Biophysical Mechanisms of the Kinetochore-Microtubule Interface

and its Regulation During Mitosis

Neil T. Umbreit

A dissertation

submitted in partial fulfillment of the

requirements for the degree of

Doctor of Philosophy

University of Washington

2014

Reading Committee:

Trisha N. Davis, Chair

Charles L. Asbury

Alexey J. Merz

Program Authorized to Offer Degree:

Biochemistry

University of Washington

Abstract

Biophysical Mechanisms of the Kinetochore-Microtubule Interface

and its Regulation During Mitosis

Neil T. Umbreit

Chair of the Supervisory Committee:

Trisha N. Davis, Professor and Chair

Department of Biochemistry

Chromosomes carry the genetic information that acts as a "blueprint" for every organism. When cells divide, replicated copies of the chromosomes are segregated into two new cells that are genetic copies of the original. This process is mediated by the mitotic spindle, a bipolar array of dynamic microtubules that connect to chromosomes and drive their segregation. Microtubules link to chromosomes via kinetochores, which assemble on the centromeres and present microtubule attachment sites. These kinetochore-microtubule linkages are tightly regulated to ensure accurate transmission of the genetic material during each division.

In the budding yeast *Saccharomyces cerevisiae*, kinetochore-microtubule attachments are mediated by the Ndc80 and Dam1 complexes. Both are essential for viability, though their distinct contributions to kinetochore-microtubule coupling were previously unknown. We showed that these complexes interact directly to form robust linkages to dynamic microtubule ends. Furthermore, the interaction between these complexes can be disrupted by the mitotic

regulatory kinase, Aurora B. During error correction, Aurora B detaches aberrant kinetochore-microtubule linkages, providing another chance to form correct attachments. We propose that Aurora B targets the interaction between the Ndc80 and Dam1 complexes during corrective detachment. In higher eukaryotes, error correction appears to depend additionally on modulating microtubule dynamics to promote microtubule disassembly. We showed that this effect is exerted through Aurora B regulation of the human Ndc80 complex.

Kinetochore-microtubule linkages require the combined activity of many different kinetochore components. Moreover, these components are present in multiple copies, as ~20 Ndc80 complexes and ~30 Dam1 complexes act collectively at each kinetochore-microtubule interface. *In vitro*, Dam1 complexes associate together to form large oligomeric rings that encircle microtubules; how this oligomerization contributes to kinetochore function has remained unclear. We found that oligomerization of the Dam1 kinetochore complex is required for its ability to form microtubule attachments that are robust against tension *in vitro* and *in vivo*. In higher eukaryotes, the Ndc80 and Ska complexes are both reported to oligomerize on microtubules. Therefore, we propose that oligomerization is an essential and conserved feature of kinetochore components that is required for accurate chromosome segregation during mitosis.

Table of Contents

List of Figures

List of Tables

Acknowledgements

I am especially grateful to my thesis advisor, Trisha Davis, for her candid mentoring and unfailing support. I am also fortunate to have received invaluable training and guidance from Chip Asbury. Thanks to their combined effort, I found a way to succeed as a biochemist and a biophysicist, and to strike a balance between independent research and collaboration. I additionally acknowledge Trisha Davis, Chip Asbury, and Alex Merz for their helpful insights and suggestions on my thesis and for their input on my scientific development, along with Rachel Klevit and Linda Wordeman, as my advisory committee. I am honored to name as peers and colleagues the members of the Davis and Asbury labs, past and present. In particular, Jerry Tien, Dan Gestaut, Andrew Franck, and Matt Miller all deserve special mention for their significant contributions as co-authors in the work presented in this thesis. I also thank those closest to me – Tim and Sylvia Umbreit, Kevin and Hilary Umbreit, Minerva Sanchez – for providing encouragement and optimism in ample abundance.

Chapter 1.

Introduction

The cell cycle: autocatalyzed formation of new life

The origin of life on Earth is a fascinating and mysterious incident that has captivated the minds of scientists for centuries. Current models propose that this event was instigated by a spontaneous organization of small organic molecules, such as by their sequestration inside lipid droplets, and/or cross-reactions that generated autocatalytic molecules or formed primitive metabolic pathways (ORGEL 1998). Such events might occur with extremely low probability even in amenable circumstances, as suggested in part by the interrelatedness of all known forms of life that suggests their singular origin. By contrast, living cells use small organic molecules to produce new life at a prodigious rate; in the most dramatic case yet observed, the bacterium *Vibrio natriegens* doubles in as few as seven minutes (MAIDA *et al.* 2013). Thus, cells dramatically increase the rate at which new cells are formed, relative to spontaneous assembly from the constituent parts. This kinetic enhancement is the result of billions of years of evolution, through which cells have developed efficient and reliable growth cycles.

Actively growing eukaryotic cells proceed through a four-stage cell cycle, which consists of two "gap" phases separated by a "synthesis" phase, and is completed by the "mitotic" phase. During the gap phases, G1 and G2, the cell grows and accrues resources. Between G1 and G2, the entire genome is duplicated during synthesis (S) phase, so that each chromosome comprises two identical copies, or "sister" chromatids. Sister chromatids remain physically linked as a pair until mitotic (M) phase, when they are segregated equally into two new "daughter" cells that are exact genetic copies of the original "mother" cell. Therefore, the cell cycle represents an

autocatalytic mechanism by which cells create new life, using their own constitution as a template.

Mitosis requires dramatic re-programming of cellular physiology

Intricate regulatory pathways have evolved to control cell cycle progression and ensure that key events occur in proper succession (PAGLIUCA *et al.* 2011). In this regard, no other stage of the cycle is more dramatic than mitosis, when cells undergo a regulated sequence of radical morphological changes. First observed well over a hundred years ago, mitotic events are so striking that their fundamental importance for heritability was correctly inferred decades ahead of the definitive demonstration that chromosomes carry the genetic information of the organism. Indeed, we now know that mitosis involves reorganization at essentially every level of cellular structure and function. For example, in most eukaryotic organisms, these changes include the compaction of chromosomes, global repression of transcriptional activity, and total rearrangement of the cytoskeleton (GOTTESFELD and FORBES 1997; LANCASTER and BAUM 2014; VAGNARELLI 2012). Amazingly, all of these examples are events that occur during prophase, which is only the first stage of mitosis.

Cytoskeletal reorganization results in the construction of the mitotic spindle, an elaborate network of microtubules organized from two spindle poles. This bipolar structure is responsible for feats of large-scale mechanical manipulation of the replicated chromosomes. During prometaphase, the chromosomes become physically linked to spindle microtubules. The chromosomes are carried to the spindle midzone and become aligned in a bipolar orientation, such that sister chromatids attach to microtubules emanating from opposite spindle poles. Metaphase represents the time at which all of the chromosomes have achieved this bipolar attachment state. Next, the highly synchronized separation of all sister chromatid pairs is

coordinated with rapid spindle elongation, as the two copies of the genome are pulled towards opposite ends of the cell in anaphase. During telophase, the two genomes are encapsulated within separate nuclear envelopes. Finally, cytoskeletal components mediate the contraction and abscission of the cell between the two nuclei during cytokinesis, completing mitosis by cleaving the cell itself in half.

Dynamic spindle microtubules provide the energy for chromosome movements

The movement of chromosomes during mitosis is driven by spindle microtubules, which are polymers of α-/β-tubulin heterodimers. In the polymer lattice, tubulin dimers associate longitudinally to form protofilaments. Lateral contacts between tubulin dimers join the protofilaments (typically 13 per microtubule) together to form a closed tube (EVANS *et al.* 1985; LEDBETTER and PORTER 1963).

In vitro and *in vivo*, microtubules undergo dynamic assembly and disassembly, as tubulin subunits add onto and dissociate from the ends of the filaments (JOHNSON and BORISY 1977; SOLTYS and BORISY 1985). Each tubulin subunit carries a guanosine nucleotide. *In vitro*, microtubule assembly requires the addition of GTP-bound tubulin dimers at the end of the filament, as GDP-bound tubulin is unstable at microtubule ends (RICE *et al.* 2008). After incorporation into the polymer lattice, tubulin subunits hydrolyze their bound GTP, and the energy of GTP hydrolysis is stored in the microtubule lattice (MITCHISON and KIRSCHNER 1984). Stochastic fluctuations in assembly or a decrease in the availability of GTP·tubulin can cause GDP·tubulin subunits to become exposed at the end of the filament. When this occurs, the microtubule end becomes destabilized and the tube begins to disintegrate, releasing the stored energy of GTP hydrolysis. The transition from microtubule growth to shortening is called a catastrophe. Microtubule disassembly continues until the polymer is eliminated, or until a

spontaneous reversion to microtubule assembly occurs, which is called a rescue. Through cycles of polymer assembly and disassembly, microtubules can undergo dynamic changes in length over time – this behavior is referred to as dynamic instability. By physically coupling chromosomes to dynamic microtubule ends, these changes in filament length can be harnessed to do the mechanical work of moving chromosomes during mitosis.

Kinetochores mediate the crucial linkage between chromosomes and dynamic microtubule ends

Kinetochores assemble on specialized chromosomal regions called centromeres (BIGGINS 2013). Each kinetochore anchors directly into the chromatin itself via a specialized histone H3 variant that assembles into nucleosomes at the centromere, as well as through other kinetochore components that bind to centromeric DNA. Together, these "inner" kinetochore components scaffold the centromere-targeted assembly of a host of additional kinetochore proteins that form a "central" structural core. The core proteins form a platform upon which is built an array of "outer" kinetochore components that bind to the ends of microtubules. Therefore, kinetochores represent the keystones of the mitotic machinery, providing the essential physical linkages between replicated chromosomes and the bipolar mitotic spindle.

Through their direct attachment to microtubule ends, kinetochores transduce chemical energy from microtubule dynamics into mechanical energy to drive chromosome movements (ASBURY *et al.* 2011). In addition, the resulting mechanical forces are used as an important indicator of kinetochore-microtubule attachment state (LAMPSON and CHEESEMAN 2011). High levels of tension are exerted across a kinetochore pair assembled on sister chromatids when they are attached in a bipolar orientation, such that the two kinetochores can be pulled toward opposite spindle poles. In contrast, relatively little tension is applied across the kinetochores

when a sister pair is instead attached to only one spindle pole. Kinetochore tension can thus be used as a means to detect the correct bipolar alignment of sister chromatids.

By necessity, kinetochores satisfy an apparent paradox: they form microtubule attachments that are robust against tension, yet retain the ability to track with a substrate in continuous flux. The mechanisms and molecular requirements underlying these feats are the subject of Chapters 2 and 3.

Kinetochore-microtubule attachments are regulated by error correction machinery

One of the most important mitotic signals appears to be kinetochore-microtubule attachment state. As discussed above, the tension applied across kinetochores is thought to be a key mechanical signal by which correct and incorrect attachments are distinguished. Regulatory pathways detect erroneous attachments and promote their detachment (PINSKY *et al.* 2006). This turnover process is highly selective, as only those kinetochores that are incorrectly attached are targeted for release in order to make another attempt at forming correct attachments. While unattached from the mitotic spindle, kinetochores additionally propagate a signal that inhibits chromosome segregation (FOLEY and KAPOOR 2013). This "wait-anaphase" signal ensures that each chromosome has sufficient time to become aligned properly on the mitotic spindle prior to the separation of sister chromatids. Thus, kinetochores act as regulatory hubs that integrate signals to promote the bipolar alignment and synchronized segregation of chromosomes. The biophysical mechanisms by which the mitotic error correction machinery targets kinetochore-microtubule attachments for release is addressed in Chapters 2 and 4.

Chapter 2.

Cooperation of the Dam1 and Ndc80 kinetochore complexes enhances microtubule coupling and is regulated by Aurora B

Introduction

During mitosis, kinetochores attach to assembling and disassembling microtubule tips while withstanding tensile forces from the mitotic spindle (MADDOX *et al.* 2003; SKIBBENS *et al.* 1995; SKIBBENS *et al.* 1993). Kinetochores are able to harness energy from these disassembling microtubule tips to drive movement of chromosomes (for a review, see INOUE and SALMON 1995). Understanding how the kinetochore establishes microtubule attachments under force requires understanding the organization of the kinetochore components and how they bear and transmit load. Recent studies investigated the spatial organization of kinetochore components in vivo and how their arrangement changes throughout mitosis (JOGLEKAR *et al.* 2009; WAN *et al.* 2009). Through systematic reconstitution of kinetochore components, we are pursuing a complementary approach with the ultimate goal of mapping the transmission of force across the kinetochore from the dynamic microtubule to the centromere. Here, we focus on the kinetochore-microtubule interface.

The kinetochores of all eukaryotes contain multiple microtubule-binding elements. The KMN network (KNL-1, Mis12 complex and Ndc80 complex) and the Ska1 complex both bind microtubules in higher eukaryotic cells (CHEESEMAN *et al.* 2006; GAITANOS *et al.* 2009; WELBURN *et al.* 2009). Yeast also contain the KMN network and the Dam1 complex, possibly the functional homolog of the Ska1 complex (GAITANOS *et al.* 2009; HANISCH *et al.* 2006;

RAAIJMAKERS *et al.* 2009; WELBURN *et al.* 2009). Cooperation of the three components of the conserved KMN network was shown by cosedimentation with taxol-stabilized microtubules (CHEESEMAN *et al.* 2006), but how or whether any of the microtubule-binding components cooperate to achieve attachment to dynamic microtubules is unknown. We show for the first time that cooperation between two kinetochore subcomplexes enhances processive, load-bearing coupling to dynamic microtubule tips.

In the budding yeast kinetochore, all four proteins of the Ndc80 complex and all ten proteins of the Dam1 complex are essential (TANAKA and DESAI 2008). In vitro, both complexes independently form diffusive attachments to the microtubule lattice and track with disassembling microtubule tips, although the Ndc80 complex requires artificial oligomerization to tip-track (GESTAUT *et al.* 2008; POWERS *et al.* 2009; WESTERMANN *et al.* 2006). When attached to beads, each complex also forms load-bearing attachments to dynamic microtubule tips (ASBURY *et al.* 2006; FRANCK *et al.* 2007; GRISHCHUK *et al.* 2008a; GRISHCHUK *et al.* 2008b; POWERS *et al.* 2009). Despite these similarities, the Ndc80 and Dam1 complexes are not redundant. The Ndc80 complex is required in vivo for attachment to microtubules (KLINE-SMITH *et al.* 2005), and the Dam1 complex is required for attaching to the tips of microtubules and for establishing biorientation (SHIMOGAWA *et al.* 2006; TANAKA *et al.* 2005). Moreover, the Ndc80 complex is required for the assembly of Dam1 complex onto the kinetochore (JANKE *et al.* 2002), and an interaction between the two complexes has been suggested by localization and two-hybrid studies (JOGLEKAR *et al.* 2009; SHANG *et al.* 2003). Studying the combination of Ndc80 and Dam1 complexes in vitro will allow us to dissect their distinct roles in kinetochore-microtubule binding.

Kinetochores not only serve as physical bridges between chromosomes and spindle microtubules but also are regulatory hubs that ensure chromosome segregation fidelity during mitosis. For example, Aurora B kinase is responsible for resetting aberrant kinetochore-microtubule attachments to achieve biorientation (CHEESEMAN *et al.* 2002; HAUF *et al.* 2003; PINSKY *et al.* 2006; TANAKA *et al.* 2002). Many of the microtubule-binding components of the kinetochore, including the Ndc80 and Dam1 complexes, are targets of Aurora B (CHEESEMAN *et al.* 2002; CHEESEMAN *et al.* 2006; DELUCA *et al.* 2006; GESTAUT *et al.* 2008; PINSKY *et al.* 2006; SHANG *et al.* 2003). In mammalian cells, Aurora B phosphorylation of the N-terminal tail of the Ndc80 protein (Hec1 in humans) abolishes kinetochore-microtubule attachment (DELUCA *et al.* 2006; GUIMARAES *et al.* 2008). While the budding yeast Ndc80 protein also has an N-terminal tail, it is not essential (AKIYOSHI *et al.* 2009). Previously, we demonstrated that phosphorylation by the yeast Aurora B homolog Ipl1 at one target site within the Dam1 complex, Ser 20 of Dam1, reduces its affinity for the microtubule lattice (GESTAUT *et al.* 2008). Two-hybrid assays and pull downs with in vitro translated proteins using phosphomimetic mutations at Ipl1 target sites in Dam1 also suggested that phosphorylation of the Dam1 complex modulates its interaction with the Ndc80 complex (SHANG *et al.* 2003). Moreover, Ipl1 target sites on Dam1 are dephosphorylated as cells enter metaphase in a cohesin-dependent manner, which could prevent kinetochore-microtubule attachment turnover as biorientation is established (KEATING *et al.* 2009).

Here we show that the Dam1 complex is a phosphoregulated processivity factor for the Ndc80 complex in kinetochore-microtubule coupling. Using techniques for tracking and manipulating single molecules in vitro, we demonstrate directly an interaction between the Ndc80 and Dam1 complexes on microtubules. Through this interaction, the Dam1 complex

enhances the ability of the Ndc80 complex to maintain attachment to dynamic microtubule tips even in the presence of external load. Finally, this interaction is regulated by Ipl1, further defining the mechanism for Aurora B-mediated corrective detachment in vivo.

Results

The Dam1 and Ndc80 complexes interact on microtubules

We expressed recombinant *S. cerevisiae* Ndc80 and Dam1 complexes in *E. coli*, and purified each complex by affinity chromatography and gel filtration (GESTAUT *et al.* 2008; POWERS *et al.* 2009; WEI *et al.* 2005). By velocity sedimentation analysis, we found weak interaction between the Ndc80 and Dam1 complexes free in solution (Figure 2.1). Using total internal reflection fluorescence (TIRF) microscopy, we then quantified the interaction of GFP-tagged Ndc80 complexes with microtubules in the presence and absence of Dam1 complex (Figure 2.2). In the absence of Dam1 complex, individual Ndc80 complexes formed transient and diffusive attachments to microtubules, as reported previously (POWERS *et al.* 2009). We measured a dissociation rate constant (k_{off}) of 0.44 ± 0.03 s^{-1}, an association rate constant (k_{on}) of 0.60 ± 0.02 $\mu M^{-1} \cdot s^{-1}$, and a diffusion constant of 0.067 ± 0.003 $\mu m^2 \cdot s^{-1}$ (Figure 2.2C–E), values comparable to our previous study. We also simultaneously visualized GFP-tagged Ndc80 complexes and mCherry-tagged Dam1 complexes on microtubules. At concentrations affording single molecule resolution of each complex, interaction events were rare. When the two complexes did associate with each other, they appeared to diffuse more slowly (Figure 2.3). However, interaction events between individual Ndc80 and Dam1 complexes were too infrequent to affect population behavior. To increase the frequency of interactions, we raised the concentration of Dam1 complex while maintaining low concentrations (10 pM) of the Ndc80 complex. Overall, Ndc80 complex transitioned gradually to a more persistent and more slowly

diffusing behavior as the concentration of Dam1 complex was increased (Figure 2.2C–E). At 500 pM Dam1 complex, the Ndc80 complex dissociated two-fold more slowly from the microtubule ($k_{off} = 0.23 \pm 0.02\ s^{-1}$) and associated 1.6-fold faster onto the microtubule ($k_{on} = 0.99 \pm 0.02\ \mu M^{-1} \cdot s^{-1}$) as compared to Ndc80 complex alone. This corresponds to a three-fold decrease in the apparent equilibrium dissociation constant, $K_d = k_{off} \cdot k_{on}^{-1}$ ($0.74 \pm 0.06\ \mu M$ to $0.23 \pm 0.02\ \mu M$). At 500 pM Dam1 complex, the Ndc80 complex also diffused five-fold more slowly ($0.013 \pm 0.0006\ \mu m^2 \cdot s^{-1}$) as compared to Ndc80 complex alone. The Dam1 complex was unlikely to be acting as a simple barrier to diffusional motility, as the diffusive behavior of the Ndc80 complex was unchanged in the presence of phosphorylated Dam1 complex at the same lattice density (see below). The brightness distribution of the GFP signal remained unchanged across concentrations of the Dam1 complex, demonstrating that oligomerization of the Ndc80 complex did not contribute to its modified behavior in the presence of the Dam1 complex (Figure 2.4). Even at 500 pM Dam1 complex, not all Ndc80 complexes bound persistently and diffused slowly. This indicates that not all Ndc80 complexes were associated with Dam1 complexes, so our calculated values describe a mixed population and likely underestimate Dam1 complex-mediated enhancement of Ndc80 complex-microtubule interactions.

In the presence of the Dam1 complex, diffusion of the Ndc80 complex is slowed far below the reported rate for a single Dam1 complex (GESTAUT *et al.* 2008). Therefore, we hypothesized that at the concentrations required to observe significant changes in the population behavior of the Ndc80 complex, the Dam1 complex forms slowly diffusing oligomers. To test this, we measured the diffusion rate of GFP-tagged Dam1 complex on microtubules (Figure 2.5A-B). At 2 pM, single GFP-tagged Dam1 complexes diffused rapidly, at $0.060 \pm 0.003\ \mu m^2 \cdot s^{-1}$, similar to the rates reported previously (GESTAUT *et al.* 2008;

WESTERMANN *et al.* 2006). At 20 and 50 pM Dam1 complex, however, we observed slowly diffusing spots that exhibited fluorescence brighter than individual Dam1 complexes. To maintain single molecule resolution for quantifying the diffusion of Dam1 complex at higher concentrations, we mixed untagged Dam1 complex with a small amount of GFP-tagged Dam1 complex. At 500 pM, Dam1 complex diffused at least 60-fold more slowly than at 2 pM (Figure 2.5B). These observations indicate that oligomerization of the Dam1 complex slows its diffusion rate, as reported previously (GRISHCHUK *et al.* 2008a). Moreover, they imply that the enhanced binding of Ndc80 complex to microtubules that we have quantified here (e.g., in Figure 2.2C–E) occurs via interaction with Dam1 complexes that are primarily in an oligomeric state.

In vitro, the Dam1 complex forms rings of 16-25 complexes that encircle microtubules (MIRANDA *et al.* 2007; WANG *et al.* 2007). To investigate whether rings are important for interaction with the Ndc80 complex, we used negative-stain electron microscopy to quantify ring formation on taxol-stabilized microtubules (at 36 nM tubulin) across a range of Dam1 concentrations (Appendix A, Figure 3). At 500 pM Dam1 complex, the highest concentration used in our TIRF assays, rings were absent. Instead, we observed small particles scattered around or attached to the filaments. The dimensions of these particles were consistent with Dam1 complex dimers (WANG *et al.* 2007). Rings first appear on microtubules at 1 nM Dam1 complex, substantially increase in density between 5 and 10 nM, and saturate at 100 nM (Appendix A, Table 1). These findings are consistent with a strong and cooperative binding of the Dam1 complex to microtubules as reported previously (GESTAUT *et al.* 2008).

While 500 pM Dam1 complex did not assemble into rings on microtubules at 36 nM tubulin, reducing the amount of tubulin could promote ring formation by increasing the density of Dam1 complex bound to microtubules. To explore the magnitude of this effect, we imaged

500 pM Dam1 complex on microtubules at 5-fold lower tubulin (7 nM). Rings were again absent (n = 8 microtubules, 101 μm total). Further reductions in tubulin concentration were impractical because the microtubules became too sparse on the electron microscopy grids. Since the effective concentration of tubulin polymer in our TIRF assays was lower still (~1 nM), it remains possible that Dam1 complex rings contributed to the observed alterations in behavior of the Ndc80 complex. We note, however, that two observations suggest ring formation is not required for the initial interaction between the Ndc80 and Dam1 complexes. First, the Dam1 and Ndc80 complexes interact during velocity sedimentation, where the Dam1 complex is primarily in dimeric form (see Figure 2.1). Second, interactions between individual Ndc80 and Dam1 complexes can be observed directly in TIRF assays (albeit rarely; see Figure 2.3).

The Dam1 complex enhances attachment of the Ndc80 complex to dynamic microtubule tips

The Ndc80 complex has been shown to track efficiently with disassembling microtubule tips in vitro, but only when it is bound to beads or to antibodies (POWERS *et al.* 2009). In contrast, the Dam1 complex tracks robustly with disassembling tips without artificial oligomerization (GESTAUT *et al.* 2008; WESTERMANN *et al.* 2006). We therefore tested whether the Dam1 complex enhances tip-tracking by the Ndc80 complex. We grew microtubules from non-hydrolyzable GMPCPP seeds in the presence of free fluorescent-labeled tubulin and GTP. We visualized the behavior of GFP-tagged Ndc80 complex as microtubules disassembled after the free tubulin was removed. By itself, the Ndc80 complex localized only briefly to microtubule tips during disassembly (Figure 2.6A). Most binding events were transient and diffusive similar to those seen on taxol-stabilized microtubules (and as reported in POWERS *et al.* 2009). In contrast, the addition of Dam1 complex, which accumulates at the disassembling

microtubule tip (Figure 2.5C), substantially increased the tip-tracking behavior of the Ndc80 complex (Figure 2.6A). Ndc80 complexes bound preferentially at the microtubule tip, were more persistently attached, and moved with the disassembling tip.

For quantification, we defined tip-tracking as the colocalization of GFP-tagged Ndc80 complex with disassembling microtubule tips. In the presence of Dam1 complex, Ndc80 complex tracked with 78% (62 of 80) of disassembling microtubule tips over an average distance of 1.2 ± 0.2 μm, compared to only 27% (19 of 71) of tips over an average distance of 0.13 ± 0.09 μm in the absence of Dam1 complex (Figure 2.6B). In the presence of the Dam1 complex, tip-tracking events by the Ndc80 complex often continued until the tips reached the microtubule seeds. Therefore, we likely underestimate the effect of the Dam1 complex to enhance the ability of the Ndc80 complex to track disassembling tips.

We then used an optical trapping-based force clamp (ASBURY *et al.* 2006; FRANCK *et al.* 2010; FRANCK *et al.* 2007; POWERS *et al.* 2009) to test if the Dam1 complex enhances the tip-tracking ability of Ndc80 complex while under load. We attached beads decorated with Ndc80 complex to the tips of assembling microtubules in the presence and absence of free Dam1 complex. We applied constant tensile force until the attachment broke, the microtubule switched to disassembly or, in a few cases, the event was terminated by other causes (e.g., the bead became stuck to the coverslip). In the absence of Dam1 complex, bead-bound Ndc80 complex formed persistent load-bearing attachments to assembling and disassembling microtubule tips (Appendix A, Figure 5), as reported previously (POWERS *et al.* 2009). While bearing 1.8 ± 0.4 pN (mean ± s.d.) of continuous load, travel distances during assembly were broadly distributed with a mean of 350 nm (n = 115). Detachment from assembling tips occurred at a rate of 0.026 ± 0.003 s^{-1} (Appendix A, Figure 5B). To mimic the likely arrangement in vivo, we

added free Dam1 complex lacking an affinity tag so that it interacted with the beads only via its interaction with Ndc80 complex (i.e., direct Dam1 complex-bead interactions were prevented – see Appendix A, Methods). In the presence of the Dam1 complex, the mean travel distance increased three-fold to 1,100 nm ($n = 42$, $P = 3 \cdot 10^{-8}$, KS test) and the detachment rate decreased five-fold to 0.005 ± 0.0008 s^{-1} (Appendix A, Figure 5B). Accordingly, plots of survival probability versus distance show that the couplers remained more persistently attached when Dam1 complex was present (Appendix A, Figure 5C).

We also developed a force ramp assay to test the coupling performance of bead-bound Ndc80 complex across a broader range of forces on both assembling and disassembling microtubule tips (FRANCK *et al.* 2010). After an initial 'preload' period at approximately 1 pN constant force, we gradually increased the force on a tip-attached bead at a constant rate (0.25 pN$\cdot s^{-1}$) until the bead detached from the microtubule tip, the load limit of the trap (10-12 pN) was reached, or in the case of disassembling filaments, the microtubule switched from shortening to growth (Appendix A, Figure 6). The maximum force achieved prior to any one of these termination points was recorded for each event. Without Dam1 complex present, all events recorded during microtubule assembly ended in detachment. Most events during disassembly also ended in detachment (93 of 96), but a few ended with a shortening-to-growth transition (2 of 96) or when the trap load limit was reached (1 of 96). The resulting maximum forces were distributed narrowly, with means of 2.7 ± 0.1 pN ($n = 101$) during assembly and 2.7 ± 0.1 pN ($n = 96$) during disassembly (Appendix A, Figure 6E-F). The addition of Dam1 complex resulted in a clear improvement in the load-bearing capacity of the Ndc80 complex-coated beads. Most events recorded during assembly ended in detachment (112 of 131) but some persisted until the trap load limit was reached (19 of 131). Of the events recorded during disassembly, only

about half ended in detachment (43 of 92). The remainder terminated when the microtubule switched to assembly (43 of 92) or, in a few cases, when the load limit was reached (6 of 92). The high frequency of shortening-to-growth transitions indicates that tension applied through linkages composed of both Ndc80 and Dam1 complexes promotes microtubule rescue, a phenomenon we saw previously using bead-bound Dam1 complex alone (FRANCK *et al.* 2007). The resulting maximum forces were distributed broadly with means of 5.2 ± 0.2 pN during assembly (n = 131) and 4.4 ± 0.2 pN during disassembly (n = 92), values that are two-fold higher than in the absence of Dam1 complex ($P < 1 \cdot 10^{-8}$ assembly; $P = 1 \cdot 10^{-8}$ disassembly). These observations, together with the force clamp results, show that interactions between Dam1 and Ndc80 complexes enhance coupling to both assembling and disassembling microtubule tips under load. This enhancement persists across a range of loads (up to 10 pN) and it occurs under conditions where the entire load is ultimately transmitted to the cargo through the Ndc80 complex.

Ipl1 phosphorylation regulates the interaction between Ndc80 and Dam1 complexes

We then asked if Ipl1 phosphorylation of the Dam1 complex regulates its interaction with the Ndc80 complex on microtubules. Phosphorylation of Ser 20 on the Dam1 protein weakens the interaction of the Dam1 complex with microtubules (GESTAUT *et al.* 2008). To determine how phosphorylation at sites other than Ser 20 affects the interaction between the Dam1 and Ndc80 complexes, we used a modified Dam1 complex with a Ser 20 to Ala mutation (S20A). With the S20A substitution, the Dam1 complex interacts with microtubules in a manner that is indistinguishable from the wild-type complex, except that the interaction is insensitive to Ipl1 phosphorylation (Figure 2.7A-B). The phosphorylated S20A Dam1 complex also tracks with disassembling microtubule tips and is less diffusive at high concentrations, as expected for

oligomers (Figure 2.5). Phosphorylated S20A Dam1 complex also slows the disassembly of microtubules, as reported for wild-type Dam1 complex (FRANCK *et al.* 2007; GRISHCHUK *et al.* 2008a; WESTERMANN *et al.* 2006).

In the presence of unphosphorylated S20A Dam1 complex, diffusion of the Ndc80 complex on microtubules is slowed, dissociation rate constant is decreased and tip-tracking is enhanced as described for the wild-type Dam1 complex (Figure 2.8). However, Ipl1 phosphorylation of the S20A Dam1 complex abolished the ability of Dam1 complex to slow the diffusion and to decrease the dissociation rate constant of the Ndc80 complex (Figure 2.8B-C). Moreover, phosphorylated S20A Dam1 complex did not enhance the tip-tracking ability of the Ndc80 complex (Figure 2.8D). Control experiments were performed to ensure that after the initial Ipl1 phosphorylation reaction with the S20A Dam1 complex, residual Ipl1 activity was negligible (Figure 2.9; see Materials and Methods below). Furthermore, the ten proteins of the Dam1 complex do not dissociate from one another when the complex is phosphorylated by Ipl1 (Figure 2.7C). Since phosphorylation of the S20A Dam1 complex does not alter the behavior of the Dam1 complex alone but abolishes its ability to change the behavior of the Ndc80 complex, we conclude that Ipl1 phosphorylation of the Dam1 complex inhibits its interaction with the Ndc80 complex.

Discussion

The Dam1 complex acts as a processivity factor for the Ndc80 complex

Many molecular machines require factors that enhance their processivity. For example, the proliferating cell nuclear antigen (PCNA) sliding clamp is required for efficient DNA replication by DNA polymerase ε (KELMAN 1997). Likewise, dynactin is required for long-distance movement of cytoplasmic dynein along microtubules (KING *et al.* 2000). Kinetochores

are processive and form persistent attachments to dynamic microtubule tips over the times and distances required for chromosome biorientation and segregation. However, the contribution of individual components to the processivity of kinetochore-microtubule attachments is poorly understood. Here we show that the Dam1 complex enables the Ndc80 complex to track with disassembling microtubule tips over distances in excess of the length of the entire yeast spindle. We also show that the Dam1 complex strengthens the attachment of the Ndc80 complex to dynamic microtubule tips. In vivo, assembly of the Dam1 complex onto the kinetochore requires the Ndc80 complex (JANKE *et al.* 2002). In our optical trap experiments, bead-bound Ndc80 complex was assayed with the Dam1 complex free in solution to mimic this arrangement in vitro. The increased ability of bead-bound Ndc80 complexes to bear load in the presence of free Dam1 complex indicates that tensile force can be transmitted through an Ndc80 complex-based linkage in a physiologically relevant arrangement.

We propose that the Dam1 complex acts as a processivity factor for the Ndc80 complex, and that the two complexes cooperate to form load-bearing kinetochore-microtubule attachments. In vivo, the Ndc80 complex forms lateral attachments to spindle microtubules prior to kinetochore association of Dam1 complex and biorientation (SHIMOGAWA *et al.* 2006; TANAKA *et al.* 2005). Our results are consistent with a model in which the Ndc80 complex initially mediates kinetochore attachment to microtubules. The Dam1 complex is later loaded onto the kinetochore to maintain attachment to dynamic microtubule tips. Association of the Dam1 complex is particularly important for these attachments to withstand the tensile forces required for biorientation. The existence of a distinct and separable processivity factor also provides a point of regulation for corrective detachment.

A mechanism for Aurora B-mediated corrective detachment

The regulatory mechanism that ensures chromosome biorientation has been proposed to respond to the level of tensile force on the kinetochore (KELLY and FUNABIKI 2009). When kinetochores make attachments that generate little tension, such as monotelic or syntelic attachments, progression to anaphase is blocked. Key to this regulation, the conserved Aurora B kinase is responsible for the release of aberrant kinetochore-microtubule attachments (BIGGINS *et al.* 1999; HAUF *et al.* 2003; PINSKY *et al.* 2006; TANAKA *et al.* 2002). We showed previously that phosphorylation by the yeast Aurora B kinase Ipl1 at Ser 20 of Dam1 decreases the affinity of the Dam1 complex for the microtubule lattice (GESTAUT *et al.* 2008). We show here that Ipl1 phosphorylation of the Dam1 complex at sites other than Ser 20 weakens its interaction with the Ndc80 complex. Together these observations suggest that Ipl1 phosphorylation of the Dam1 complex promotes corrective detachment of kinetochores via two distinct mechanisms, decreasing the affinity of the Dam1 complex for both the Ndc80 complex and for microtubules. Regulation by Aurora B kinase is a conserved feature of kinetochore function in all eukaryotes. Therefore, we propose that regulation at both the kinetochore-microtubule interface and between components of the kinetochore itself will extend to mechanisms of corrective detachment in higher eukaryotes.

Materials and Methods

Protein Expression and Purification

The *S. cerevisiae* Ndc80 and Dam1 complexes were expressed from polycistronic vectors in *E. coli* as described (GESTAUT *et al.* 2010; GESTAUT *et al.* 2008; POWERS *et al.* 2009; WEI *et al.* 2005). For TIRF microscopy, the Ndc80 complex Nuf2 subunit was tagged with GFP, and the Dam1 complex Dad1 subunit was tagged with GFP or mCherry. Complexes were purified

by affinity chromatography and gel filtration as previously described (ASBURY *et al.* 2006; FRANCK *et al.* 2007; GESTAUT *et al.* 2008; POWERS *et al.* 2009).

For optical trap bead assays, a TEV cleavage site was inserted adjacent to the His_6 affinity tag within the GFP-tagged Dam1 complex. The complex was purified by affinity chromatography and gel filtration as previously described (GESTAUT *et al.* 2008). The cleavage reaction was carried out in 50 mM phosphate buffer, 350 mM NaCl, pH 6.9 with 1 mM DTT, 0.5 mM EDTA and recombinant TEV protease for 2 hrs at 4°C. TEV-cleaved Dam1 complex was isolated by gel filtration and cleavage was verified by immunoblot analysis.

Phosphorylation of the Dam1 complex

Dam1 complex was phosphorylated with purified GST-Ipl1 and GST-Sli15 as described (GESTAUT *et al.* 2008). The reaction (50 μl) contained 4 μM GFP- or mCherry-tagged S20A Dam1 complex, 0.5 μM GST-Ipl1, 0.5 μM GST-Sli15 (residues 554-698), 200 mM NaCl, 10 mM ATP, 25 mM $MgCl_2$ and 50 mM HEPES buffer, pH 7.2. Reactions were incubated at 30°C for 90 min. Control reactions lacked GST-Ipl1 and GST-Sli15. Control reactions lacking ATP were also performed and gave similar results as previously reported (GESTAUT *et al.* 2008). Ipl1 activity was not eliminated after the phosphorylation reaction. Therefore, to ensure that residual Ipl1 from the reaction did not affect our assays, we performed mock phosphorylation reactions using BSA in place of the Dam1 complex. The components of this mock reaction had no effect on the diffusion and dissociation rate constants of the Ndc80 complex either in the absence or presence of the Dam1 complex (Fig. S5).

TIRF Microscopy

A custom TIRF illumination system was constructed for simultaneous excitation of Alexa-647 and GFP (GESTAUT *et al.* 2010; GESTAUT *et al.* 2008; POWERS *et al.* 2009). Total

internal reflection of a far-red laser (FTEC-635-0-25-PFQ, Blue Sky Research) and a blue laser (Sapphire 488-75, Coherent) was achieved using a through-the-objective lens arrangement (100 x 1.4 numerical aperture (NA) CFI Plan Apochromat, Nikon). Images from the far-red and green channels were projected side by side onto a cooled emCCD camera (iXon 887-BI, Andor Technology).

A custom flow cell construction method (GESTAUT *et al.* 2010; GESTAUT *et al.* 2008; POWERS *et al.* 2009)was employed. Glass slides (Gold Seal) were drilled with two holes along the short axis. Double-sided sticky tape (Scotch) was placed on either side of the holes to produce the walls of the flow channel. Silanized coverslips (Corning) were then pressed firmly onto the tape and the ends of the channel were sealed with vacuum grease. To draw fluid through the channel, a peristaltic pump was used via a custom adaptor attached above one of the holes on the glass slide with adhesive transfer tape (3M).

Flow cells were washed with three 100 µl volumes of dH_2O. To bind taxol-stabilized microtubules, we flowed in a modified "rigor" kinesin (G234A) lacking motor activity (RICE *et al.* 1999) diluted in BRB80 containing 8 $mg \cdot ml^{-1}$ BSA (BB80). Flow cells were then washed with two 50-µl volumes of BB80, the second of which contained 10 µM taxol (BB80T). Alexa-647 labeled microtubules were diluted in BB80T and incubated in flow cells for 5 min. Flow cells were then washed with two 50-µl volumes of BB80T. Proteins were then introduced, diluted in BB80T containing 0.02 to 0.1 $mg \cdot ml^{-1}$ κ-casein, 200 $\mu g \cdot ml^{-1}$ glucose oxidase, 35 $\mu g \cdot ml^{-1}$ catalase, 25 mM glucose and 5 mM DTT. When assayed in combination, Ndc80 and Dam1 complexes were pre-mixed prior to their introduction into flow cells. After flowing in the protein mixture, 2000-frame movies were taken at 10 frames per second with iXon software (Andor Technology). All assays were performed at 26°C.

For disassembling microtubule assays, "rigor" kinesin was bound to flow cells and washed with 50 µl BB80, followed by 50 µl BB80 containing 0.1 mg ml^{-1} κ-casein and 1 mM GTP (GB). Alexa-647 labeled GMPCPP microtubule seeds were then bound and washed with two 50-µl volumes of GB. Microtubules were grown by incubating for ~15 min in GB containing 2 mg·ml^{-1} tubulin (Alexa-647 labeled 1:100), 200 µg·ml^{-1} glucose oxidase, 35 µg ml^{-1} catalase, 25 mM glucose and 5 mM DTT. Microtubule depolymerization was induced by buffer exchange removing free tubulin and simultaneously introducing proteins diluted in BB80 containing 0.1 mg·ml^{-1} κ-casein, 200 µg·ml^{-1} glucose oxidase, 35 µg·ml^{-1} catalase, 25 mM glucose and 5 mM DTT. Movies were started concomitantly with induction of depolymerization and taken at 10 frames per second for 2000 frames.

TIRF Microscopy Data Analysis

Software analysis of TIRF microscopy data was performed using Labview (National Instruments) as previously described (GESTAUT *et al.* 2010; GESTAUT *et al.* 2008; POWERS *et al.* 2009). The software generated the position and brightness of individual GFP-tagged complexes on microtubules over time. Custom Igor Pro (WaveMetrics) programs (available on request) were used to generate histograms of Ndc80 complex residence times on microtubules. A weighted single exponential fit was applied to determine the mean residence time, τ, and to calculate the dissociation rate constant, $k_{off} = \tau^{-1}$. Association rate constants, k_{on}, were estimated as the number of observed Ndc80 complex binding events per tubulin dimer per second, divided by the free concentration of Ndc80 complex. Standard diffusion plots of mean squared displacement versus time were generated in Igor Pro. A weighted linear fit was used to calculate the one-dimensional diffusion constant, D, of GFP-tagged complexes on microtubules.

To quantify Ndc80 complex tip-tracking, brightness profiles along disassembling tips were created in Labview. Fluorescent signals at the tips were averaged across seven frames (0.7 sec) and we required a minimum intensity threshold of 20% above background to score a tip-tracking event. For each individual frame, the instantaneous depolymerization rate was calculated as the change in tip position over 50 frames (5 sec). A microtubule disassembly event was defined to start at the first appearance of GFP-tagged Ndc80 complex at the tip, and to end when the rate of depolymerization dropped below 0.03 $\mu m \cdot s^{-1}$. Microtubule tips without tracking as defined by this criterion were omitted from further analysis. The total tracking distance for each individual tip was determined and the average tracking distance per depolymerization event was calculated.

To quantify binding to microtubules, we created brightness profiles of 500 pM mCherry-tagged Dam1 complex using our TIRF assay. After 5 min incubation with taxol-stabilized microtubules, an image was recorded (6 or 7 images per condition). For each microtubule in the image, the integrated intensity of mCherry was measured in ImageJ (NIH) and the brightness per unit length was calculated. Brightness per unit length values were averaged across all microtubules within one image, and reported as averages from multiple images.

Electron Microscopy

Electron microscopy was performed by my collaborators, Jerry Tien and Tamir Gonen. See Appendix A for details.

Optical Trap Bead Assays, Data Collection and Analysis

Our optical trap has been described previously (FRANCK *et al.* 2010; FRANCK *et al.* 2007; POWERS *et al.* 2009). These assays were performed by my collaborator, Andrew Franck. See Appendix A for details.

Figures

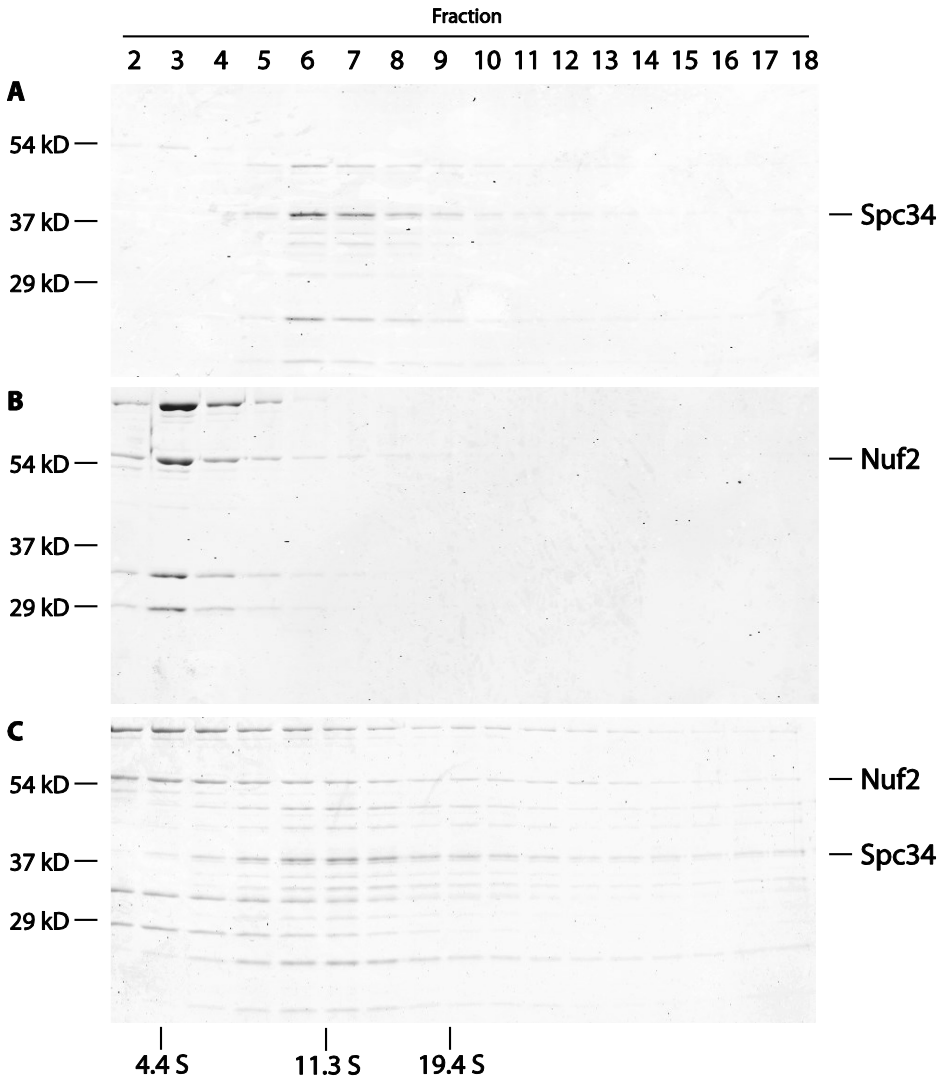

Figure 2.1: Ndc80 and Dam1 complexes interact weakly free in solution.
The interaction between Ndc80 and Dam1 complexes free in solution was assayed by velocity sedimentation. Samples (240 µl) were layered onto 4.75 ml linear sucrose gradients (8 – 32%). Gradients were centrifuged at 189,000xG at 4°C for 6 hrs and fractions (265 µl) were collected. Fraction 1 is the top of the gradient. BSA (4.4S), catalase (11.3S), and thyroglobulin (19.4S) were used as standards. When assayed alone and together, Ndc80 complex and Dam1 complex had a sedimentation coefficient of 4.4S and 11.3S respectively. Based on a Stokes radius of 9.9 nm as determined by gel filtration, the molecular weight of Dam1 complex was calculated to be ~470 kD (Siegel and Monty, 1966). Therefore, at the concentration in this assay, the 204-kD Dam1 complex exists primarily as a dimer free in solution. The positions of the Dam1 complex component Spc34 and the Ndc80 complex component Nuf2 are indicated on the right. (A) 2 µM Dam1 complex, (B) 1 µM Ndc80 complex and (C) 2 µM Dam1 complex and 1 µM Ndc80 complex in combination.

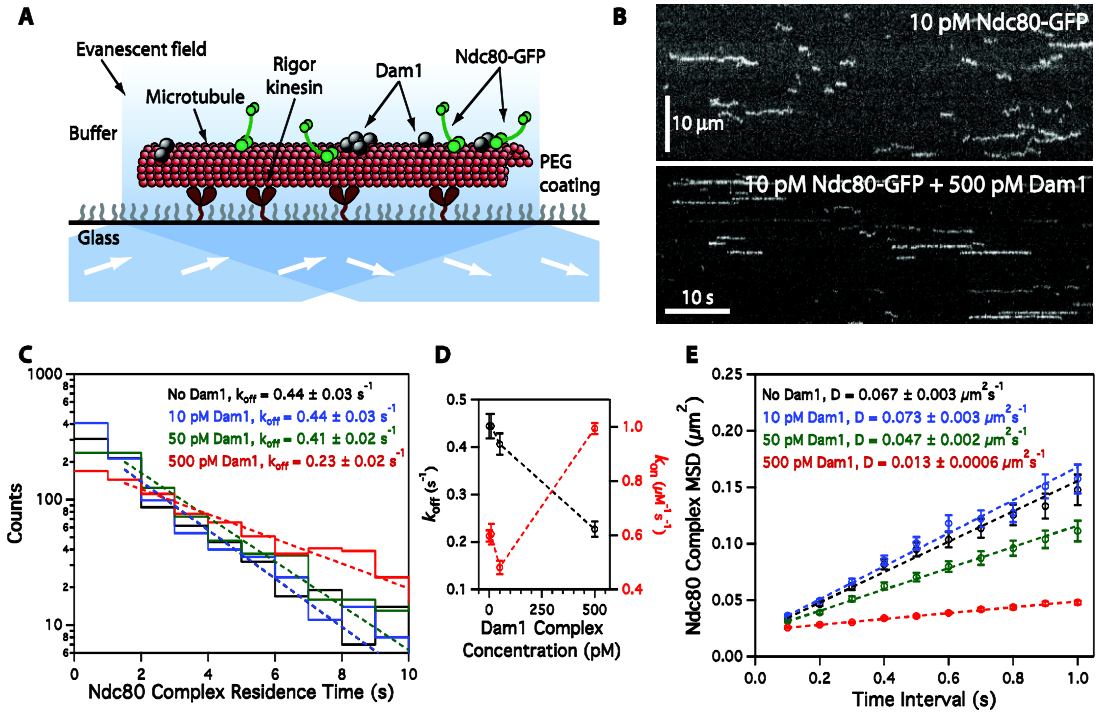

Figure 2.2: Dam1 complex enhances binding of individual Ndc80 complexes to microtubules.

(A) Schematic of the TIRF assay developed to visualize the behavior of GFP-tagged Ndc80 complexes (green rods) in the presence of untagged Dam1 complexes (grey spheres) on microtubules. (B) Representative kymographs showing the binding and one-dimensional diffusion of 10 pM Ndc80 complexes on taxol-stabilized microtubules in the absence or presence of 500 pM Dam1 complex. Positions along the microtubule are shown on the vertical axis, while the passage of time is depicted along the horizontal axis. Concentrations are of free complexes in solution. (C) Residence time distributions of 10 pM Ndc80 complex on microtubules without Dam1 complex (black histogram, n = 883 events), with 10 pM Dam1 complex (blue histogram, n = 966), with 50 pM Dam1 complex (green histogram, n = 928), and with 500 pM Dam1 complex (red histogram, n = 1003). Dotted lines show the weighted exponential fits used to determine dissociation rate constants, k_{off}. (D) Dissociation rate constants (k_{off}, left axis, black markers) for the Ndc80 complex, calculated from the data in (C), are plotted against the concentration of Dam1 complex. Association rate constants (k_{on}, right axis, red markers) of the Ndc80 complex are also plotted (without Dam1 complex, n = 1,103; with 10 pM Dam1 complex, n = 1426; with 50 pM Dam1 complex, n = 1179; with 500 pM Dam1 complex, n = 1412). (E) Mean-squared displacement (MSD) is plotted against time for 10 pM Ndc80 complex on microtubules without Dam1 complex (black markers, n = 803 events), with 10 pM Dam1 complex (blue markers, n = 859), with 50 pM Dam1 complex (green markers, n = 883), and with 500 pM Dam1 complex (red markers, n = 968). Dotted lines show the weighted linear fit used to determine diffusion constant, D. Markers are mean values ± s.e.m.

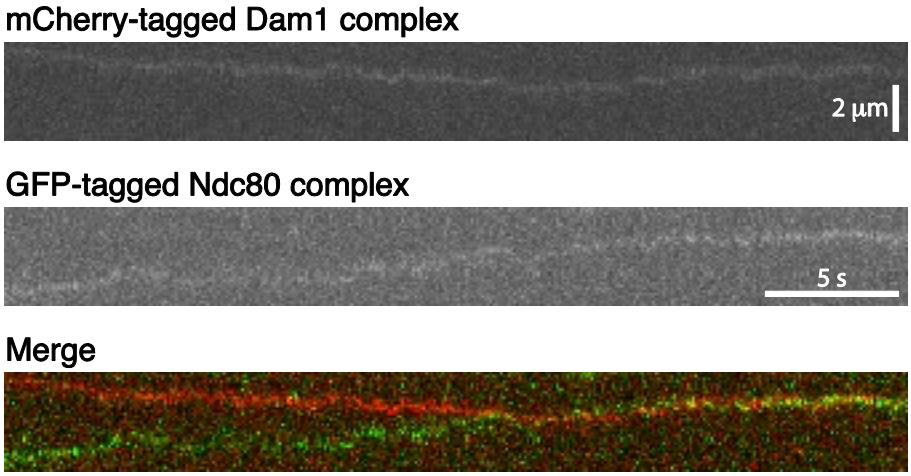

Figure 2.3: Ndc80 complex and Dam1 complex interact on microtubules.
Representative kymograph showing the diffusion of GFP-tagged Ndc80 complex (10 pM) and mCherry-tagged Dam1 complex (2 pM) on microtubules. Both complexes are diffusive alone, but appear to diffuse more slowly when they interact on microtubules.

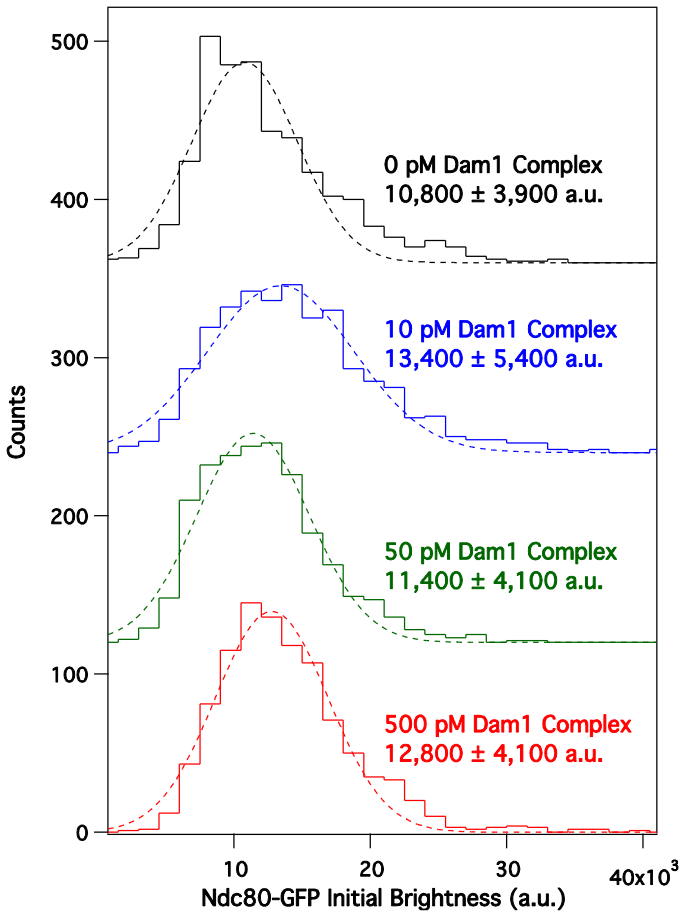

Figure 2.4: Dam1 complex does not affect the oligomerization state of the Ndc80 complex on microtubules.
Average initial brightness distributions of GFP-tagged Ndc80 complex (10 pM) binding events on microtubules without Dam1 complex (black histogram, n = 883 events), with 10 pM Dam1 complex (blue histogram, n = 966), with 50 pM Dam1 complex (green histogram, n = 928), and with 500 pM Dam1 complex (red histogram, n = 1003). Dotted lines show Gaussian fits used to determine mean values ± s.d. These values are similar to the average brightness from rare single bleach steps of GFP-tagged Ndc80 complex (9300 ± 3200 a.u., n = 11). For clarity, green, blue, and black histograms are offset vertically by 120, 240, and 360 counts respectively.

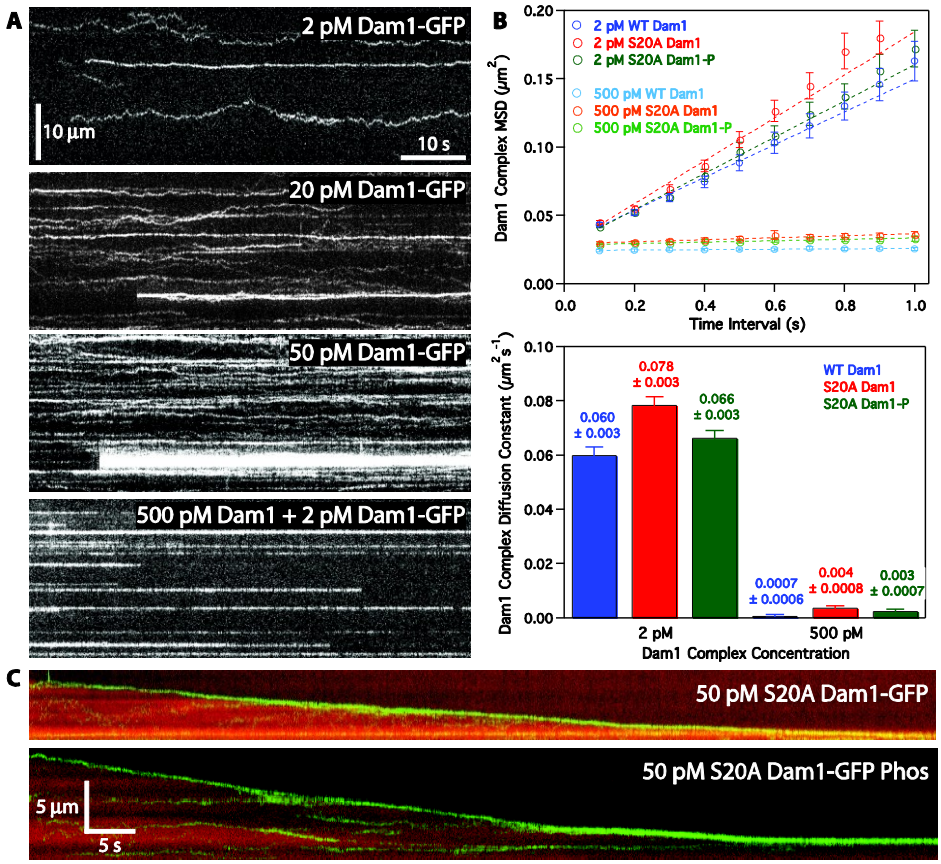

Figure 2.5: The Dam1 complex oligomerizes on microtubules and tracks with disassembling tips.
(A) Representative kymographs showing changes in Dam1 complex behavior as it oligomerizes on microtubules. At 2 pM GFP-tagged Dam1 complex, single monomers were discernable. At 20 and 50 pM, slowly diffusing oligomers were seen as lines. At 500 pM Dam1 complex, the behaviors of individual oligomers were traced by visualizing a small proportion of labeled complex. Concentrations are of free complexes in solution. (B) Oligomerization of Dam1 complex slows its diffusion on taxol-stabilized microtubules and oligomerization of S20A Dam1 complex is not abolished by Ipl1 phosphorylation. Top: Mean-squared displacement (MSD) is plotted against time for 2 pM WT Dam1 complex (blue markers, n = 188), 2 pM S20A Dam1 complex (red markers, n = 327), 2 pM Ipl1 phosphorylated S20A Dam1 complex (green markers, n = 346), 500 pM wild-type (WT) Dam1 complex (light blue markers, n = 129), 500 pM S20A Dam1 complex (orange markers, n = 188) and 500 pM Ipl1 phosphorylated S20A Dam1 complex (light green markers, n = 231). At 500 pM Dam1 complex, the behaviors of individual oligomers were traced by visualizing a small proportion of labeled complex. Markers are mean values ± s.e.m. Dotted lines show the weighted linear fits used to determine diffusion constants, D. Bottom: Diffusion constants derived from MSD versus time plots are summarized as a bar graph. WT Dam1 complex (blue bars), S20A Dam1 complex (red bars), and Ipl1 phosphorylated S20A Dam1 complex (green bars). Error bars denote s.e.m. (C) Representative two-color kymographs demonstrating the tip-tracking ability of Ipl1 phosphorylated S20A Dam1 complex. Movement of 50 pM GFP-tagged unphosphorylated and phosphorylated S20A Dam1 complex (green) is shown on disassembling microtubules (red).

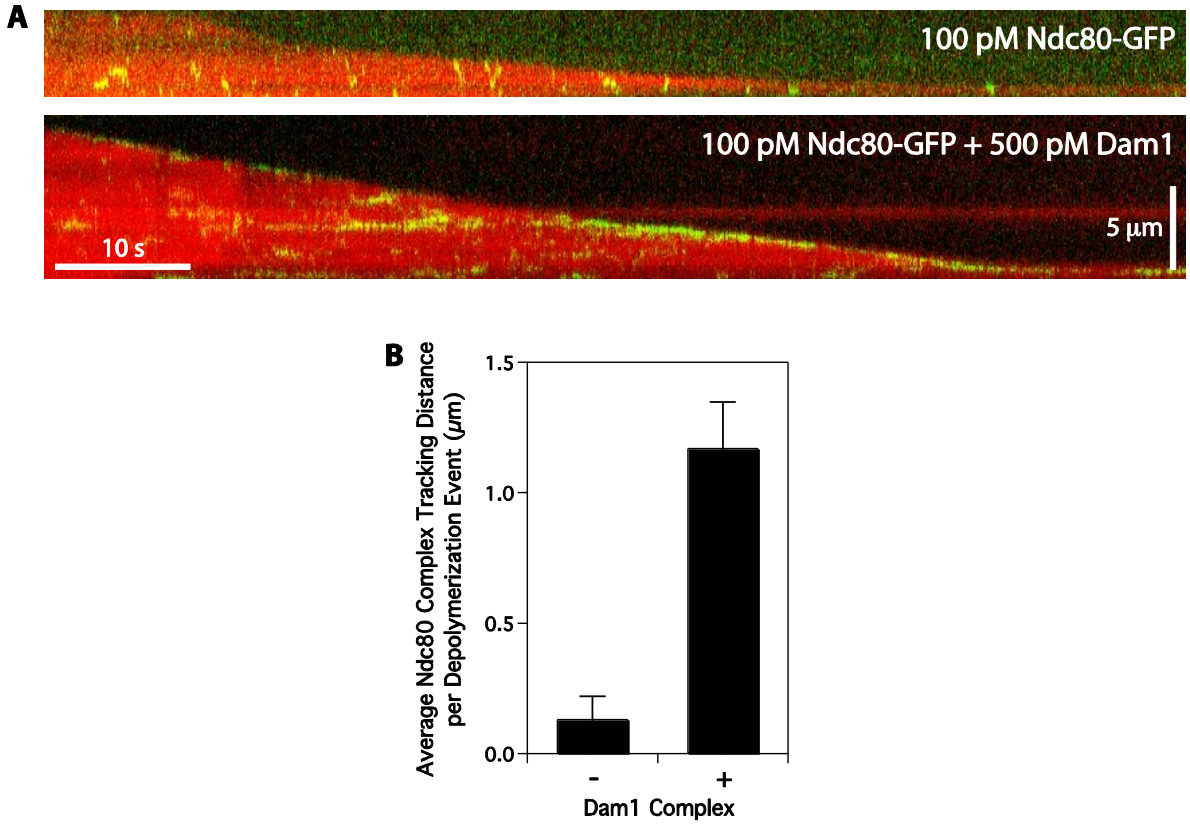

Figure 2.6: Ndc80 complex tracks with disassembling tips in the presence of Dam1 complex.
(A) Representative two-color kymographs showing the tip-tracking ability of Ndc80 complex (100 pM) in the presence or absence of Dam1 complex (500 pM). Movement of GFP-tagged Ndc80 complex (green) is shown on disassembling microtubules (red). Concentrations are of free complexes in solution. (B) Average tracking distance of Ndc80 complex per depolymerization event in the absence of Dam1 complex (n = 19) or in the presence of 500 pM Dam1 complex (n = 62). Bars are mean values ± s.e.m.

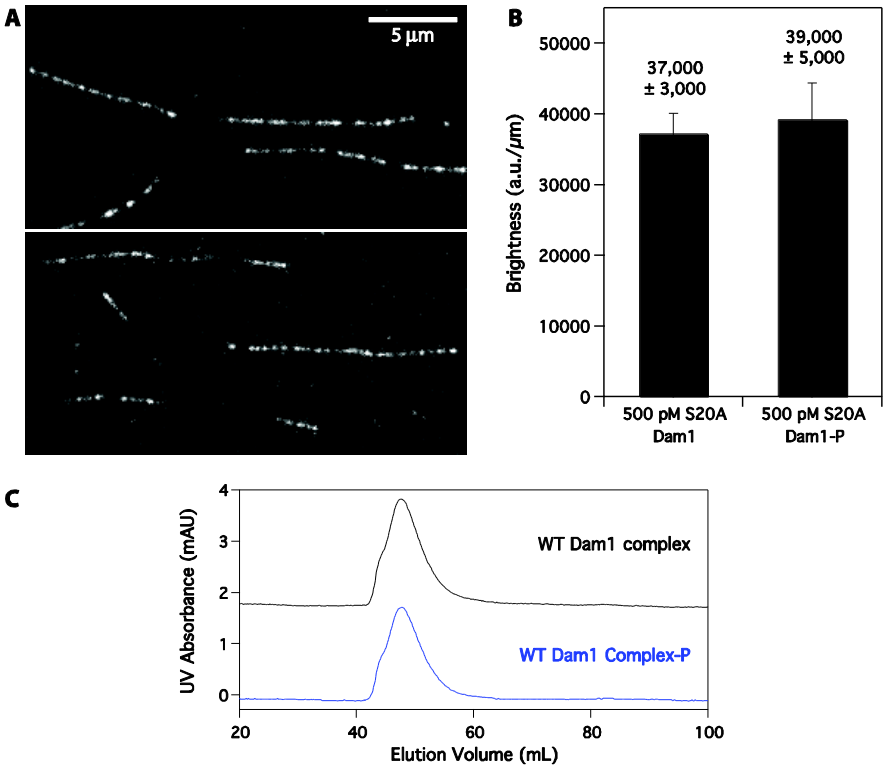

Figure 2.7: Phosphorylation does not affect microtubule binding of S20A Dam1 complex, and does not cause disassembly of wild-type Dam1 complex.
(A) Representative images of mCherry-tagged S20A Dam1 complex on microtubules. Top: 500 pM S20A Dam1 complex. Bottom: 500 pM Ipl1 phosphorylated S20A Dam1 complex. (B) Image averages of mCherry brightness per unit length microtubules for unphosphorylated (n = 6 images representing 68 microtubules, totaling 790 µm) and phosphoryated (n = 7 images representing 51 microtubules, totaling 754 µm) S20A Dam1 complex. Bars are mean values ± s.e.m. (C) Unphosphorylated and Ipl1 phosphorylated wild-type Dam1 complexes each migrate as a single peak during gel filtration, and elute at a volume consistent with previously reported values (Gestaut et al., 2008). The elution profile for unphosphorylated Dam1 complex is offset vertically by 2 mAU.

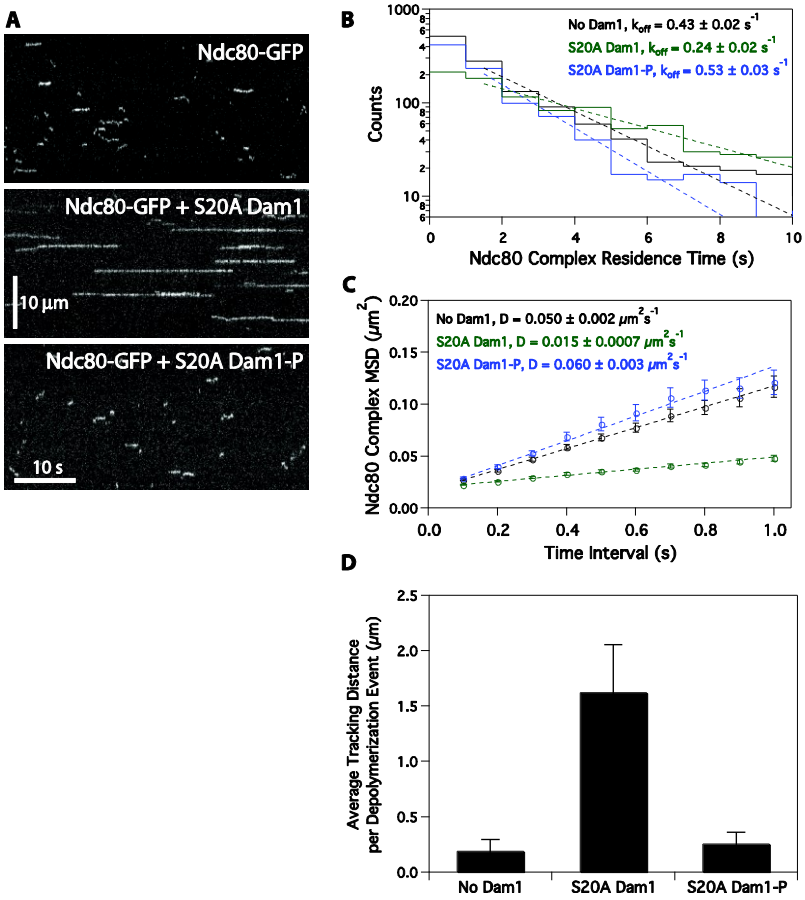

Figure 2.8: Ipl1 phosphorylation of the Dam1 complex regulates its interaction with the Ndc80 complex.

(A) Representative kymographs showing changes in behavior of the Ndc80 complex (10 pM) with the addition of S20A Dam1 complex (500 pM) with or without Ipl1 phosphorylation. Concentrations are of free complexes in solution. (B) Residence time distributions of Ndc80 complex (10 pM) on microtubules without Dam1 complex (black histogram, n = 1266 events), with 500 pM S20A Dam1 complex (green histogram, n = 1081), and with 500 pM Ipl1 phosphorylated S20A Dam1 complex (blue histogram, n = 974). Dotted lines show the weighted exponential fits used to determine dissociation rate constants, k_{off}. (C) Mean-squared displacement (MSD) is plotted against time for Ndc80 complex (10 pM) on microtubules without Dam1 complex (black markers, n = 1102), with 500 pM S20A Dam1 complex (green markers, n = 1030), and with 500 pM Ipl1 phosphorylated S20A Dam1 complex (blue markers, n = 860). Markers are mean values ± s.e.m. Dotted lines show the weighted linear fit used to determine diffusion constant, D. (D) Average tracking distance of 100 pM Ndc80 complex per depolymerization event in the absence of Dam1 complex (n = 19), in the presence of 500 pM S20A Dam1 complex (n = 28), or in the presence of 500 pM Ipl1 phosphorylated S20A Dam1 complex (n = 39). Bars are mean values ± s.e.m.

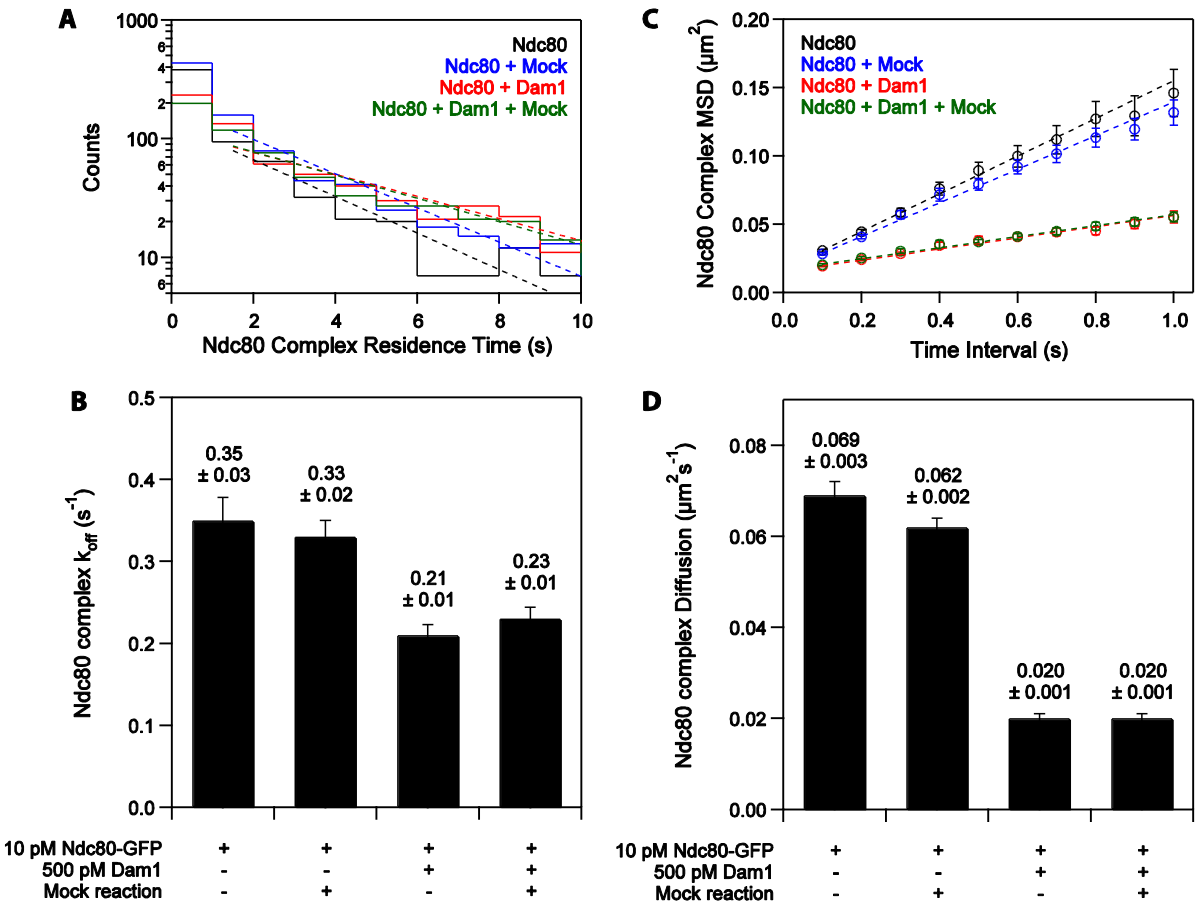

Figure 2.9: Residual components of Ipl1 phosphorylation reactions have no effect on the behavior of the Ndc80 complex on microtubules.
Mock Ipl1 phosphorylation reactions were performed with BSA in place of Dam1 complex, and added to TIRF assays at concentrations as in Fig. 6 (63 pM Ipl1, 63 pM Sli15, and 1.3 μM ATP). (A) Residence time distributions of GFP-tagged Ndc80 complex (10 pM) on microtubules alone (black histogram, $n = 692$), with mock reaction (blue histogram, $n = 869$), with 500 pM Dam1 complex (red histogram, $n = 752$), and with 500 pM Dam1 complex and mock reaction (green histogram, $n = 699$). Dotted lines show the weighted exponential fits used to determine dissociation rate constants, k_{off}. (B) Dissociation rate constants derived from histograms are summarized as a bar graph. Bars are mean values ± s.e.m. (C) Mean-squared displacement (MSD) is plotted against time for GFP-tagged Ndc80 complex (10 pM) on microtubules alone (black markers, $n = 472$), with mock reaction (blue markers, $n = 670$), with 500 pM Dam1 complex (red markers, $n = 636$), and with 500 pM Dam1 complex and mock reaction (green markers, $n = 586$). Markers are mean values ± s.e.m. Dotted lines show the weighted linear fits used to determine diffusion constants, D. (D) Diffusion rate constants derived from MSD versus time plots are summarized as a bar graph. Bars are mean values ± s.e.m.

Chapter 3.

Kinetochores require oligomerization of the Dam1 complex to maintain microtubule attachments against tension and promote biorientation

Introduction

Accurate chromosome segregation is mediated by kinetochores, which physically link replicated chromosomes to the bipolar mitotic spindle. During mitosis, kinetochores utilize microtubule tip dynamics to transduce mechanical forces required for chromosome biorientation and segregation. In the budding yeast *Saccharomyces cerevisiae*, the heterodecameric Dam1 complex is responsible for coupling kinetochores to microtubule ends and for maintaining these attachments during biorientation, when tension is applied across the kinetochores assembled on sister chromatid pairs (JANKE *et al.* 2002; SHIMOGAWA *et al.* 2006; TANAKA *et al.* 2005). *In vitro*, the Dam1 complex spontaneously assembles into oligomeric rings that encircle microtubules, and it has long been hypothesized that the ability to adopt this ring conformation is critical for its roles in kinetochore-microtubule attachment (EFREMOV *et al.* 2007; GRISHCHUK *et al.* 2008a; MIRANDA *et al.* 2005; WESTERMANN *et al.* 2005). However, ring formation is not required for the Dam1 complex to track with disassembling microtubule ends in the absence of applied tension *in vitro* (GESTAUT et al. 2008). Thus, it remains unclear whether oligomerization is required for any specific functions of the Dam1 complex, or even if oligomeric rings exist at kinetochores during mitosis.

The Dam1 complex is required for kinetochores to sustain attachments to microtubule ends against high forces, and to modify microtubule tip dynamics to promote attachment stability (AKIYOSHI *et al.* 2010; FRANCK *et al.* 2007; SARANGAPANI *et al.* 2013). It binds to kinetochores via direct interaction with the Ndc80 complex on microtubules (LAMPERT *et al.* 2010; TIEN *et al.* 2010). To address whether oligomerization is important for any of these functions, we used a Dam1 subcomplex that lacks the ability to assemble into oligomeric rings on microtubules, as determined by negative-stain electron microscopy (MIRANDA *et al.* 2007). Deletion of the gene encoding Hsk3 causes the remaining nine components of the Dam1 complex to split into two subcomplexes. One of these contains six proteins – Dam1, Duo1, Spc34, Spc19, Dad1, and Dad3 – and binds microtubules *in vitro*. This is the "Oligomerization-Deficient" Dam1^{OD} complex used in this study. The other three components (Ask1, Dad2, and Dad4) form the second subcomplex, which does not bind microtubules (MIRANDA *et al.* 2007).

Using *in vitro* biochemical and biophysical assays, we found that the Dam1^{OD} complex represents a clean separation of functions: it retains an intact microtubule-binding site, but is deficient in oligomerization. We identified a striking defect of the Dam1^{OD} complex in coupling to disassembling microtubule tips against applied tension. Finally, we asked if oligomerization of the Dam1 complex is required *in vivo*. As every component of the Dam1 complex is essential for viability (WESTERMANN *et al.* 2007), an Hsk3 degron system was used to transiently generate the Dam1^{OD} complex in yeast cells. Consistent with our *in vitro* observations, kinetochore-microtubule attachments in these cells failed during bipolar alignment of sister chromatids, resulting in mitotic arrest. Our work provides compelling evidence for a specific and essential function of oligomerization at the kinetochore-microtubule interface.

Results

Microtubule-binding and oligomerization are separable functions of the Dam1 complex

Miranda and coworkers (MIRANDA *et al.* 2007) previously reported a stable, six-protein Dam1 subcomplex that cosediments with microtubules, but is unable to assemble into oligomeric rings. We corroborated and expanded these findings to verify this Oligomerization-Deficient $Dam1^{OD}$ complex retains a functional microtubule-binding domain in the absence of oligomerization. Using total internal reflection fluorescence (TIRF) microscopy (GESTAUT *et al.* 2008; TIEN *et al.* 2010), we imaged single wild-type ($Dam1^{WT}$) and $Dam1^{OD}$ complexes tagged with Dad1-GFP as they bound to microtubules (Figure 3.1A). Distributions of GFP fluorescence intensity were similar for the $Dam1^{WT}$ and $Dam1^{OD}$ complexes, and the magnitude of single photobleach steps in our imaging conditions suggests that these distributions derive from single GFP molecules (Figure 3.1B). Thus, at the low concentrations (5-40 pM) required for single-molecule imaging, both $Dam1^{WT}$ and $Dam1^{OD}$ complexes exist primarily as monomers. Residence time distributions and standard diffusion plots showed that the $Dam1^{WT}$ and $Dam1^{OD}$ complexes exhibit similar microtubule-binding properties (Figure 3.1C-D). We determined single-molecule mean residence times of 5.3 ± 0.5 and 7.0 ± 0.5 s, and diffusion constants of 0.021 ± 0.001 and 0.017 ± 0.001 $\mu m^2 s^{-1}$, for $Dam1^{WT}$ and $Dam1^{OD}$ complexes, respectively. Thus, at the single-molecule level, the oligomerization-deficient Dam1 complex binds microtubules in a manner that is similar to the wild-type complex.

At a higher concentration (2 nM) that supports the formation of oligomeric rings (TIEN *et al.* 2010), $Dam1^{WT}$ complex formed a punctate distribution along microtubules, consistent with its cooperative binding (GESTAUT *et al.* 2008) and its assembly into oligomers (Figure 3.2A). Despite their similar behavior at the single-molecule level, 2 nM $Dam1^{OD}$ complex decorated the

microtubule lattice at a much lower density relative to 2 nM Dam1^{WT} complex (Figure 3.2B). Instead, 20 nM Dam1^{OD} complex was needed to achieve a binding density on microtubules comparable to that of 2 nM wild-type, and the decoration by Dam1^{OD} complex appeared more uniform (Figure 3.2A-B). Thus, the Dam1^{OD} complex is impaired in binding cooperativity, as expected for an oligomerization-deficient species. We visualized individual molecules in these conditions by mixing small ("tracer") quantities of GFP-tagged Dam1 complex with excess un-tagged complex (Figure 3.2C-E). For Dam1^{WT} complex, "tracer" GFP-tagged molecules exhibited long residence times on the microtubule lattice, suggesting their incorporation into oligomers of un-tagged Dam1^{WT} complexes (Figure 3.2C). We note that the residence time of "tracer" Dam1^{WT} complexes, 56 ± 8 s (Figure 3.2F), is comparable to the average single-step photobleaching time in our imaging conditions (51 ± 16 s). Therefore, this measurement likely underestimates the lifetime of oligomeric assemblies of Dam1^{WT} complex on microtubules. By contrast, "tracer" Dam1^{OD} complexes were unaffected by the addition of excess un-tagged Dam1^{OD} complex. The residence time for "tracer" Dam1^{OD} complexes was 7.0 ± 0.6 s (Figure 3.2D,F), indistinguishable from the residence time in the absence of excess un-tagged Dam1^{OD} complexes, 7.0 ± 0.5 s (Figure 3.1C). Thus, the Dam1^{OD} complex does not form stable oligomers on microtubules. Interestingly, the mean residence time of "tracer" Dam1^{OD} complexes increased 1.8-fold (12.5 ± 1.2 s) in the presence of excess unlabeled Dam1^{WT} complexes, indicating that the Dam1^{OD} complex can associate with the Dam1^{WT} complex (Figure 3.2E-F). Because the residence time is only doubled, the OD complex must only associate with one or a few Dam1^{WT} complexes and does not form rings. Finally, by combining gel filtration and velocity sedimentation analyses, we estimated the molecular weight of the Dam1^{WT} and Dam1^{OD} complexes to assess oligomerization state in solution. Even at concentrations above 1 μM, the

Dam1^{OD} complex is monomeric in solution (Figure 3.3), while the Dam1^{WT} complex exists primarily as a dimer, as reported previously (TIEN *et al.* 2010; WANG *et al.* 2007).

Unlike the Dam1^{WT} complex, the Dam1^{OD} complex does not dimerize in solution or homo-oligomerize on microtubules. However, the microtubule-binding site of the Dam1^{OD} complex appears intact at the single-molecule level and behaves similarly to a single Dam1^{WT} complex. Therefore, the interfaces that mediate microtubule-binding and oligomerization are contained in structurally distinct modules within the Dam1 complex. These modules can be separated to measure how oligomerization contributes to kinetochore-microtubule attachment *in vitro* and *in vivo*.

Oligomerization of the Dam1 complex is required for the strongest microtubule attachments

An optical trap-based rupture force assay (FRANCK *et al.* 2010; TIEN *et al.* 2010) was used to assess the strength of microtubule attachments mediated by the wild-type Dam1 complex and by the oligomerization-deficient complex (Figure 3.4A-B). Dam1 complexes were loaded onto polystyrene beads at relatively high surface density to promote the formation of oligomers, such that up to ~80 individual complexes could simultaneously interact with the microtubule tip (POWERS *et al.* 2009). Beads coated with Dam1^{OD} complexes yielded a median rupture force similar to that for beads coated with Dam1^{WT} complexes (4.8 and 5.2 pN, respectively). However, there is an extended "tail" on the distribution for Dam1^{WT} complex at very high rupture forces; this tail is absent for the Dam1^{OD} complex (Figure 3.4C, Table 3.1). The maximum rupture force observed for Dam1^{WT} complex, 15.2 pN, is almost two-fold higher than that for the Dam1^{OD} complex, 8.3 pN. This was not an isolated instance, as 13% of all ruptures for Dam1^{WT} complex occurred above the maximum rupture force for the Dam1^{OD} complex

(Figure 3.4C). These findings suggest that oligomerization is required for the formation of strong microtubule attachments.

To further investigate this hypothesis, we performed the rupture force assay in the presence of additional Dam1 complex added free in solution. By design of the assay, free Dam1 complex was unable to load directly onto the bead surface, and could only affect attachment strength by oligomerizing with bead-bound Dam1 complex. Relative to Dam1^{WT} complex on beads alone, the addition of 2 nM free Dam1^{WT} complex significantly increased the proportion of strong attachments (Figure 3.4D, Table 3.1): the median rupture force increased to 6.5 pN, and 30% of all ruptures occurred at high force (above 8.3 pN). In contrast, the behavior of Dam1^{WT} complex on beads was not enhanced by the addition of free Dam1^{OD} complex (Figure 3.4D), even when 10-fold more was added to compensate for its decreased microtubule decoration seen by TIRF microscopy. Based on our observation that the Dam1^{OD} and Dam1^{WT} complexes can interact directly, we further reasoned that free Dam1^{OD} complex might interfere with oligomerization by the Dam1^{WT} complex. Indeed, the enhancement in strength afforded by free Dam1^{WT} complex was completely negated by simultaneous addition of free Dam1^{OD} complex in solution (Figure 3.4D). Therefore, we propose that the Dam1^{OD} complex acts as a competitive inhibitor in the rupture force assay by "capping" Dam1^{WT} oligomers. Our results demonstrate that oligomers of Dam1 complex are necessary to sustain microtubule attachments against high forces.

Oligomerization is not required for the Dam1 complex to bind kinetochores

In vivo, the Ndc80 to complex is required for the Dam1 complex to associate with kinetochores, which occurs after initial kinetochore capture on the lateral face of spindle microtubules (JANKE *et al.* 2002; LAMPERT *et al.* 2010; TANAKA *et al.* 2005). The Dam1

complex promotes kinetochore-microtubule attachment strength and is required for maturation of these attachments from lateral to end-on (SHIMOGAWA *et al.* 2006; TANAKA *et al.* 2005). Using the optical trap-based rupture force assay, we tested if the Dam1 complex must oligomerize in order to bind the Ndc80 complex and strengthen its attachment to microtubules. As previously reported (TIEN *et al.* 2010), the Ndc80 complex formed weak microtubule attachments (mean rupture force: 2.5 ± 0.2 pN) that were greatly enhanced by the addition of Dam1^{WT} complex (7.4 ± 0.4 pN) free in solution (Figure 3.5A, Table 3.1). The Dam1^{OD} complex also strengthened Ndc80-based attachments (4.8 ± 0.2 pN), albeit to a lesser extent than wild-type (Figure 3.5A, Table 3.1). We further asked if the Dam1^{OD} complex could bind to native kinetochore particles isolated from budding yeast, and strengthen their attachments to microtubules *in vitro*. To inactivate endogenous Dam1 complex, kinetochore particles were purified from cells carrying the temperature-sensitive *dad1-1* mutation after being shifted to the restrictive temperature. Consistent with previous work (AKIYOSHI *et al.* 2010; SARANGAPANI *et al.* 2013), wild-type kinetochore particles yielded a mean rupture force of 9.7 ± 1.0 pN, while *dad1-1* kinetochores were much weaker at 2.7 ± 0.2 pN (Figure 3.5B, Table 3.1). The mean rupture force of *dad1-1* kinetochores was partially rescued by the addition of Dam1^{WT} complex to 5.6 ± 0.3 pN (Figure 3.5B, Table 3.1). The Dam1^{OD} complex was less effective but still partially rescued attachment strength to 3.7 ± 0.2 pN (Figure 3.5B, Table 3.1). Thus, oligomerization is not strictly required for the Dam1 complex to transmit load to the kinetochore through the Ndc80 complex.

Oligomerization of the Dam1 complex is critical for stable coupling to disassembling microtubule tips against an applied load

At the kinetochore, the Dam1 complex enhances the strength and processivity of microtubule linkages (LAMPERT *et al.* 2010; TIEN *et al.* 2010). Stable kinetochore-microtubule

coupling is crucial when chromosomes become bioriented by the mitotic spindle, as tension is applied across sister kinetochore pairs. It has long been hypothesized that oligomerization is required for the Dam1 complex to support robust coupling to dynamic microtubule ends against applied mechanical loads (MIRANDA *et al.* 2005; WESTERMANN *et al.* 2005). To test this hypothesis, we programmed the laser trap to apply constant force against Dam1 complexes as they coupled beads to dynamic microtubule tips (ASBURY *et al.* 2006; FRANCK *et al.* 2007). When linked directly to beads, both Dam1^{WT} and Dam1^{OD} complexes were able to maintain attachments to assembling microtubule tips over the course of several minutes (9.9 ± 1.9 and 2.8 ± 0.3 min, respectively) against a constant load of 2.4 pN (Figure 3.6A). During this time, the wild-type and OD complexes had similar effects on microtubule dynamics. Microtubule tips exhibited similar average rates of growth and catastrophe, the transition from assembly to disassembly (Figure 3.6B-C). Following catastrophe events, beads coated with Dam1^{WT} complex coupled to disassembling microtubules for 1.0 ± 0.3 min against the applied force. Furthermore, Dam1^{WT} complex slowed the rate of microtubule disassembly and promoted rescue (the transition from shortening to growth), as previously reported (FRANCK *et al.* 2007) (Figure 3.6B-C). By contrast, beads decorated with Dam1^{OD} complex failed to couple robustly to disassembling tips against force, as evidenced by their detachment within 0.05 ± 0.01 min (3 sec) on average (Figure 3.6A). Dam1^{OD} complex also regulated disassembly speed less effectively, and we were unable to observe any rescue events due to the short lifetime of these attachments (Figure 3.6B-C). Importantly, the Dam1^{OD} complex was impaired in disassembly-driven motility only when acting against an applied force. In the absence of force, every bead tested (n = 15) underwent processive tracking with a disassembling microtubule end. Most beads (13 of 15) tracked disassembly all the way to the stabilized microtubule seed, while only two events ended

in detachment, yielding a mean lifetime of ~5 minutes during disassembly in the absence of force. Thus, the oligomerization-deficient Dam1 complex is strikingly defective in coupling to and regulating the dynamics of disassembling microtubule tips under load.

The oligomerization-deficient Dam1 complex fails to support biorientation *in vivo*

Based on our *in vitro* results, we predicted that the oligomerization-deficient Dam1 complex should localize to kinetochores and bind microtubules *in vivo*, but fail to mediate kinetochore-microtubule attachments against the forces experienced during biorientation. Since deletion of *HSK3* is lethal in budding yeast (KASTENMAYER *et al.* 2006; LI *et al.* 2005), we targeted Hsk3 with an inducible degron system (NISHIMURA *et al.* 2009) to transiently generate the Dam1^{OD} complex *in vivo* (Figure 3.7A-B and Figure 3.8). Degron induction caused cells to arrest with large buds, indicating mitotic arrest and suggesting an essential role for Hsk3 during mitosis. Localization of the two structural modules of the Dam1 complex was tracked in Hsk3-depleted cells using Dad1-GFP (in the microtubule-binding module) and Ask1-YFP (in the oligomerization module). Consistent with the formation of the Dam1^{OD} complex *in vivo*, depletion of Hsk3 decoupled the localization of these two modules. Dad1-GFP retained localization to kinetochores and the mitotic spindle similar to control cells, while Ask1-YFP became delocalized (Figure 3.7A-B and Figure 3.8C-D). To verify that this is a specific outcome of depleting Hsk3, rather than a generic result of disrupting the Dam1 complex, we targeted the degron system to the Dam1 protein (Figure 3.9A-B). Depletion of Dam1 caused both Dad1-GFP and Ask1-YFP to delocalize (Figure 3.7C and Figure 3.9C-D). These findings suggest that the Hsk3 degron system generates a stable Dam1^{OD} complex *in vivo* and does not simply disrupt the entire Dam1 complex.

To ask if oligomerization is required for normal kinetochore-microtubule attachment, cells were depleted of Hsk3 and imaged as they entered mitosis. Upon separation of the duplicated spindle pole bodies, kinetochores (marked by Nuf2-GFP) in control cells aligned symmetrically between the two spindle poles, while in Hsk3-depleted cells, kinetochores often aligned asymmetrically towards one pole (Figure 3.10A-C). Hsk3-depleted cells additionally exhibited abnormal spindle lengths (e.g., Figure 3.10B shows spindle hyper-extension), consistent with the high incidence of spindle breakage observed in an extended degron-induced arrest (Figure 3.11). Asymmetric kinetochore clustering towards one pole is inconsistent with a lack of kinetochore-microtubule attachment, which causes unclustering of kinetochores in the nucleus (ANDERSON *et al.* 2009; DE WULF *et al.* 2003; JANKE *et al.* 2001; PINSKY *et al.* 2006). Instead, this asymmetric kinetochore clustering phenotype suggests a defect in sister kinetochore biorientation (JANKE *et al.* 2002; TANAKA *et al.* 2002). To quantify asymmetry in the kinetochore distribution, we developed a "kinetochore intensity ratio" metric. Nuf2-GFP fluorescence intensity was integrated across the two halves of each spindle (Figure 3.10A-B), and a ratio was taken of the brighter side over the dimmer side (and is thus always ≥ 1). For control cells, this ratio was narrowly distributed around the average of 1.1 ± 0.02, indicating accurate bipolar segregation of kinetochores with high fidelity (Figure 3.10D-E). By contrast, kinetochore intensity ratios for Hsk3-depleted cells varied widely (from 1.0 to 14) and averaged 3.3 ± 0.6, reflecting a strong bias towards monopolar alignment that was evident across all observed spindle lengths (Figure 3.10D-E). Therefore, the equal partitioning of kinetochores during mitosis requires oligomerization of the Dam1 complex.

To directly test for a defect in sister kinetochore biorientation, we visualized individual sister centromere pairs in Hsk3-depleted cells. Consistent with the asymmetric distribution of

kinetochores, the majority of Hsk3-depleted cells (83%) had a monopolar *CEN3* pair, while only 17% contained a *CEN3* pair in a bipolar state (Figure 3.12). Of the bipolar *CEN3* pairs, 31% collapsed to monopolar attachments within 30 minutes of observation (Figure 3.12C and Figure 3.13). These events provide direct evidence for microtubule attachment failure by one kinetochore of the sister pair. In control cells, weak or erroneous attachments were rarely observed. Among 112 cells, only one (1%) contained a monopolar CEN3 spot, and the remaining (99%) bioriented *CEN3* (Figure 3.12D). Furthermore, nearly all cells (99%) with *CEN3* biorientation maintained stable separation of the sister pair over the entire imaging period (Figure 3.12D). Therefore, the kinetochore biorientation defect in Hsk3-depleted cells directly supports predictions based on our *in vitro* experiments. Taken altogether, our findings suggest that oligomerization of the Dam1 complex is required for stable coupling of kinetochores to dynamic microtubule ends under tension *in vivo*.

Discussion

The Dam1 complex spontaneously assembles into oligomers *in vitro*, and forms rings that encircle microtubules. The functional consequences of oligomerization have remained unclear. One possibility is that oligomerization merely increases the avidity by allowing multiple Dam1 complexes to simultaneously contact the microtubule. Another non-mutually exclusive possibility is that oligomerization forms a structure with a specialized interaction with microtubule ends. For example, in its oligomeric ring conformation, the Dam1 complex is proposed to hook onto curled protofilaments at disassembling microtubule ends, thereby harnessing mechanical energy from the "conformational wave" of microtubule disassembly (EFREMOV *et al.* 2007; KOSHLAND *et al.* 1988; MANDELKOW *et al.* 1991; MOLODTSOV *et al.* 2005). However, oligomerization of the Dam1 complex has not been shown to be required for its

functions either in forming direct attachments to dynamic microtubule ends *in vitro*, or in mediating these linkages at kinetochores *in vivo*.

We addressed this question by using a version of the Dam1 complex that does not form oligomeric rings *in vitro* (MIRANDA *et al.* 2007). Here, we show that this version of the Dam1 complex retains wild-type microtubule-binding behavior at the level of single complexes, but lacks the ability to assemble into oligomers of any size, and is thus "Oligomerization-Deficient" (Dam1^{OD} complex). In our optical trap assays, we found that oligomerization is required *in vitro* for the Dam1 complex to form microtubule attachments that are robust against applied mechanical loads. Due to the design of the assay, these functions must be independent of binding avidity. Linking Dam1 complexes to the surface of polystyrene beads artificially imposes avidity; however, avidity alone is insufficient to rescue the functional defects of the Dam1^{OD} complex. Therefore, oligomerization of the Dam1 complex contributes to the strength and processivity of microtubule coupling in a manner that is independent of binding avidity. Our data suggest that oligomerization allows the Dam1 complex to adopt a unique conformation that is required for its function at the kinetochore-microtubule interface.

We tested this hypothesis *in vivo* using an Hsk3 degron system to generate the oligomerization-deficient Dam1 complex in cells. We found that depletion of Hsk3 releases the oligomerization module of the Dam1 complex from its microtubule-binding module, indicating successful formation of the Dam1^{OD} complex *in vivo*. In Hsk3-depleted mitotic cells, bipolar centromere pairs collapsed to monopolar attachments. This microtubule attachment failure at one kinetochore of the sister pair can be explained directly by our *in vitro* results. The Dam1^{OD} complex is unable to mediate stable coupling to dynamic microtubule ends under tension. Following breakage, sister pairs remained attached in a monopolar state *in vivo*, consistent with

the ability of the Dam1^{OD} complex to maintain attachments in the absence of tension *in vitro*. Thus, in the absence of oligomerization, the microtubule-binding ability of the Dam1 complex alone is insufficient to support stable kinetochore-microtubule attachment under tension *in vivo*.

Our findings additionally suggest that oligomerization of the Dam1 complex can be regulated by controlling Hsk3 levels. Cells entering meiosis specifically suppress *HSK3* expression among the genes encoding members of the Dam1 complex, and this regulation appears to promote the proper segregation of chromosomes during meiosis I (MILLER *et al.* 2012). We speculate that regulation of *HSK3* might produce the Dam1^{OD} complex as the biologically-relevant form of the Dam1 complex during meiosis I.

Outside of fungal organisms, homologs of the Dam1 complex have not been identified; however, the Ska complex is a proposed functional equivalent in higher eukaryotes, and has been reported to form oligomeric structures *in vitro* (WELBURN *et al.* 2009). Moreover, we and others have found that the human Ndc80 complex has evolved the ability to oligomerize (ALUSHIN *et al.* 2010; MILLER *et al.* 2008; UMBREIT *et al.* 2012). Interestingly, the human Ndc80 complex is thought to oligomerize "longitudinally" on microtubules, binding along individual protofilaments (ALUSHIN *et al.* 2010). This form of oligomerization could provide functions distinct from those afforded by "lateral" oligomerization (binding around the tube, as seen in Dam1 complex rings). The experiments presented here provide a framework to study how oligomerization contributes to kinetochore-microtubule coupling in other systems. Ultimately, we show that oligomerization is an important mechanism by which kinetochore components are coordinated to form a robust microtubule attachment site.

Materials and Methods

Protein expression and purification

All ten components of the *S. cerevisiae* Dam1 complex were co-expressed in *E. coli* from a polycistronic vector (MIRANDA *et al.* 2005). The complex was affinity-purified using a C-terminal His_6- or FLAG-tag on Spc34 and subjected to gel filtration, as previously described (FRANCK *et al.* 2007; GESTAUT *et al.* 2008; TIEN *et al.* 2010). The expression vector was also modified to remove the gene encoding Hsk3; purification as carried out for the wild-type complex then yielded the six-protein oligomerization-deficient Dam1 complex, as previously reported (MIRANDA *et al.* 2007). For TIRF microscopy experiments, the Dam1 complex was tagged by fusion of GFP to the C-terminus of Dad1 (GESTAUT *et al.* 2008). The *S. cerevisiae* Ndc80 complex was expressed in and purified from *E. coli* as reported previously (POWERS *et al.* 2009; TIEN *et al.* 2010; WEI *et al.* 2005). Native kinetochore particles were purified from asynchronously growing *S. cerevisiae* cells using Dsn1-His_6-FLAG, as previously described (AKIYOSHI *et al.* 2010; SARANGAPANI *et al.* 2013).

TIRF microscopy

Flow chambers were constructed and functionalized to immobilize taxol-stabilized microtubules on the coverglass, as reported previously (GESTAUT *et al.* 2010; GESTAUT *et al.* 2008; POWERS *et al.* 2009; TIEN *et al.* 2010). Single-molecule imaging experiments were carried out by incubating 5-40 pM $Dam1^{WT}$ or $Dam1^{OD}$ complex with Alexa-647-labeled microtubules. GFP and Alexa-647 fluorescence channels were simultaneously recorded using a custom TIRF imaging system (GESTAUT *et al.* 2010). In "tracer" assays, GFP-tagged and unlabeled versions of the Dam1 complex were pre-mixed at a 1:100 ratio to a total concentration of 2 nM ($Dam1^{WT}$ complex) or 20 nM ($Dam1^{OD}$ complex) and subsequently incubated with microtubules. All TIRF

assays were performed in BRB80 (80 mM PIPES, 120 mM K^+, 1 mM $MgCl_2$, and 1 mM EGTA, pH 6.9) containing 1 mg·ml^{-1} κ-casein, and supplemented with an additional 70 mM KCl and an oxygen scavenger system (200 μg·ml^{-1} glucose oxidase, 35 μg·ml^{-1} catalase, 25 mM glucose and 5 mM DTT).

Single-particle tracking and analysis was performed using custom software (available upon request) developed in Labview (National Instruments) and Igor Pro (Wavemetrics) as reported previously (GESTAUT *et al.* 2008; POWERS *et al.* 2009; TIEN *et al.* 2010). Average binding densities of Dam1^{WT} and Dam1^{OD} complex on microtubules (Fig. S1b) were measured using the line scan function in ImageJ (NIH). Photo-bleaching experiments were carried out by non-specifically adsorbing GFP-tagged Dam1 complexes to the coverglass at a density of ~100 complexes per field of view (1150 μm^2) and imaging under conditions identical to those used in single-molecule experiments. Automated analysis of single-step photo-bleach events was performed by fitting a heavy-side step function to records of brightness intensity over time (custom software developed in Labview, available upon request).

Bootstrapping analysis was used to determine mean residence time and to estimate the error of the mean. Each residence time dataset was randomly resampled with replacement 1000 times. For both Dam1^{WT} and Dam1^{OD} complex, the means of the resampled datasets formed normal distributions. Gaussian fits to these distributions yielded estimates of mean residence time, and the Gaussian width was used as an estimate of the error.

Protein size analysis

Size-exclusion chromatography was carried out using a HiLoad Superdex 16/60 prep grade column (GE Healthcare) equilibrated in Dam1 purification buffer (500 mM NaCl, 50 mM phosphate, pH 6.9). The column was calibrated using BSA, catalase, ferritin, and thyroglobulin

as protein size standards. For velocity sedimentation analysis, a 90-µl sample of 2 µM $Dam1^{WT}$ or $Dam1^{OD}$ complex was loaded onto a 1-ml 8-32% sucrose gradient made in Dam1 purification buffer; BSA, catalase, and aldolase were used as protein size standards.

Optical trap-based bead motility assays

Streptavidin-coated 0.44-µm polystyrene beads (Spherotech) were functionalized with biotinylated anti-His_5 antibody (Qiagen) and decorated with Dam1 complexes via recognition of the His_6-tag on the C-terminus of Spc34, as reported previously (FRANCK *et al.* 2007). Incubation of 11 pM beads with 20 nM Dam1 complex (for ~1 hr at 4°C) yielded a surface density of ~2000 complexes per bead. In this arrangement, we estimate that up to ~80 Dam1 complexes can simultaneously reach from the bead surface to the microtubule end (POWERS *et al.* 2009). Bead decoration was performed in a total volume of 60 µl incubation buffer (BRB80 containing 8 $mg \cdot ml^{-1}$ BSA and 1 mM DTT). Any remaining Dam1 complex not bound to the bead surface was removed by pelleting the beads (16,000x *g* for 10 min at 4°C) and washing with ~200 µl incubation buffer. Beads were returned to the original incubation volume by pelleting (16,000x *g* for 10 min at 4°C) and resuspending in 60 µl incubation buffer. Beads coated with Ndc80 complex were prepared in the same manner as described for Dam1 complex. Kinetochore particles were diluted such that the concentration of Dsn1 was ~0.4 $ng \cdot ul^{-1}$, and then incubated with 6 pM beads for ~1 hr at 4°C, as described previously (AKIYOSHI *et al.* 2010; SARANGAPANI *et al.* 2013).

Flow chambers were prepared to immobilize GMPCPP-stabilized microtubule seeds on the coverglass, as previously described (FRANCK *et al.* 2010; UMBREIT *et al.* 2012). Beads were introduced into the flow chamber in assay buffer (BRB80 containing 8 $mg \cdot ml^{-1}$ BSA, 1 $mg \cdot ml^{-1}$ κ-casein, 1 mM DTT, 1 mM GTP, 1.4 mg ml tubulin) supplemented with an oxygen scavenging

system (250 μg·ml^{-1} glucose oxidase, 30 μg·ml^{-1} catalase, 30 mM glucose). Dynamic microtubule extensions were assembled by the addition of free tubulin dimers onto the coverglass-bound GMPCPP-stabilized microtubule seeds.

A custom optical trap instrument (FRANCK *et al.* 2010) was used to capture and manipulate beads, and to apply force to the attachments between the Dam1 complex and dynamic microtubule ends. Rupture force experiments were performed essentially as described previously (AKIYOSHI *et al.* 2010; SARANGAPANI *et al.* 2013; TIEN *et al.* 2010). Beads were initially attached to microtubules and subjected to a 2.4-pN constant "test" force in the direction of microtubule growth. Beads were required to track microtubule growth over a distance of ~100-500 nm to ensure end-on attachment. After satisfying the test phase, the applied force was increased at a constant rate of 0.25 pN·s^{-1} until bead detachment. Records of force versus time collected during the experiment were used to determine the rupture force, which was marked as the maximum force sustained by the attachment during each event. Some rupture force assays included FLAG-tagged Dam1 complex added free in solution along with the beads; this free Dam1 complex was supplied in the assay buffer.

Constant force experiments were also carried out as previously reported (ASBURY *et al.* 2006; FRANCK *et al.* 2007; POWERS *et al.* 2009). Briefly, beads were attached to assembling microtubule ends, and 2.4 pN was applied continuously (in the direction of microtubule growth) throughout rounds of microtubule assembly and disassembly. Upon bead detachment, microtubule tip state was determined visually during the experiment and confirmed during subsequent analysis using traces of bead position versus time. Attachment lifetime and microtubule dynamic rates were also measured from bead position traces using custom software (available upon request) developed in Igor Pro (Wavemetrics).

For experiments performed in the absence of applied force, beads were tracked by DIC imaging as previously described (ASBURY *et al.* 2006). Beads were bound to the microtubule lattice, and a secondary laser was used to induce microtubule disassembly by ablation of the plus end, as reported previously (TIEN *et al.* 2010; UMBREIT *et al.* 2012). Attachment lifetime was measured from video recordings and was defined as the period over which recognizable disassembly-driven motility occurred.

Yeast culture and live-cell imaging

Strains used in this study are listed in Table 3.2 and are derivatives of SBY3 (W303). NUF2-GFP and SPC110-mCherry (SHIMOGAWA *et al.* 2006), pCUP1-GFP12-LacI and CEN3::33LacO (WARGACKI *et al.* 2010), TUB1-GFP (STRAIGHT *et al.* 1997), and OsTIR1-9myc constructs (NISHIMURA *et al.* 2009) were described previously. ASK1-YFP was created as described (WACH *et al.* 1997). HSK3-3V5-IAA7, DAM1-3V5-IAA7 and DAD1-GFP were constructed by PCR-based methods as reported previously (LONGTINE *et al.* 1998). Primer sequences for strain constructions are available upon request. Auxin-inducible degron alleles were generated by fusing the protein of interest with 3V5-IAA7. 3V5-IAA7 tagging plasmids were kindly provided by Dr. Leon Chan (UC Berkeley).

Cultures were grown at 30°C in yeast peptone dextrose rich (YPD) medium (BURKE *et al.* 2000) to ~30-60 klett. The auxin-inducible degron system (NISHIMURA *et al.* 2009) was activated by addition of 0.5 mM auxin to the growth medium (YPD + auxin). Cells were mounted on agar pads as described previously (MULLER *et al.* 2005) or in a CellAsic (Millipore) microfluidics device and imaged using a DeltaVision system (Applied Precision) fitted with an IX70 inverted fluorescence microscope (Olympus), a Uplan APO 100× objective (1.35 NA), and a CoolSnap HQ camera (Photometrics).

For localization experiments, asynchronously growing cells were collected for imaging on agar pads at designated timepoints after the addition of auxin. Exposures of 0.3 s were recorded for Dad1-GFP or Ask1-YFP in each of nine 0.5-μm optical sections. Automated spot detection was performed using custom Matlab-based software, Fluorcal (SHIMOGAWA *et al.* 2010), available upon request. Cells were counted visually using DIC images taken in the same field of view. Spindle morphology was assessed in asynchronously growing cultures after treatment with auxin for 2 hours. Tub1-GFP and Spc110-mCherry were imaged as described for Dad1-GFP and Ask1-YFP. Spindles were considered broken if no Tub1-GFP fluorescence was oriented along the spindle axis at one or both spindle poles.

Kinetochore biorientation was imaged in synchronized cells using the CellAsic system. Asynchronous cells (~30 Klett units) were loaded into the microfluidics chamber and grown in YPD + 6 μM α-factor medium for 2 hours. Auxin was then introduced by exchanging to YPD + 6 μM α-factor + 0.5 mM auxin medium for 1 hour. Cells were subsequently released from α-factor into YPD + auxin medium and imaged in three 1.5-μm optical sections at 7.5-min intervals from the time of release. Nuf2-GFP and Spc110-mCherry were imaged with exposures of 0.1 s and 0.3 s, respectively. For each cell, a single representative frame in which both spindle poles were in good focus was used to generate a spindle profile. Spindle profiles were generated from maximum intensity projections of the GFP and mCherry channels with the ImageJ line scan tool. Automated analysis was performed on each spindle profile using custom software developed in Igor Pro, and is available upon request. Spindle poles were located using Gaussian fitting, and the spindle midzone was defined as the midpoint between the two poles. GFP fluorescence intensity was then integrated in each half spindle (as defined by the spindle midzone) to obtain the "kinetochore intensity" associated with each spindle pole. The

kinetochore intensity ratio was then determined as the larger kinetochore intensity divided by the smaller; by definition, this ratio is always ≥1. Average spindle profiles were obtained by normalizing spindle length: the spindle pole associated with the larger kinetochore intensity was defined as position 0, and the opposite spindle pole as position 1. GFP intensity was binned in increments of 0.05 along the normalized spindle axis and averaged across all measured spindles.

In *CEN3* biorientation experiments, auxin was added to asynchronous cultures, and live cells were imaged on agar pads at 45-s intervals for up to 30 minutes. LacI-GFP (labeling a lacO array adjacent to *CEN3*) and Spc110-mCherry were imaged with 0.3 s exposures in nine 0.5-µm optical sections, as described above for Dad1-GFP. Biorientation was scored manually after the experiment for all cells in which both spindle poles remained in focus throughout the observation period. Position versus time traces were obtained from four-dimensional automated spot tracking applied to the mCherry and GFP channels using Imaris (Bitplane).

Figures

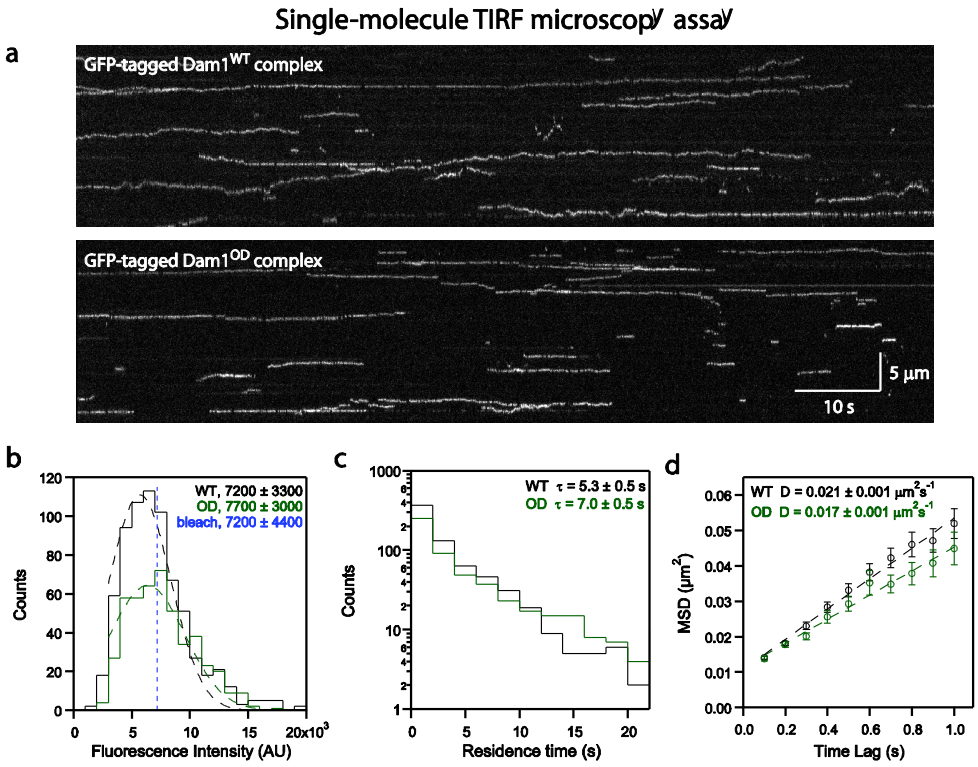

Figure 3.1: The oligomerization-deficient Dam1 complex retains an intact microtubule-binding site.
(A) Kymographs show single molecules of GFP-tagged wild-type (top) and oligomerization-deficient (bottom) Dam1 complex as they bound to and diffused along taxol-stabilized microtubules. Scale bar applies to both kymographs; image contrast adjusted identically. (B) Histograms of GFP brightness intensity for single molecules of wild-type (WT, black trace, n = 717) and oligomerization-deficient (OD, green trace, n = 472) Dam1 complex on microtubules. Dashed blue line indicates the average height of single-step photobleaches under identical imaging conditions (n = 295). Brightness values are reported as mean ± s.d. (C) Residence time distributions for individual WT (n = 717) and OD (n = 564) Dam1 complexes on microtubules. Mean residence time, τ ± s.d. was estimated by bootstrapping analysis (see Materials and Methods for additional details). (D) Mean-squared displacement (MSD) versus time lag for single particles (WT, n = 654; OD, n = 506) represented in (C) and (D). Error bars on each point indicate s.e.m. Dashed lines indicate weighted linear fits to the data, yielding the diffusion constants, D ± s.d. of the fit.

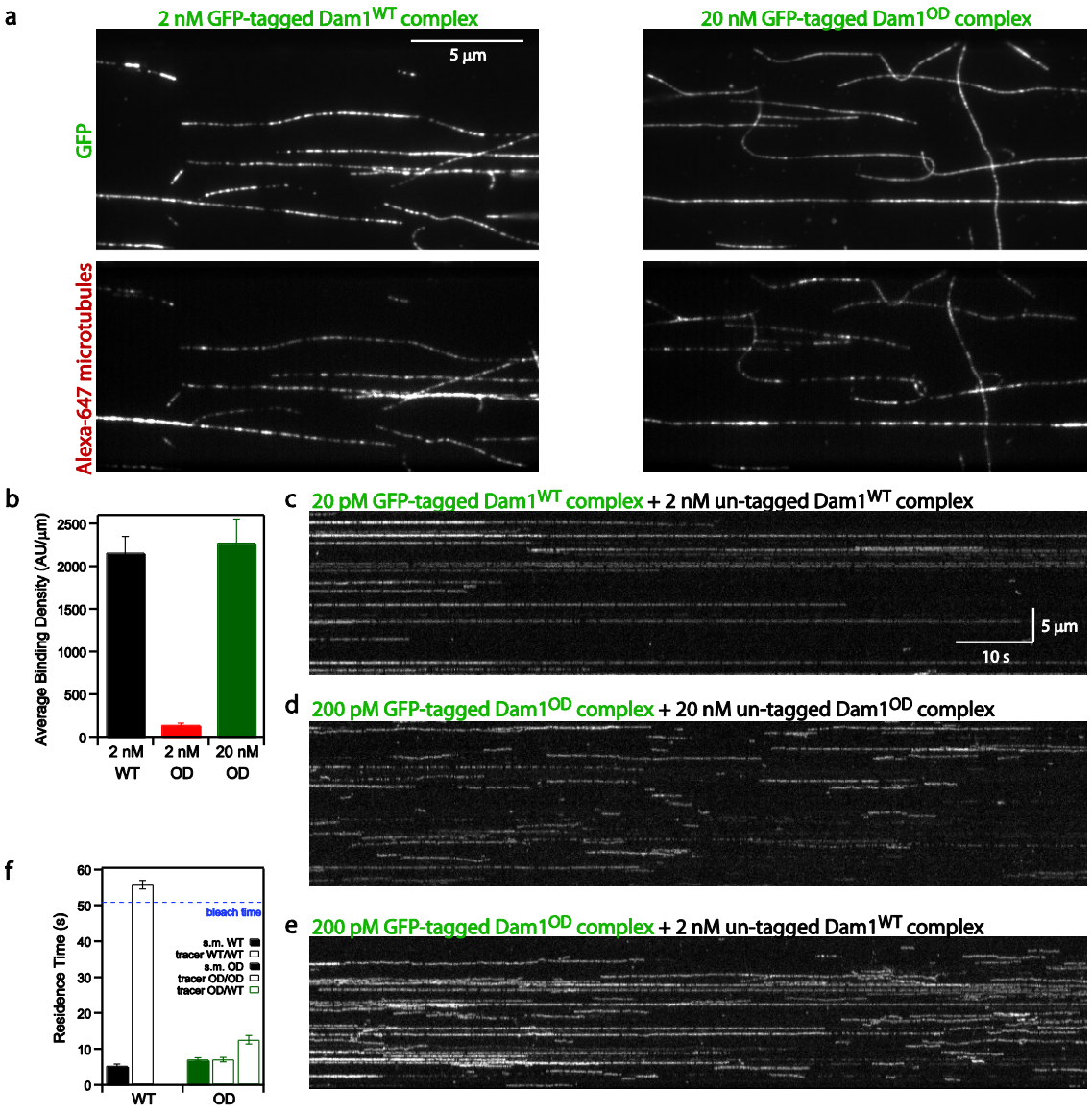

Figure 3.2: The oligomerization-deficient Dam1 complex lacks the ability to oligomerize on microtubules.
(A) TIRF microscopy images of 2 nM GFP-tagged wild-type (left panels) and 20 nM GFP-tagged oligomerization-deficient (right panels) Dam1 complex on Alexa-647-labeled microtubules. Top: GFP channel; Bottom: Alexa-647 channel. (B) Average binding density of GFP-tagged Dam1 complex on microtubules. To match binding density, OD Dam1 complex was added at 10-fold higher concentration than WT. (C-E) Single molecules were imaged in conditions shown in (A) by mixing GFP-tagged and un-tagged Dam1 complexes at a ratio of 1:10 or 1:100. (F) Residence times for "true" single-molecule conditions (solid bars, WT or OD Dam1 complex at 5-40 pM on microtubules, data from Figure 3.1C) are compared to the residence times for "tracer" single-molecules (striped bars) in the conditions shown in C-E. Dashed blue line indicates the average time for single fluorophores to photobleach under identical imaging conditions. Error bars in B indicate s.e.m.; in E, error was estimated using bootstrapping analysis as in Figure 3.1C.

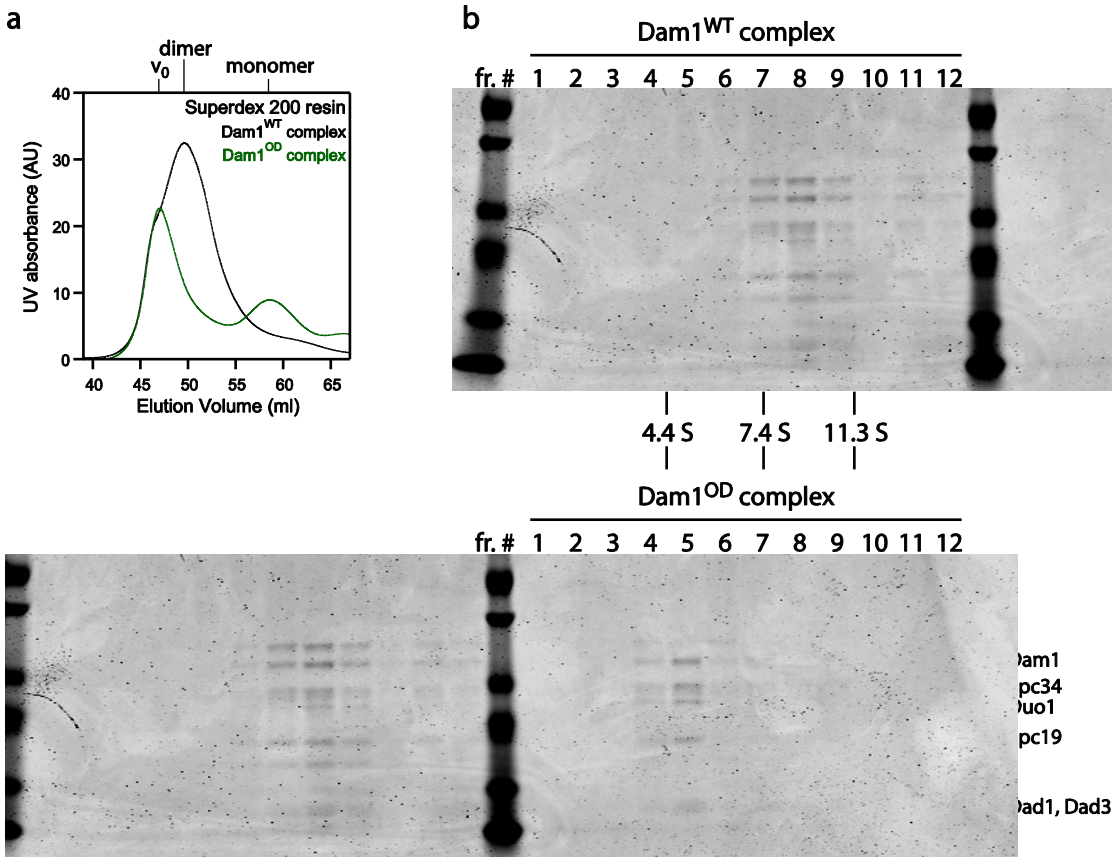

Figure 3.3: The oligomerization-deficient Dam1 complex does not dimerize in solution. (A) Elution profiles from size-exclusion chromatography experiments performed on the wild-type (R_S 8.9 nm; WT, black trace) and oligomerization-deficient (R_S 7.3 nm; OD, green trace) Dam1 complexes. Stokes radii were determined using a standard curve generated from BSA, catalase, ferritin, thyroglobulin. (B) Coomassie-stained SDS-PAGE gels show velocity sedimentation analyses for WT (9.1 S; upper gel) and OD (4.9 S; lower gel) Dam1 complexes. BSA, aldolase, and catalase were used as standards. Data from A and B were combined to estimate molecular weight (SIEGEL and MONTY 1966). In solution, the WT complex is primarily dimeric (observed species is ~340 kDa; monomers are predicted to be ~200 kDa), while the OD complex is monomeric (observed ~150 kDa; predicted ~140 kDa monomer).

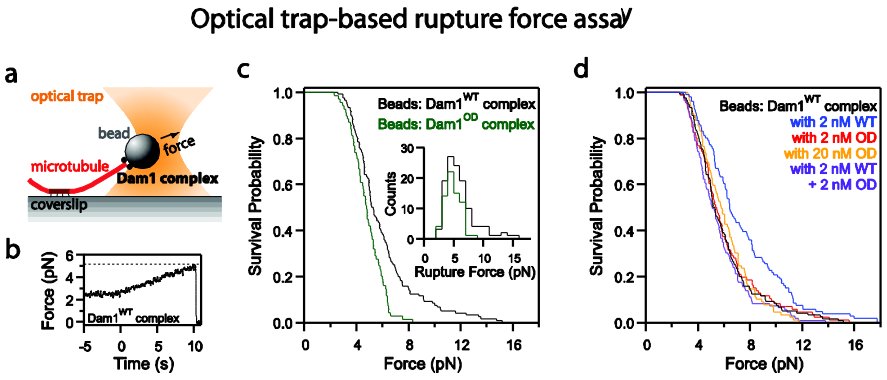

Figure 3.4: Oligomerization of the Dam1 complex enhances microtubule attachment strength.

(A) Diagram of the optical trap assay. (B) Example trace of applied force versus time from the rupture force assay. Beads are subjected to a ~2.5-pN test force prior to initiation of the force ramp (~0.25 pN/s), which begins at t = 0 s. Dashed line indicates the rupture force from this event. (C) Survival versus force curves for beads coated with wild-type (WT, black trace, *n* = 120) or oligomerization-deficient (OD, green trace, *n* = 69) Dam1 complexes coupled to microtubule tips. Inset: same data represented in survival curves but re-plotted as rupture force histograms. (D) Survival versus force curves for beads coated with wild-type Dam1 complex alone (black trace, reproduced from C) or in the presence of additional Dam1 complex free in solution: with 2 nM WT, blue, *n* = 106; with 2 nM OD, red, *n* = 86; with 20 nM OD, orange, *n* = 89; with 2 nM WT and 2 nM OD, purple, *n* =109.

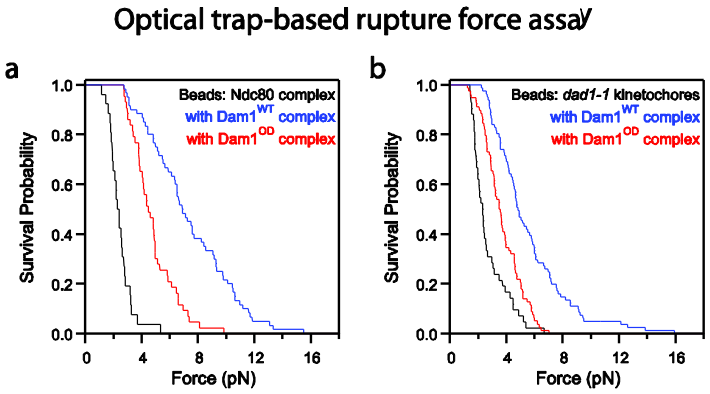

Figure 3.5: The Dam1 complex loads onto the Ndc80 complex and onto kinetochores in the absence of oligomerization.
(A) Survival versus force curves for beads coated with Ndc80 complex alone (black trace, n = 26) or in the presence of free wild-type (WT, blue trace, n = 60) or oligomerization-deficient (OD, red trace, n = 43) Dam1 complex in solution. (B) As in A, using beads instead coated with purified kinetochore particles lacking functional endogenous Dam1 complex (*dad1-1* kinetochores). Beads were assayed alone (black trace, n = 42), and in the presence of purified, recombinant WT (blue trace, n = 81) or OD (red trace, n = 78) Dam1 complex added free in solution.

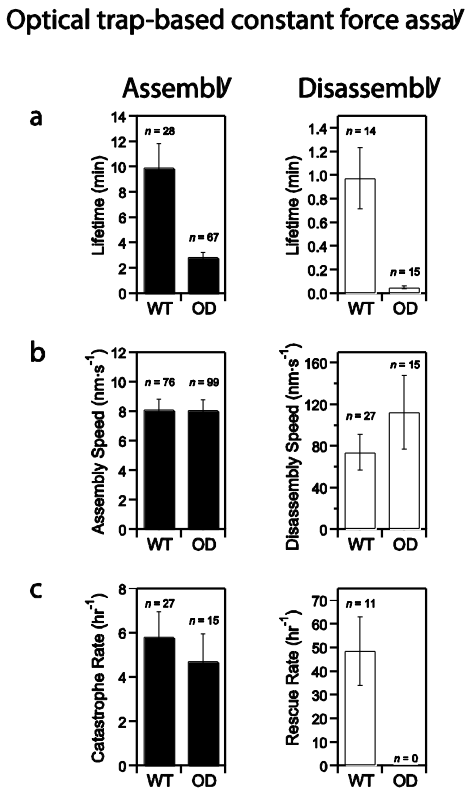

Figure 3.6: The oligomerization-deficient Dam1 complex fails to track with disassembling microtubule tips against applied load.
Beads coated with wild-type (WT) or oligomerization-deficient (OD) Dam1 complex were tracked while they coupled to assembling (left plots) and disassembling (right plots) microtubule tips under a constant force of ~2.4 pN applied in the direction of microtubule assembly. (A) Mean attachment lifetime for beads coupled to dynamic microtubule tips under constant load. (B) Speeds of microtubule tip assembly and disassembly while coupled to beads under constant force. In our assay conditions, the intrinsic rates of microtubule assembly and disassembly are ~6 nm s^{-1} and ~230 nm s^{-1}, respectively (FRANCK *et al.* 2007; UMBREIT *et al.* 2012). (C) Switch rates for microtubule tip state: from assembly to disassembly (catastrophe), and from disassembly to assembly (rescue). For microtubules alone, catastrophes occur at a frequency of ~10 hr^{-1} (FRANCK *et al.* 2010; WALKER *et al.* 1988), and rescues at ~2 hr^{-1} (UMBREIT *et al.* 2012). In A and C, error bars are based on counting statistics; in B, error bars indicate s.e.m.

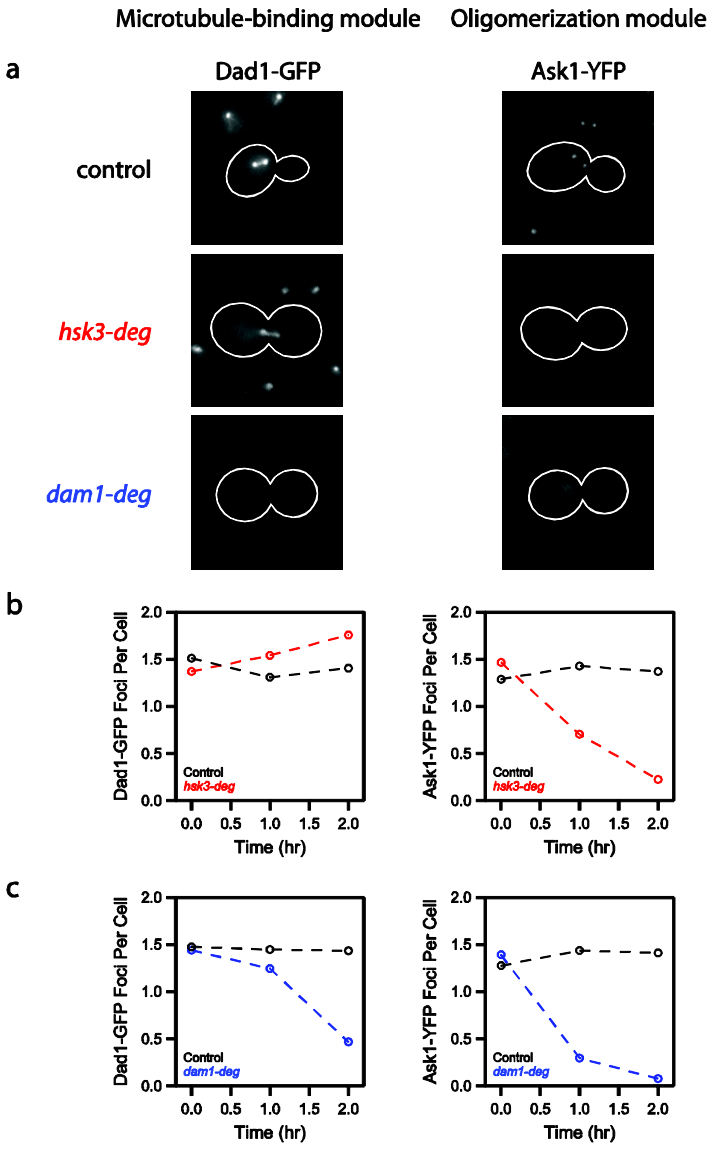

Figure 3.7: Depletion of Hsk3 causes formation of the oligomerization-deficient Dam1 complex *in vivo*.
(A) Representative images of Dad1-GFP and Ask1-YFP in mitotic control (top), *hsk3-degron* (middle), and *dam1-degron* (bottom) cells at 2 hours after addition of auxin. Localization of Dad1-GFP (B) and Ask1-YFP (C) was quantified by automated spot detection and is reported as the average number of detected spots per cell. For both Dad1-GFP and Ask1-YFP, asynchronously growing cells have ~1.4 spots per cell on average, indicating a mix of mitotic (2 spots) and non-mitotic (1 spot) cells. Arrest in mitosis with kinetochore localization causes cells to approach 2.0 spots per cell; delocalization is indicated by a trend towards 0 spots per cell. See Figure 3.8 and Figure 3.9 for the number of cells counted in each condition.

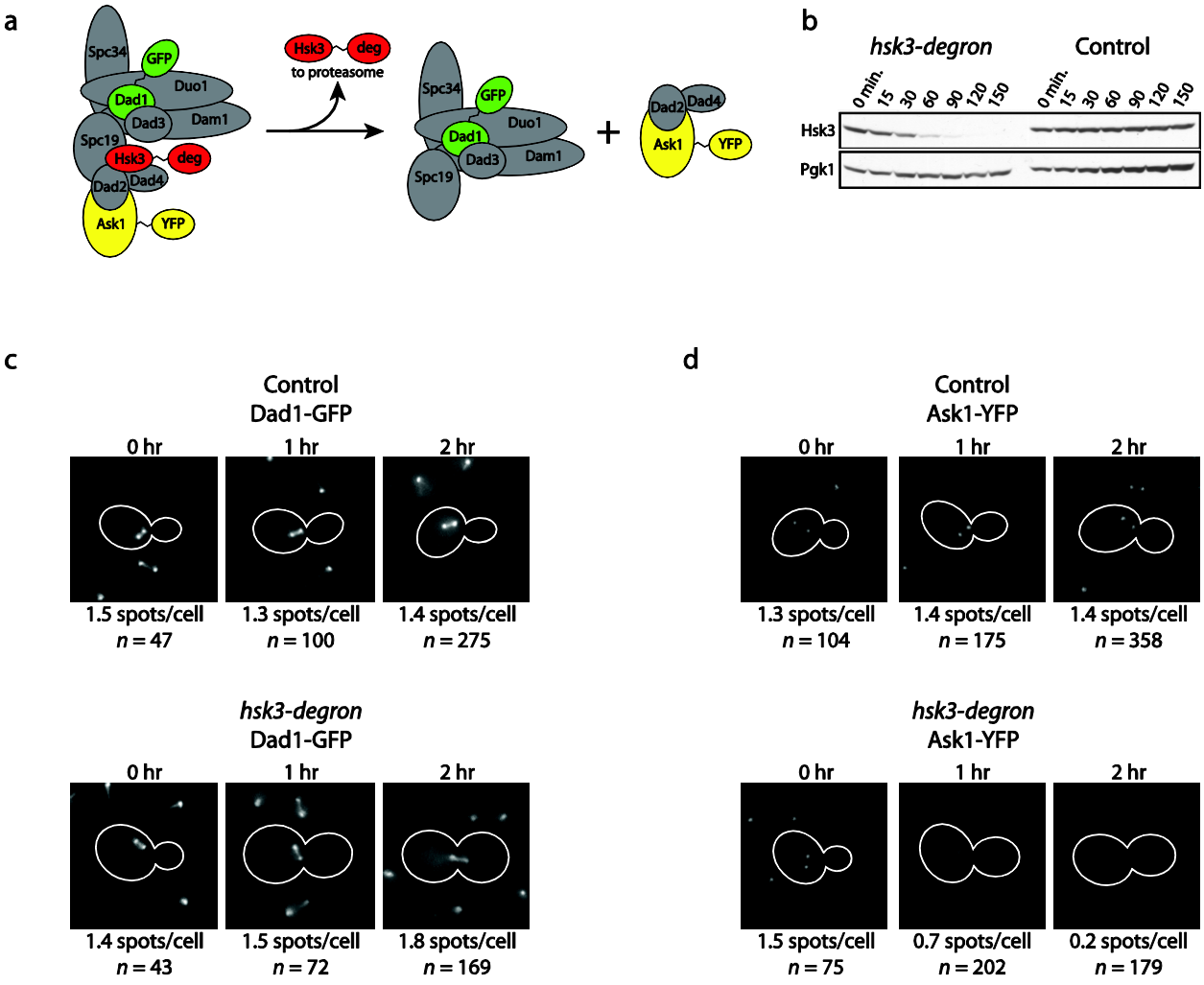

Figure 3.8: An inducible Hsk3 degron system separates the microtubule-binding module of the Dam1 complex from the oligomerization module *in vivo*.
(A) Diagram of the Hsk3 degron system and the predicted separation of the two structural modules of the Dam1 complex *in vivo*. (B) Western blot shows the degradation kinetics of Hsk3 in asynchronously growing *hsk3-degron* and control cells; anti-V5 antibody was used to detect a V5 epitope in the degron tag. Pgk1 was used as a loading control. (C) Representative images of Dad1-GFP in mitotic control (top) and *hsk3-degron* (bottom) cells, in samples taken at the designated times following the addition of auxin to the growth medium. Below each image is the average number of detected spots per cell and the total number of cells observed. Images at 2 hours after addition of auxin are reproduced from Figure 3.7A. Image dimensions are 15 x 15 μm, and contrast was adjusted equally. (D) Analogous to C, but shows representative images of Ask1-YFP in control and *hsk3-degron* cells.

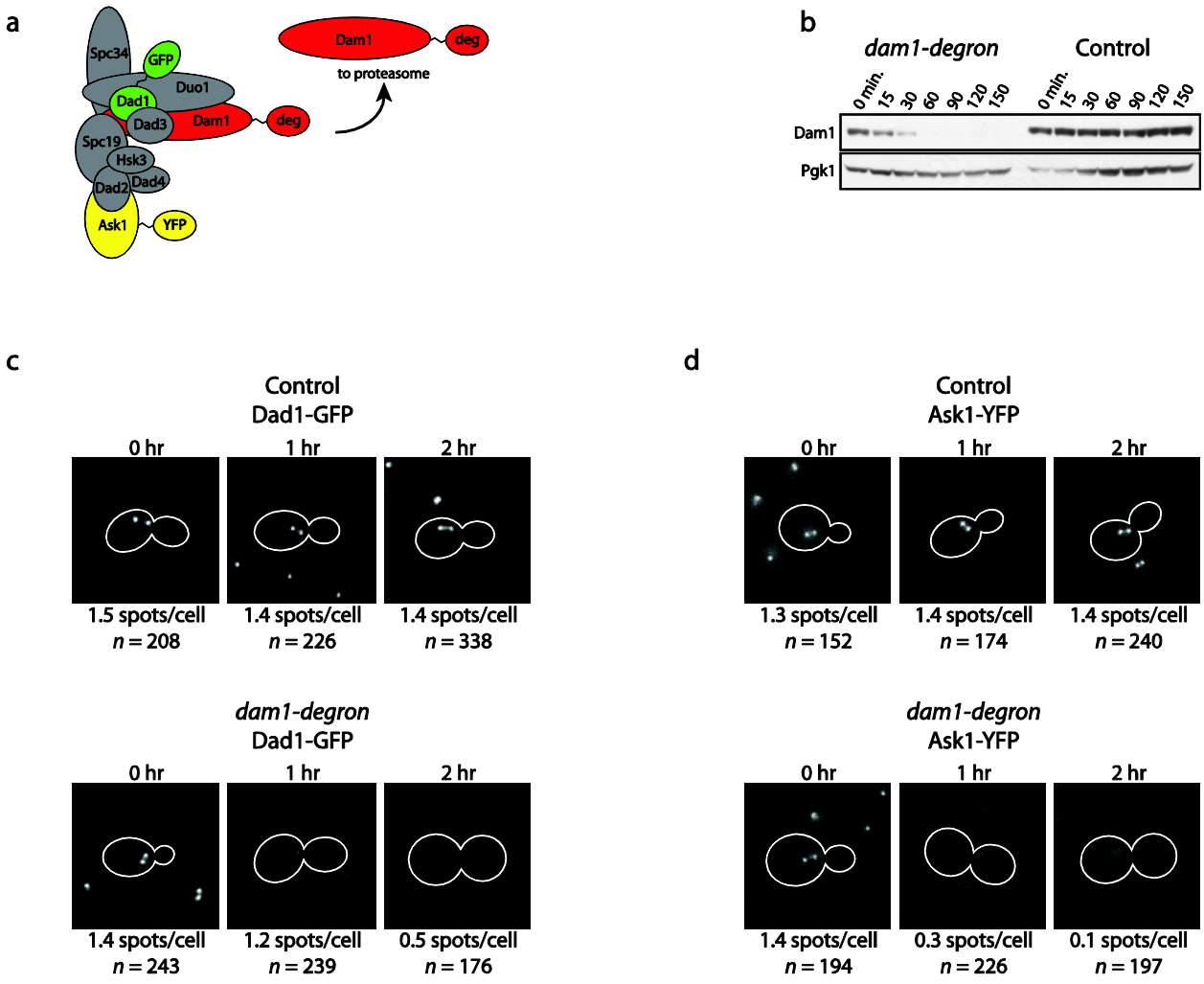

Figure 3.9: Targeting the degron system to the Dam1 protein disrupts localization of both structural modules of the Dam1 complex.
Analogous to Figure 3.8. (A) Diagram of the Dam1 degron system. (B) Western blot shows degradation kinetics of Dam1 in asynchronously growing *dam1-degron* and control cells; anti-V5 antibody was used to detect a V5 epitope in the degron tag. Pgk1 was used as a loading control. Representative images and quantification of spots per cell for Dad1-GFP (C) and Ask1-YFP (D), as in Figure 3.8. Images of *dam1-degron* cells at 2 hours after addition of auxin are reproduced from Figure 3.7A. Contrast was adjusted equally for comparison with images shown in Figure 3.8; dimensions are 15 x 15 µm.

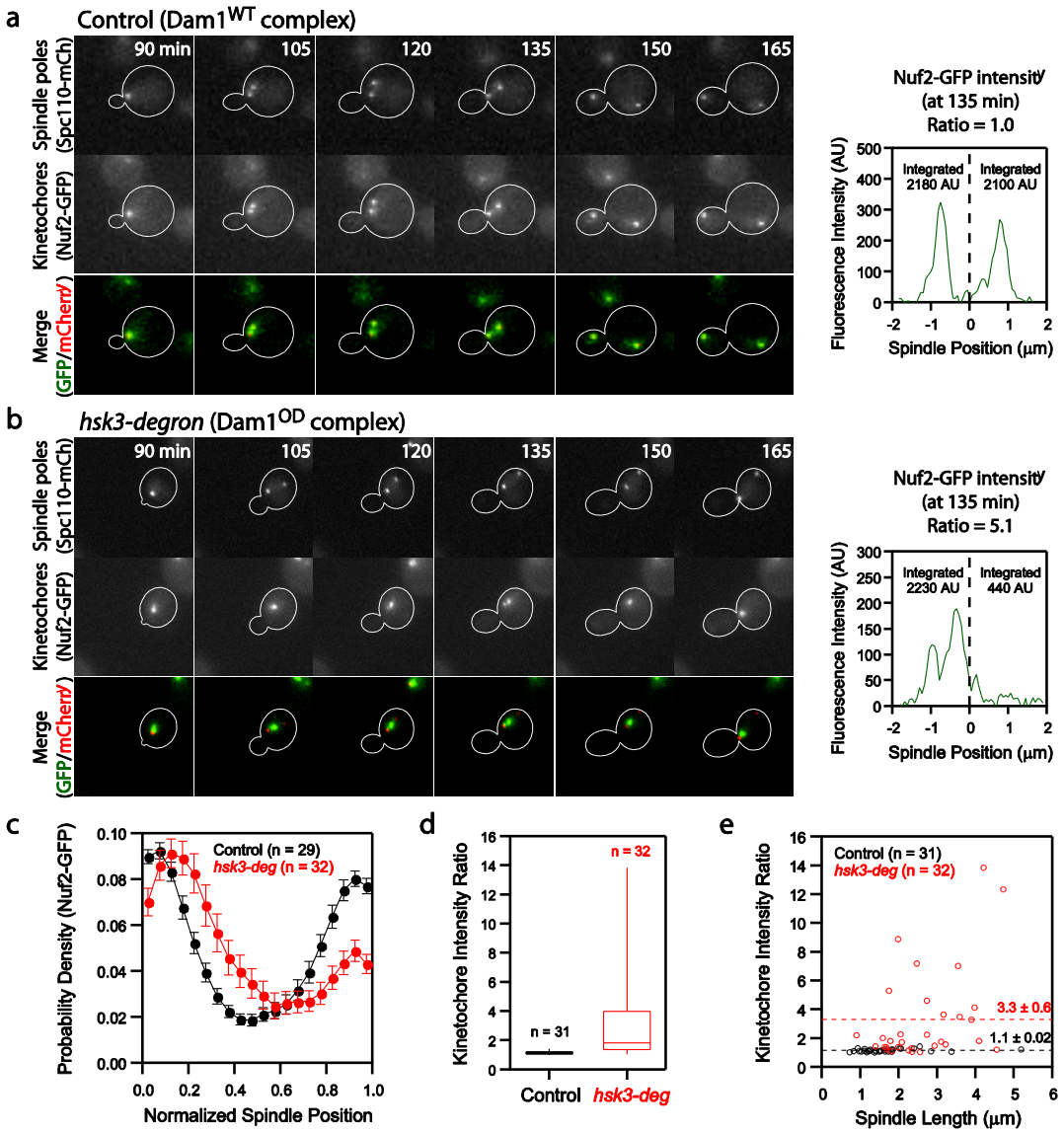

Figure 3.10: Equal bipolar distribution of kinetochores requires oligomerization of the Dam1 complex.

Time-lapse images of spindle poles (Spc110-mCherry, top row), kinetochores (Nuf2-GFP, middle row), and merged channels (bottom row) in control (A) and *hsk3-degron* (B) cells. Cells were imaged immediately following release from α-factor (G1) arrest; time stamps show time after release. Image dimensions are 15 x 15 μm. At right in both A and B are spindle profiles of Nuf2-GFP intensity from corresponding images taken at 135 minutes after release. The integrated intensity in each half-spindle is printed on the plot. (C) Average spindle intensity profiles of Nuf2-GFP in control (black curve) and *hsk3-degron* (red curve) cells. Markers indicate average ± s.e.m. (D) Box and whisker plots show the distribution of kinetochore intensity ratios measured for control and *hsk3-degron* cells. Top and bottom whiskers show 100th and 0th percentiles of the distribution, respectively, while the box shows the 75th, 50th, and 25th percentiles. (E) Plot of kinetochore intensity ratio versus spindle length shows that asymmetric kinetochore alignment in *hsk3-degron* cells is independent of spindle length. See Materials and Methods for additional information about the measurements presented in this figure.

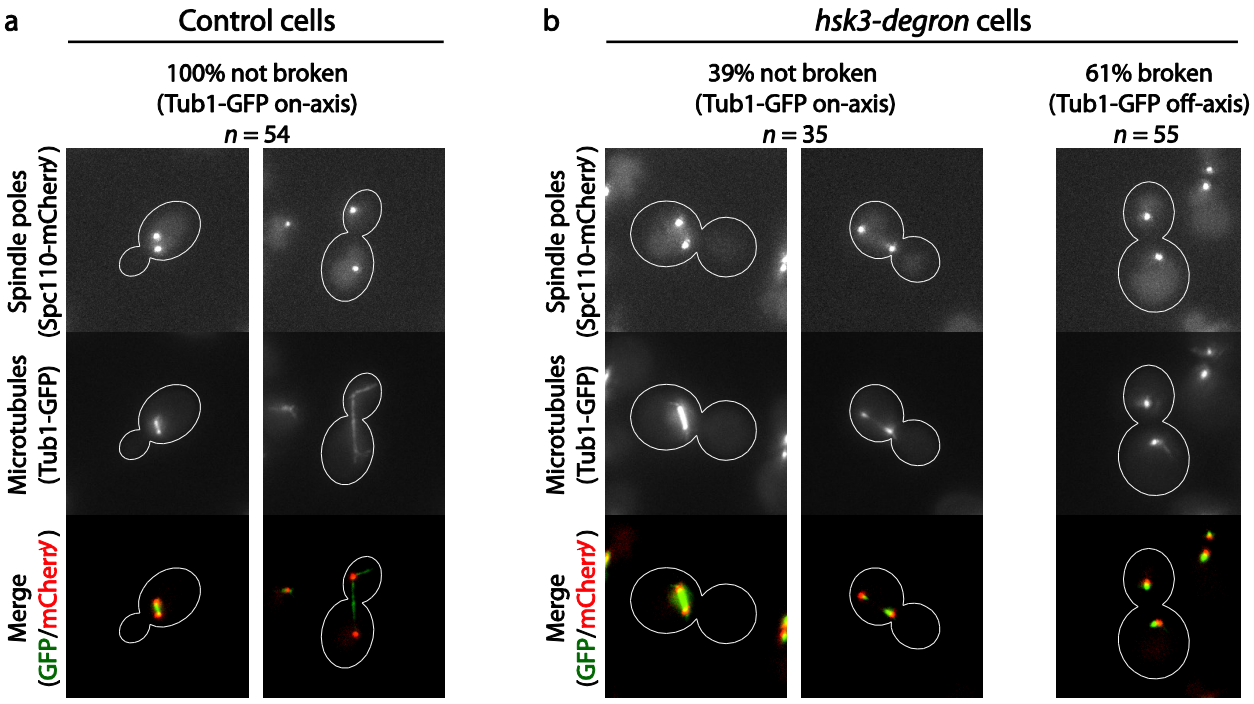

Figure 3.11: Hsk3-depleted cells exhibit spindle morphology defects.
Spindle poles (Spc110-mCherry) and microtubules (Tub1-GFP) were imaged in asynchronously growing control cells (A) and *hsk3-degron* cells (B) after treatment with auxin for 2 hours. Spindle morphology was quantified by the spatial distribution of Tub1-GFP along the spindle axis. Spindles were considered broken if no Tub1-GFP fluorescence was oriented along the spindle axis at one or both spindle poles. Image contrast was adjusted identically in A and B; each image is 15 x 15 μm.

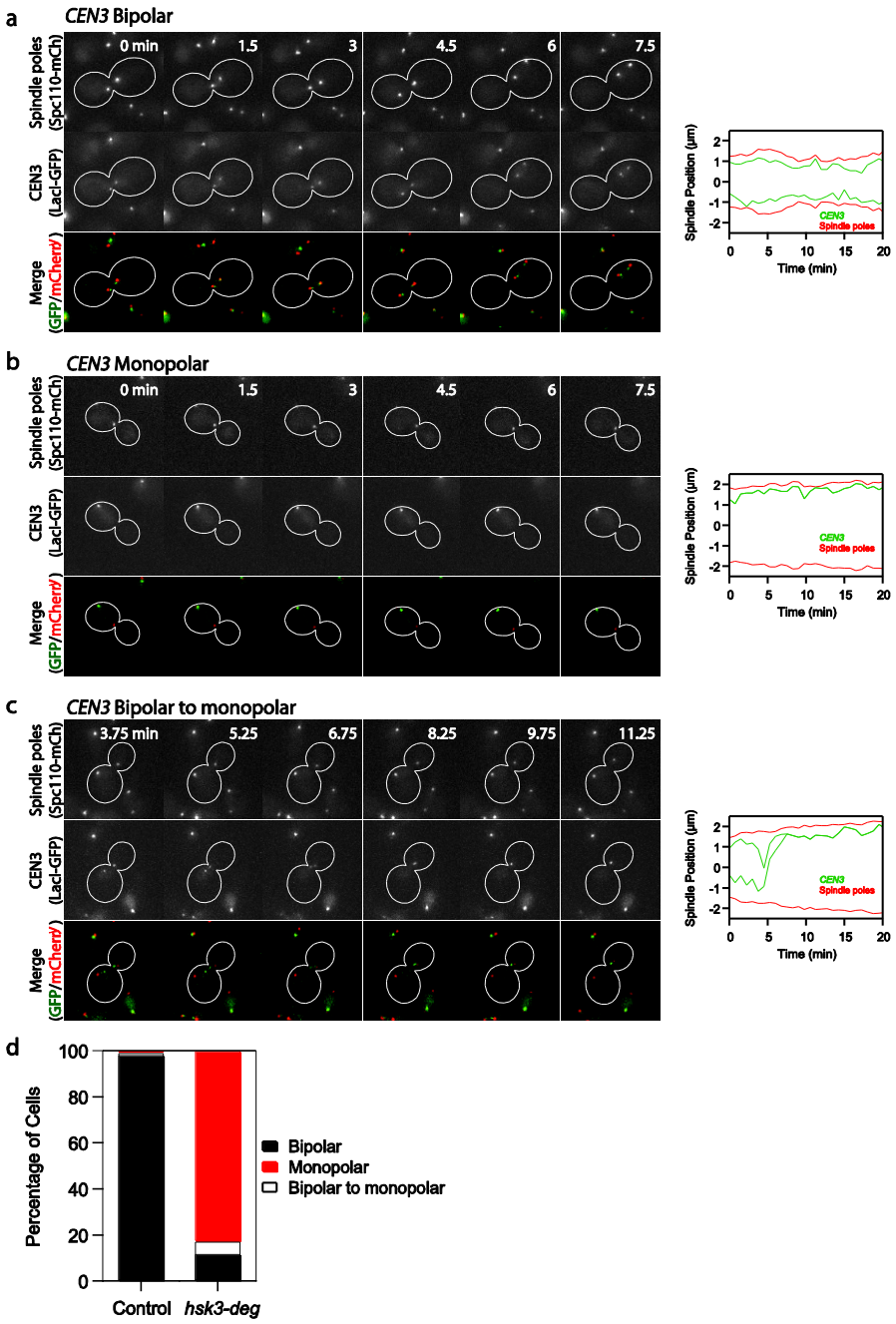

Figure 3.12: The oligomerization-deficient Dam1 complex fails to support bipolar attachment of sister chromatids.
Representative time-lapse images of *hsk3-degron* cells show the three classes of *CEN3* behavior: bioriented (A), monopolar (B), and biorientation failure (C). GFP and mCherry channels are shown separately and merged as in Figure 5. Image dimensions are 15 x 15 µm; contrast was adjusted for visual clarity. Time stamps indicate elapsed time from the start of imaging. Shown to the right in A-C are plots of position versus time for spindle poles (red) and *CEN3* spots (green) from the corresponding time-lapse series. (D) Bar graph shows the fraction cells in each *CEN3* class for control (n = 121) and *hsk3-degron* (n = 168) cells.

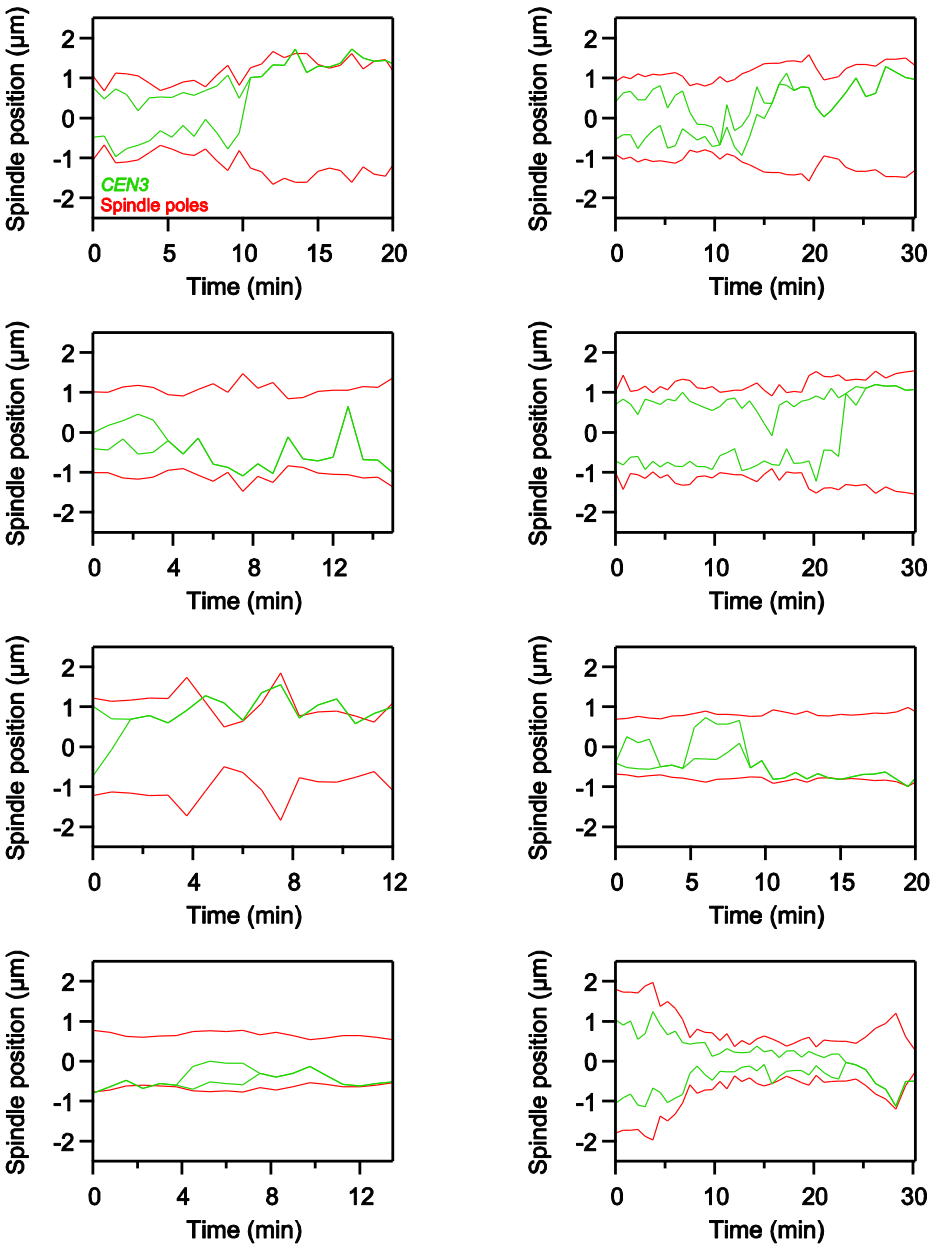

Figure 3.13: Examples of kinetochore-microtubule attachment failure at bipolar *CEN3* pairs in Hsk3-depleted cells.
Related to Figure 3.12C; additional traces of position versus time are shown for spindle poles (red) and *CEN3* spots (green).

	Beads functionalized with:	Dam1 complex added free in solution:	Mean RF (pN)	S.E.M.	Median RF (pN)	No. replicates	Compare versus:	P value (KS test)
1	$Dam1^{WT}$ complex		6.0	0.2	5.2	120		
2	$Dam1^{OD}$ complex		4.8	0.1	4.8	69	1	$4.7x10^{-3}$
3	$Dam1^{WT}$ complex	2 nM WT	7.4	0.3	6.5	106	1	$1.0x10^{-3}$
4	$Dam1^{WT}$ complex	2 nM OD	6.0	0.3	5.4	86	1	0.97
5	$Dam1^{WT}$ complex	20 nM OD	6.1	0.2	5.8	89	1	0.44
6	$Dam1^{WT}$ complex	2 nM WT, 2 nM OD	5.6	0.2	5.1	109	1	0.37
7	Ndc80 complex		2.5	0.2	2.3	26		
8	Ndc80 complex	2 nM WT	7.4	0.4	6.9	60	7	$1.2x10^{-12}$
9	Ndc80 complex	2 nM OD	4.8	0.2	4.5	43	7	$2.5x10^{-9}$
10	*dad1-1* kinetochores		2.7	0.2	2.3	42		
11	*dad1-1* kinetochores	100 nM WT	5.6	0.3	4.8	81	10	$6.8x10^{-11}$
12	*dad1-1* kinetochores	100 nM OD	3.7	0.2	3.5	78	10	$2.7x10^{-5}$

Table 3.1: The rupture force assay reveals how oligomerization of the Dam1 complex contributes to microtubule attachment strength.

Strain	Genotype	Figure
SBY3	*MAT***a** *ura3-1 leu2-3,112 his3-11 trp1-1 can1-100 ade2-1 bar1-1*	-
SBY12423	*MAT***a** *NUF2-GFP:HIS3MX6 SPC110-mCherry:hphMX HSK3-3V5-IAA7:KanMX ura3-1:OsTIR1-9myc:URA3 BAR1 ade3*Δ	Figure 6
SBY12425	*MAT***a** *NUF2-GFP:HIS3MX6 SPC110-mCherry:hphMX HSK3-3V5-IAA7:KanMX BAR1 ade3*Δ	Figure 6
SBY12501	*MAT***a** *pCUP1-GFP12-LacI2:HIS3 CEN3::33LacO:KanMX SPC110-mCherry:hphMX HSK3-3V5-IAA7:KanMX ura3-1:OsTIR1-9myc:URA3 bar1-1 ade3*Δ	Figure 7
SBY12503	*MAT***a** *pCUP1-GFP12-LacI12:HIS3 CEN3::33LacO:KanMX SPC110-mCherry:hphMX HSK3-3V5-IAA7:KanMX bar1-1 ade3*Δ	Figure 7
SBY12504	*MAT***a** *HSK3-3V5-IAA7:KanMX ura3-1:OsTIR1-9myc:URA3 ASK1-YFP:HIS3*	Figure 5a-b, S3
SBY12506	*MAT***a** *HSK3-3V5-IAA7:KanMX ASK1-YFP:HIS3*	Figure 5a-b, S3
SBY12662	*MAT***a** *HSK3-3V5-IAA7:KanMX ura3-1:OsTIR1-9myc:URA3 DAD1-GFP:KanMX6*	Figure 5a-b, S3
SBY12664	*MAT***a** *HSK3-3V5-IAA7:KanMX DAD1-GFP:KanMX6*	Figure 5a-b, S3
SBY12729	*MAT***a** *DAM1-3V5-IAA7:KanMX ura3-1:OsTIR1-9myc:URA3 ASK1-YFP:HIS3*	Figure 5c, S4
SBY12731	*MAT***a** *DAM1-3V5-IAA7:KanMX ASK1-YFP:HIS3*	Figure 5c, S4
SBY12733	*MAT***a** *DAM1-3V5-IAA7:KanMX ura3-1:OsTIR1-9myc:URA3 DAD1-GFP:KanMX6*	Figure 5c, S4
SBY12735	*MAT***a** *DAM1-3V5-IAA7:KanMX DAD1-GFP:KanMX6*	Figure 5c, S4
SBY12750	*MAT***a** *ura3-1::TUB1-GFP:URA3 SPC110-mCherry:hphMX HSK3-3V5-IAA7:KanMX his3-11:OsTIR1:HIS3*	Figure S5
SBY12751	*MAT***a** *ura3-1::TUB1-GFP:URA3 SPC110-mCherry:hphMX HSK3-3V5-IAA7:KanMX*	Figure S5

Table 3.2: Genotypes of strains generated for use in this study.
All strains contain the markers of SBY3 unless otherwise noted.

Chapter 4.

The Ndc80 kinetochore complex directly modulates microtubule dynamics

Introduction

During mitosis, replicated chromosomes are segregated by the mitotic spindle, a bipolar array of dynamic microtubules. Each chromatid is linked to a bundle of microtubules (a "K-fiber") by a kinetochore. To ensure accurate chromosome segregation, regulatory mechanisms detect and correct errors in attachments between kinetochores and spindle microtubules. The conserved Aurora B kinase plays a crucial role in the resolution of aberrant kinetochore-microtubule attachments (LIU *et al.* 2009). Aurora B has many identified targets at the kinetochore, and it is generally thought that phosphorylation of these targets triggers the release of incorrect attachments (BIGGINS and MURRAY 2001; CHEESEMAN *et al.* 2002; CIMINI *et al.* 2006; HAUF *et al.* 2003; PINSKY *et al.* 2006; TANAKA *et al.* 2002). However, emerging evidence suggests that Aurora B activity does not always result in kinetochore-microtubule detachment. For example, early in mitosis when merotelic attachments are more prevalent, phosphorylation of the Ndc80 complex (the key microtubule-binding component of the kinetochore) is relatively high, yet kinetochores do not appear to release from their K-fibers (CIMINI *et al.* 2003; DELUCA *et al.* 2011). Similarly, syntelic attachments formed in the presence of a reversible Aurora B inhibitor are not immediately released when the kinase is reactivated (LAMPSON *et al.* 2004). Instead, the K-fiber microtubules disassemble, carrying the kinetochores back to the centrosome, where the attachments are corrected by an unknown mechanism. These results suggest that

Aurora B additionally acts to regulate microtubule dynamics as a part of its mechanism of error correction.

Additional findings suggest that Aurora B modulates microtubule dynamics through regulation of the Ndc80 complex. A component of the Ndc80 complex, the Hec1 protein, has a disordered N-terminal tail that is targeted by Aurora B *in vivo* (GUIMARAES *et al.* 2008; MILLER *et al.* 2008). In PtK cells, preventing phosphorylation of these target sites not only results in hyper-stable kinetochore-microtubule attachments, but also damped kinetochore oscillations (DELUCA *et al.* 2011). The abnormal oscillations could be explained by direct or indirect contributions from the Ndc80 complex. The Ndc80 complex could itself directly control microtubule dynamics in response to Aurora B activity. An alternative (but not mutually exclusive) explanation is that phosphorylation of Hec1 alters the localization of other factors that modulate dynamics. These may include the microtubule stabilizer EB1 and the microtubule depolymerase MCAK, both of which are also targets of Aurora B (HUNTER *et al.* 2003; JIANG *et al.* 2009; KNOWLTON *et al.* 2006; MANNA *et al.* 2008; TIRNAUER *et al.* 2002; ZHANG *et al.* 2007; ZIMNIAK *et al.* 2009).

Here, we show that the human Ndc80 complex directly stabilizes the tips of disassembling microtubules, slows the rate of disassembly, and promotes microtubule rescue (the transition from microtubule shortening to growth) *in vitro*. By contrast, Ndc80 complex with mutations mimicking Aurora B phosphorylation was impaired in its ability to influence microtubule dynamics, even while tracking with the tips of disassembling microtubules. This diminished ability of the phosphomimetic complex to affect dynamics is not solely a result of weakened microtubule binding, as an N-terminally truncated complex with similar affinity was still able to promote rescue. These results suggest that Aurora B modulates microtubule

dynamics through regulation of the Ndc80 complex, and this mechanism could be separable from effects on attachment stability.

Results

Characterization of full-length human Ndc80 complex

The conserved Ndc80 complex is an essential microtubule-binding component of the kinetochore (KLINE-SMITH *et al.* 2005). While the Ndc80 complex from yeast and worms has been extensively studied *in vitro* (CHEESEMAN *et al.* 2006; LAMPERT *et al.* 2010; POWERS *et al.* 2009; TIEN *et al.* 2010; WEI *et al.* 2006; WEI *et al.* 2005), most work on the human complex has been limited to the use of truncated forms (ALUSHIN *et al.* 2010; CHEESEMAN *et al.* 2006; CIFERRI *et al.* 2008; TOOLEY *et al.* 2011; WEI *et al.* 2007; WILSON-KUBALEK *et al.* 2008). We expressed and purified full-length human Ndc80 complex from *E. coli* for *in vitro* characterization (Figure 4.1). As seen by negative-stain electron microscopy (EM), this recombinant Ndc80 complex bound to taxol-stabilized microtubules (Appendix B, Figure 1A). Using total internal reflection fluorescence (TIRF) microscopy, we visualized single molecules of GFP-tagged Ndc80 complex on taxol-stabilized microtubules (Appendix B, Figures 1B and S2) and measured their dissociation and diffusion rate constants ($k_{off} = 0.21 \pm 0.01$ s^{-1}, $D = 0.018 \pm 0.001$ $\mu m^2 s^{-1}$; Appendix B, Figure 1C-D). The affinity and cooperativity of microtubule binding were measured using a bulk microtubule binding assay that measures the amount of GFP-tagged complex bound to microtubules over varying concentrations of complex (Appendix B, Figure 1E) (GESTAUT *et al.* 2008; GRACZYK and DAVIS 2011). Based on a standard Hill model fit (HILL 1910), the Ndc80 complex binds microtubules with a strong apparent affinity ($K_d = 3.3 \pm 0.2$ nM) and has a Hill coefficient of 2.2 ± 0.2 (Appendix B, Figure 1F). In our binding assay, cooperativity is likely based on interactions between Ndc80 complexes that occur

while they are bound to microtubules. Therefore, we employed a model previously developed by McGhee and von Hippel that describes cooperativity between ligands binding to a polymer lattice (MCGHEE and VON HIPPEL 1974). Fitting the binding data with this model (Appendix B, Figure 1G) also showed a strong apparent affinity (K_d = 8.3 ± 1.5 nM) and cooperativity between Ndc80 complexes on the microtubule lattice (w = 3.4 ± 0.5). As compared to the Hill model fit, the McGhee and von Hippel model fit yielded a weaker apparent K_d for a single complex. Thus, interactions between complexes bound to the microtubule contribute to the K_d predicted by the Hill model. This finding is supported by the observation that at high concentrations, truncated Ndc80 complex binds microtubules in clusters (ALUSHIN *et al.* 2010). Fits to both models revealed a lattice occupancy of ~2 Ndc80 complexes per tubulin dimer, consistent with cryo-EM reconstructions that showed a 4-nm spacing of the truncated complex on microtubules (ALUSHIN *et al.* 2010).

The Ndc80 complex directly stabilizes disassembling microtubule tips and promotes microtubule rescue

In vivo, kinetochores transmit forces generated by the mitotic spindle to drive chromosome movement (KOSHLAND *et al.* 1988). This depends on the ability of microtubule-binding components of the kinetochore to form stable attachments to dynamic microtubule tips. Using TIRF microscopy, we visualized GFP-tagged Ndc80 complex on disassembling microtubules. In these assays, microtubule disassembly was induced by the removal of free tubulin. The human Ndc80 complex can track with disassembling microtubule tips (Appendix B, Figure 2A), unlike the budding yeast Ndc80 complex, which requires the Dam1 complex or oligomerization on the surface of beads (POWERS *et al.* 2009; TIEN *et al.* 2010). The human Ndc80 complex also slowed the rate of microtubule disassembly (Appendix B, Figure 2C); as the

concentration of the complex was increased from 0 to 500 pM, microtubule disassembly was slowed from 280 ± 20 nm/s to 100 ± 10 nm/s.

At 500 pM, bright particles of GFP-tagged Ndc80 complex were observed on microtubules (Appendix B, Figure 2C), consistent with its cooperative binding behavior in our bulk assays. In some cases, disassembly appeared to stall as the tip reached these particles, and only continued after the Ndc80 complex appeared to detach. This behavior resulted in a step-like appearance in kymographs (Appendix B, Figure 2B). Furthermore, Alexa-647-labeled tubulin decorated with Ndc80 complex was often seen bending away from the long axis of the microtubule (observed for 66 ± 10% of microtubules; Appendix B, Figures 2D and S3A-B). Because these curled extensions can be resolved by light microscopy (116-nm pixels), their curvature is gentler than the tight 20-nm curls seen at bare disassembling tips by cryo-EM *in vitro* (MANDELKOW *et al.* 1991). To further investigate tip structure in the presence of Ndc80 complex, we performed a similar disassembly assay and visualized the microtubule tips by negative-stain EM. We observed open protofilament sheets emanating from the tips of microtubules stabilized by Ndc80 complex (Appendix B, Figure 2E). These sheets were not observed at the tips of microtubules stabilized by taxol or by the Dam1 complex (Appendix B, Figure S3C) (WESTERMANN *et al.* 2005). Microtubules exposed to the same conditions in the absence of any stabilizing factor completely disassembled into free tubulin. Although we were unable to distinguish between microtubule plus- and minus-ends in the electron micrographs, curled extensions were observed in the presence of Ndc80 complex at both microtubule ends in the TIRF assay (Appendix B Figure S3A). Together, the TIRF and EM assays suggest that the Ndc80 complex slows disassembly by stabilizing protofilament extensions at microtubule tips.

To test how purified Ndc80 complex couples to dynamic microtubule tips under force, we employed an optical trap-based bead motility assay (FRANCK *et al.* 2010). By incubating 11 pM beads with 5 nM Ndc80 complex (~450 complexes per bead), we estimate up to ~20 complexes can interact with the microtubule tip based on geometric constraints (POWERS *et al.* 2009). This closely approximates the number of Ndc80 complexes per kinetochore microtubule *in vivo* (LAWRIMORE *et al.* 2011). These beads remained coupled to microtubule tips against 2 pN of tension (Figure 4.2A-B), similar to the forces sustained by kinetochore-microtubule attachments *in vivo*, which are estimated to be 0.4 to 8 pN (NICKLAS 1988; PEARSON *et al.* 2001; POWERS *et al.* 2009). Against the applied force, beads tracked robustly with the tips of disassembling microtubules over an average distance of 970 ± 190 nm (n = 44). Consistent with results from our TIRF-based assays, microtubule disassembly was slowed from 230 ± 14 nm/s (for microtubule tips not coupled to beads and in the absence of force) to 44 ± 7 nm/s by beads coated with Ndc80 complex under 2 pN of force (Figure 4.2C). For episodes of disassembly-driven movement against the applied force, about half (53 ± 8%) ended in bead detachment, but a large proportion (40 ± 7%) underwent a microtubule rescue (the remaining events, 7 ± 3%, terminated for other reasons, such as the bead reaching the microtubule seed or non-specifically adhering to the coverslip). Strikingly, disassembling microtubule tips coupled to beads coated with the Ndc80 complex rescued ~70-fold more frequently than bare microtubules (Figure 4.2D; 135 ± 24 hr^{-1} compared to 2 ± 1 hr^{-1}). Therefore, the Ndc80 complex is an effective tip-coupler that can directly slow microtubule disassembly and promote rescue.

By contrast, in our previous work with the budding yeast Ndc80 complex, we observed little effect on the rate of microtubule rescue (POWERS *et al.* 2009). Here we analyzed the dataset reported in Powers *et al*., specifically looking for rescue events. Microtubules rescued at a

frequency of 9 ± 5 hr^{-1} while coupled to beads coated with budding yeast Ndc80 complex (n = 4 rescues, ~100-2700 complexes per bead, against ~1 pN of force). This is close to the rate of rescue for microtubules not coupled to beads (reported above). Therefore, the budding yeast Ndc80 complex, unlike the human complex, appears to have little ability to promote microtubule rescue.

Phosphomimetic mutations in the Ndc80 complex inhibit its ability to influence microtubule dynamics

The Hec1 protein of the Ndc80 complex contains a calponin homology domain that is important for its microtubule binding activity (CIFERRI *et al.* 2008; WEI *et al.* 2007). In addition, Hec1 has a disordered N-terminal tail that contributes to the affinity of the complex for microtubules (GUIMARAES *et al.* 2008; MILLER *et al.* 2008; WEI *et al.* 2007). *In vivo*, the tail is a target for the Aurora B kinase, and mutations that mimic phosphorylation at these sites result in unattached kinetochores (GUIMARAES *et al.* 2008; SUNDIN *et al.* 2011). Consistent with this observation, Aurora B phosphorylation of a truncated Ndc80 complex reduces its binding to microtubules *in vitro* (CIFERRI *et al.* 2008). On the other hand, mutations that block phosphorylation severely damp kinetochore oscillations *in vivo* (DELUCA *et al.* 2011). These findings suggest that phosphorylation in the Hec1 tail is required not only for regulation of kinetochore-microtubule attachments, but also for normal kinetochore-microtubule dynamics. Using the optical trap assay, we tested the direct contribution of the tail to microtubule dynamics *in vitro*. In addition to the wild-type complex, we purified Ndc80 complex with the nine putative Aurora B target sites in the Hec1 tail mutated to aspartic acid to mimic phosphorylation (9D), and Ndc80 complex with the Hec1 tail deleted (ΔN). As a control, we also purified Ndc80 complex with alanine mutations at the Aurora B target sites (9A). Since this construct behaved

like the wild-type complex in our TIRF assays (Appendix B Figures S3B and S4), it was not further characterized in the optical trap assay.

Beads coated with wild-type, 9D, and ΔN complexes were all able to slow the rate of microtubule disassembly in a concentration-dependent manner while tracking with disassembling tips against ~2 pN of applied force (Figure 4.2B-C). However, the 9D and ΔN complexes were impaired relative to the wild-type complex; when incubated with 5 nM of Ndc80 complex, 82 ± 11% of wild-type beads tracked with disassembling microtubule tips, while only 21 ± 5% of the 9D beads and 20 ± 4% of the ΔN beads tracked with disassembly (Figure 4.2B). Furthermore, 5 nM wild-type beads slowed disassembly to 44 ± 7 nm/s, while 5 nM 9D and 5 nM ΔN beads slowed disassembly to 110 ± 20 and 96 ± 27 nm/s, respectively (Figure 4.2C). The ability of the mutant complexes to track with and slow disassembly was recovered to wild-type levels by increasing the density of decoration on beads ~20-fold (Figure 4.2B-C; compare 0.5 and 1 nM wild-type to 10 and 20 nM mutant complexes, respectively). For example, beads coated with 20 nM 9D or 20 nM ΔN complex tracked with microtubules similarly to 1 nM wild-type beads (9D: 76 ± 11%, ΔN: 70 ± 10, wild-type: 74 ± 9%). Therefore, increasing the number of mutant complexes on beads compensates for their decreased coupling performance.

When assayed at comparable coupling performance, the wild-type and ΔN complexes promoted microtubule rescue, but the 9D complex did not (Figure 4.2D-E). Deletion of the Hec1 tail reduced the ability of the complex to promote rescue only modestly (~2-fold). In contrast, phosphomimetic mutations in the tail nearly abolished this activity. Using beads coated with 20 nM 9D complex, we observed only 3 rescue events in 29 minutes of microtubule disassembly, which is an average rescue frequency similar to that for bare microtubules (6 ± 4 versus 2 ± 1 hr^{-}

[1]). In addition, the ΔN complex, but not the 9D complex, stabilized curled extensions at disassembling microtubule tips in the TIRF assay (Figure 4.2F). Thus, phosphomimetic mutations do not simply negate the activity of the tail, but actively interfere with the ability to modify microtubule tip structure and promote rescue.

The ΔN and 9D complexes performed similarly in tracking with and slowing microtubule disassembly, suggesting that their disparate effects on microtubule rescue and tip structure are not due simply to a difference in their microtubule-binding affinities. We quantified binding of GFP-tagged 9D and ΔN complexes directly by single-molecule TIRF microscopy and bulk microtubule binding assays. Unlike the wild-type complex, binding of the mutant complexes was undetectable in standard BRB80 (120 mM K^+) buffer conditions, so the assays were performed in BRB40 (60 mM K^+) buffer. Single molecules of 9D and ΔN complex exhibited similar dissociation and diffusion rate constants (Appendix B, Figure 4A-B; k_{off} = 0.85 ± 0.07 and 0.90 ± 0.05 s^{-1}, and D = 0.060 ± 0.003 and 0.050 ± 0.002 $\mu m^2 s^{-1}$, respectively). In contrast, wild-type Ndc80 complexes dissociated from microtubules ~15-times more slowly (k_{off} = 0.062 ± 0.005 s^{-1}) and diffused on the lattice ~4-times more slowly (D = 0.015 ± 0.001 $\mu m^2 s^{-1}$). It has been previously suggested that the Hec1 tail contributes to microtubule binding by the Ndc80 complex and/or mediates cooperativity between complexes on microtubules (ALUSHIN *et al.* 2010; GUIMARAES *et al.* 2008; MILLER *et al.* 2008). Our results establish that the tail contributes directly to microtubule binding, since deletion of the tail causes individual Ndc80 complexes (in the absence of cooperative binding) to dissociate more quickly from microtubules. In the bulk binding assay, fits to both the Hill and the McGhee and von Hippel models (Appendix B, Figure 4C-D) show that the 9D and ΔN complexes are indistinguishable from one another in their apparent affinities, cooperativity constants, and lattice occupancies (McGhee and

von Hippel fit for 9D and ΔN: K_d = 78 ± 20 and 73 ± 20 nM, w = 7 ± 2 and 7 ± 1, i = 2.4 ± 0.1 and 2.4 ± 0.1 per tubulin dimer, respectively). Therefore, phosphomimetic mutations reduce the affinity of the Ndc80 complex for microtubules and impair its ability to promote microtubule rescue. However, these two effects are not strictly coupled; deletion of the Hec1 tail equally reduces the affinity of the complex for microtubules, but is not as detrimental to its ability to modify microtubule tip structure and dynamics. These findings suggest that Aurora B phosphorylation has separable effects on attachment stability and microtubule dynamics at the kinetochore.

Discussion

The Ndc80 complex directly modulates microtubule dynamics

The Ndc80 complex is a conserved and essential microtubule-binding component of the kinetochore. Here, we characterized the binding of full-length human Ndc80 complex to microtubules *in vitro*. The Ndc80 complex bound cooperatively to microtubules with a strong affinity, and directly promoted microtubule rescue. Our *in vitro* results using unphosphorylated wild-type Ndc80 complex explain observations made in cells. In the absence of Hec1 phosphorylation, we found that the Ndc80 complex antagonizes microtubule disassembly. This effect explains why blocking Hec1 phosphorylation *in vivo* causes hyper-stabilized K-fibers, and leads to damped sister kinetochore oscillations and severe defects in cell division (DeLuca *et al.* 2011). We believe our findings represent the first demonstration that a core component of the human kinetochore directly modifies microtubule rescue rate *in vitro*. This ability has been shown previously for a core kinetochore component only once, with the budding yeast Dam1 complex (Franck *et al.* 2007), which has no known homolog in higher eukaryotes. Notably, the

budding yeast Ndc80 complex does not effectively promote microtubule rescue (POWERS *et al.* 2009), even though the composition and domain structure of the complex are highly conserved.

Our results also indicate a possible mechanism by which the Ndc80 complex promotes microtubule rescue. In the absence of stabilizing factors, protofilaments at disassembling microtubule tips form tight ~20-nm curls (MANDELKOW *et al.* 1991). When microtubules are stabilized by a non-hydrolyzable GTP analog, protofilaments are straighter at disassembling tips (MULLER-REICHERT *et al.* 1998). We found that the tips of disassembling microtubules in the presence of Ndc80 complex were gently curved (as seen by TIRF microscopy) and formed large protofilament sheets (as seen by EM). These observations suggest that the Ndc80 complex promotes microtubule rescue by stabilizing tip structures with straighter protofilaments. Alushin and coworkers proposed that the Hec1 calponin homology domain recognizes the interface between tubulin monomers (ALUSHIN *et al.* 2010), at a putative hinge region (WESTERMANN *et al.* 2005). Our findings are consistent with this model. Ndc80 complex lacking the Hec1 tail was able to modify microtubule tip structure and promote rescue, indicating that other parts of the complex (outside of the tail) are primarily responsible for this activity. We propose that binding of the Hec1 calponin homology domain at the hinge region between tubulin subunits induces a straighter protofilament conformation that facilitates microtubule rescue.

Aurora B regulates microtubule dynamics through the Ndc80 complex

The Aurora B kinase has an established role in releasing aberrant kinetochore-microtubule attachments (LIU *et al.* 2009). Consistent with this model, PtK cells carrying a phosphomimetic mutant Ndc80 (9D) complex have unattached kinetochores (GUIMARAES *et al.* 2008; SUNDIN *et al.* 2011). We found that the human 9D complex bound to microtubules more weakly relative to the wild-type complex as determined by three independent *in vitro* assays: 1)

Single molecules of the 9D complex dissociated more quickly (>10-fold) from the microtubule lattice. 2) In our bulk assays, binding of the 9D complex was undetectable under conditions in which the wild-type complex bound strongly to microtubules. 3) At equal surface density on beads, the 9D complex was impaired in its ability to track with microtubule disassembly against force. In all three of these assays, the 9D complex behaved similarly to and not worse than Ndc80 complex that lacks the tail domain (ΔN). Therefore, mutations that mimic complete phosphorylation of the Hec1 tail prevent the tail from contributing to microtubule binding.

In vivo observations suggest that in higher eukaryotes, Aurora B does not simply trigger kinetochore-microtubule detachment but additionally regulates microtubule dynamics (DeLuca *et al.* 2006; DeLuca *et al.* 2011; Lampson *et al.* 2004). In PtK cells, syntelic kinetochore-microtubule attachments are not lost immediately following Aurora B activation (Lampson *et al.* 2004). Instead, reactivation of Aurora B appears to induce disassembly of the kinetochore microtubules, and the kinetochores track with disassembly back to the centrosome, where the attachments are corrected. Our results offer insight into these observations. At higher surface densities on beads (20 nM), the 9D complex tracked robustly with disassembling microtubule tips against force. Based on geometric constraints (Powers *et al.* 2009), we estimate ~80 complexes can interact with the microtubule tip at this surface density. This is more than the number of Ndc80 complexes per microtubule *in vivo* (~20 per microtubule), but fewer than the number of complexes at a single mammalian kinetochore, which binds 20-25 microtubules through more than 400 attachments (Lawrimore *et al.* 2011; Rieder 1982). Relative to the wild-type complex, the 9D and ΔN complexes are similarly impaired in their binding affinity and tracking performance. However, the ΔN complex promotes microtubule rescue, while the 9D complex does not. Thus, a phosphomimetic Hec1 tail interferes with the ability of the Ndc80

complex to modulate microtubule dynamics, possibly by blocking the ability of the calponin homology domain to stabilize a straighter protofilament conformation. Taken together, these *in vitro* observations explain how phosphorylation relieves microtubule stabilization at syntelic kinetochores to promote K-fiber disassembly, allowing the attached kinetochores to track back to the centrosome.

Here, we show that a conserved core microtubule-binding component of the human kinetochore directly influences microtubule dynamics. In addition, we find that phosphomimetic mutations of essential Aurora B phosphorylation sites in Hec1 not only weaken attachment, but also nearly abolish the ability of the Ndc80 complex to influence dynamics. These effects are separable, and might be independently tunable through phosphorylation of different subsets of target sites in the Hec1 tail. Together, our results indicate that microtubule dynamics can be regulated through Aurora B phosphorylation of the Ndc80 complex.

Materials and Methods

Protein expression and purification

The human Ndc80 complex was co-expressed from two di-cistronic plasmids encoding Spc25/Spc24-His_6 and Hec1/Nuf2 (see Appendix B) in *E. coli* BL21 cells (Rosetta; Novagen). Protein expression and purification were carried out as previously described (POWERS *et al.* 2009).

TIRF microscopy

TIRF microscopy was performed as described above (see Chapter II, Materials and Methods). These assays were performed by my collaborator, Dan Gestaut. See Appendix B for additional details.

Microtubule binding assays

Microtubule binding assays were performed essentially as described (GRACZYK and DAVIS 2011), see Appendix B for a detailed description. These data were provided by my collaborator, Jerry Tien.

Electron microscopy

Electron microscopy data were collected by my collaborators, Jerry Tien, Breanna Vollmar, and Tamir Gonen. Details are provided in Appendix B.

Optical trap bead motility assays

Ndc80 complexes were linked to the surface of polystyrene beads as previously described (FRANCK *et al.* 2010; POWERS *et al.* 2009; TIEN *et al.* 2010). Streptavidin-coated beads (Spherotech) were functionalized with biotinylated anti-His_5 antibodies (Qiagen). His_6-tagged wild-type or mutant Ndc80 complex was incubated at the appropriate concentration (0.5, 1, 5, 10, or 20 nM) with 11 pM beads, rotating for 30 minutes at 4°C. Beads were spun down at 13,200 rpm in a desktop centrifuge for 5 minutes at 4°C, and resuspended in 200 µl assay buffer (BRB80 containing 8 mg ml^{-1} BSA and 1 mM DTT) to wash away unbound Ndc80 complex. The beads were spun again at 13,200 rpm for 5 minutes at 4°C, and resuspended with assay buffer to the original incubation volume.

Flow chambers were constructed and functionalized as previously described (FRANCK *et al.* 2010). First, one flow chamber volume of 1 mg ml^{-1} biotinylated BSA (Vector Laboratories) was introduced and allowed to bind to the glass surface for ~10 min at room temperature. The chamber was then washed twice with ~20 volumes BRB80. Next, ~10 volumes 0.33 mg ml^{-1} avidin DN (Vector Laboratories) was introduced, incubated for ~2 minutes, and washed out with ~20 volumes BRB80. GMPCPP-stabilized biotinylated microtubule seeds were introduced in

BRB80, and allowed to bind to the functionalized glass surface for ~2 minutes. The chamber was then washed with ~20 volumes blocking buffer (BRB80 containing 1 mM GTP, 8 mg ml^{-1} BSA, and 1 mg ml^{-1} κ-casein), followed by a second wash with growth buffer (BRB80 containing 1 mM GTP and 8 mg ml^{-1} BSA). Lastly, Ndc80 complex-coated beads were introduced at an eight-fold dilution from the incubation mix (see above) in a solution of growth buffer containing 1.4 mg ml^{-1} tubulin, 8 mg ml^{-1} BSA, 1 mM DTT, 250 μg ml^{-1} glucose oxidase, 30 μg ml^{-1} catalase, and 4.5 μg ml^{-1} glucose. The edges of the flow chamber were sealed with nail polish to prevent evaporation. Microtubule disassembly events occurred either by a spontaneous switch from assembly to disassembly or by laser scission, as described previously (FRANCK *et al.* 2010). All optical trap assays were performed at 26°C.

Records of bead position versus time were analyzed using custom software written in Igor Pro (available upon request). In order to be considered in the analysis, beads were required to have undergone tracking in the direction of disassembly against the applied force for at least 25 nm. Detachments were scored during the experiment and verified in analysis when the force on a bead under load suddenly dropped to zero, and the bead position trace exhibited "run-away" movement. Microtubule rescues were scored visually during the experiment and verified in analysis by identifying the time at which microtubule disassembly halted. Beads were observed for an additional ~30 seconds to verify that the bead subsequently underwent motion in the direction of microtubule growth at an assembly-limited rate (~10 nm/s) (Fig. 3*A*, top two traces). Intrinsic disassembly and rescue rates for bare microtubules in the absence of force were measured from traces of tip position versus time, as determined from DIC recordings (WALKER *et al.* 1988). We also determined that microtubule rescue was not a result of the disassembling tip reaching the GMPCPP-stabilized microtubule seed; the microtubule lattice was laser-ablated

approximately at the point where rescue occurred, and the microtubule was verified to undergo disassembly back to the stabilized seed. The rescue rate for microtubules was calculated by dividing the number of observed microtubule rescues by the total time of disassembly-driven motility recorded for each assay condition. Disassembly rates were estimated for each event by the slope of a linear fit to the bead position versus time trace, taken over the second half of the entire duration of the disassembly event. Events that lasted less than 2 seconds were not included in disassembly rate analysis due to unreliability in the linear fits over short time intervals.

Figures

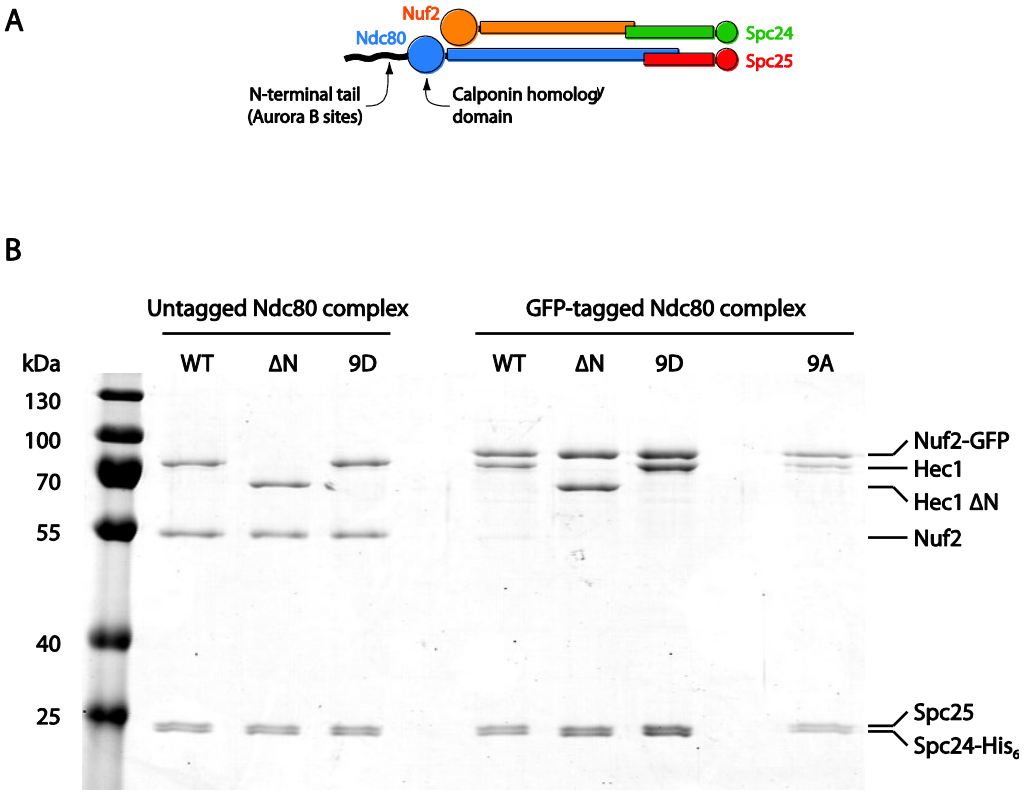

Figure 4.1: The human Ndc80 complex was expressed in and purified from *E. coli* using affinity and size-exclusion chromatography.
(A) Schematic of the heterotetrameric Ndc80 complex. (B) A Coomassie-stained gel shows the purified, recombinant wild-type and mutant versions of the Ndc80 complex used in this study. Molecular weight size markers are labeled on the left, and Ndc80 complex proteins, identified by size, are labeled on the right.

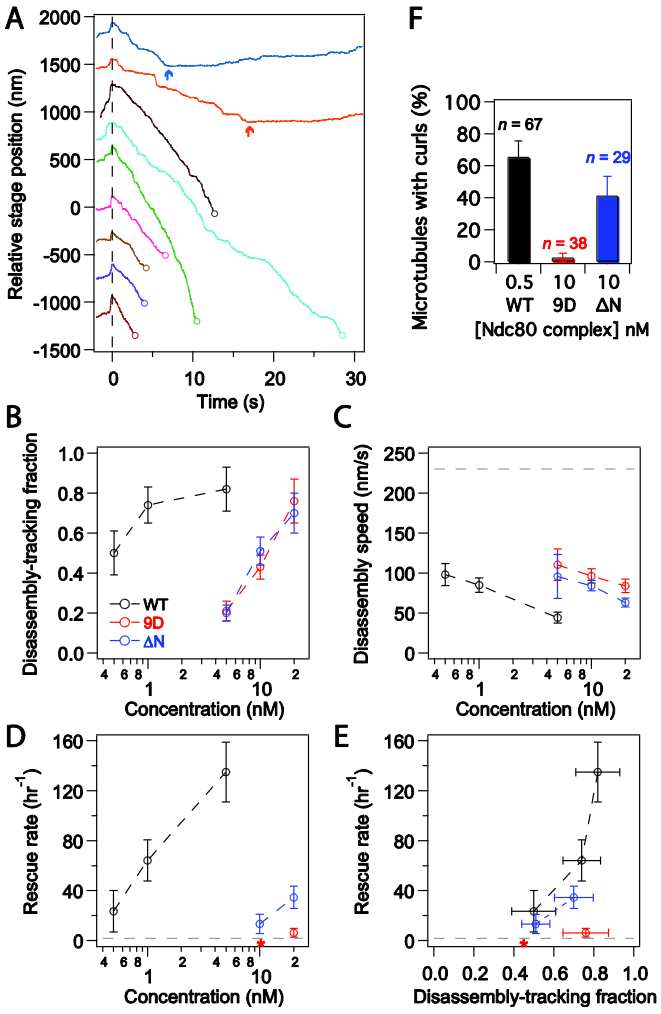

Figure 4.2: Phosphomimetic mutations in the Ndc80 complex inhibit its ability to promote microtubule rescue.
(A) Example traces of position versus time for beads decorated with Ndc80 complex as they tracked microtubule disassembly against ~2 pN of applied force. Time $t = 0$ s (dashed vertical line) marks the onset of tracking, when the disassembling microtubule tip began to drive movement of the bead against the force of the trap. Disassembly-driven movement ended when the bead detached (open circles) or when the microtubule rescued (arrows). Traces are offset vertically for visual clarity. (B) The fraction of beads coated with wild-type or mutant Ndc80 complex capable of tracking against ~2 pN. From the disassembly-tracking events in B, (C) mean microtubule disassembly speeds ± SEM and (D) rescue rates were measured. Without load and in the absence of bead-bound Ndc80 complex, the disassembly rate was 230 ± 14 nm/s (dashed line in C, $n = 26$) and the rescue rate was 2 ± 1 hr^{-1} (dashed line in D, $n = 3$ events in 104 minutes of disassembly). (E) Rescue rate is plotted against the fraction of beads that tracked disassembly against force. (F) Percentage of microtubules for which a curl (Appendix B, Figures 2D and S3B) was observed at either tip during disassembly in the TIRF microscopy assay. The n for each data point in B-D is listed in Table 4.1. Asterisks indicate that no rescues were observed. Unless otherwise noted, all error bars represent uncertainties from counting statistics.

Ndc80 complex	WT			9D			ΔN		
Concentration (nM)	0.5	1	5	5	10	20	5	10	20
n (disassembly-tracking fraction)	40	84	74	98	134	58	122	111	74
n (disassembly speed)	21	47	54	8	46	53	11	39	40
n (number of rescues)	2	15	32	ND	0	3	ND	3	15
Rescue rate observation time (minutes of disassembly)	5	14	14	ND	16	29	ND	13	26

ND, not determined.

Table 4.1: Number of replicates for optical trap assays.

Chapter 5.

Conclusions

Reconstitution uncovers the unique role of each kinetochore component

The recent purification of native kinetochore particles from budding yeast has enabled their biophysical characterization *in vitro*, and these studies have provided a set of performance benchmarks by which we can evaluate biochemically reconstituted kinetochore complexes (AKIYOSHI *et al.* 2010). Remarkably, reconstituted particles containing only the Ndc80 and Dam1 complexes recapitulate several key features of purified kinetochores. Both reconstituted and native kinetochore-based couplers form stable attachments to dynamic microtubule ends, sustain these attachments against high forces, and modify microtubule tip dynamics. However, native kinetochore particles exhibit these mechanical properties even at the level of a single coupler, while this has not yet been possible with a single reconstituted complex. This important distinction suggests that additional components must be added to the Ndc80 and Dam1 complexes in order to fully reconstitute the microtubule-binding activity of native kinetochores.

Purified kinetochore particles comprise many additional proteins beyond those in the Ndc80 and Dam1 complexes, and might contribute to the microtubule-binding interface in several ways. One possibility is that additional direct linkages to the microtubule end are required. For example, the Spc105 protein binds microtubules and is present in purified kinetochores (AKIYOSHI *et al.* 2010; CHEESEMAN *et al.* 2006; PAGLIUCA *et al.* 2009). Another possibility is that proteins in the structural core of the kinetochore indirectly affect the microtubule-binding interface (see next section). Finally, purified kinetochores contain additional proteins that influence microtubule dynamics. Their potential for indirectly

influencing kinetochore-microtubule attachments is well-supported by experimental data, as microtubule tip state is a strong determinant of attachment stability *in vitro*. Through systematic biochemical reconstitution *in vitro*, we can test these hypotheses and uncover how every component contributes to kinetochore function.

Kinetochore structural organization promotes avidity and optimal attachment geometry at the microtubule interface

Kinetochores are organized in a hierarchical manner, as the copy number of kinetochore components increases dramatically from the DNA-binding layer to the microtubule-binding layer. For example, kinetochores insert into DNA via two centromere-specific nucleosomes, while ~20 Ndc80 complexes and ~30 Dam1 complexes comprise the microtubule attachment site (LAWRIMORE *et al.* 2011). This multiplicity in copy number suggests that avidity – that is, many independent binding molecules combined as a single functional unit – is especially important for kinetochore-microtubule attachment, but not for kinetochore-DNA attachment. One possible explanation is that centromere DNA provides a stable attachment point, while microtubule ends are highly dynamic substrates.

The requirement of avidity for coupling to dynamic microtubule ends is supported by *in vitro* measurements. High copy numbers of Ndc80 and Dam1 complexes are needed for reconstituted couplers to approach the mechanical properties of a single native kinetochore particle. Furthermore, kinetochore-microtubule attachments are highly sensitive to microtubule dynamics *in vitro*. At any given force, detachment typically occurs ~10- to 100-fold more frequently from disassembling microtubule tips relative to assembling tips (AKIYOSHI *et al.* 2010; FRANCK *et al.* 2007; POWERS *et al.* 2009). Thus, the kinetochore must form many independent linkages to the microtubule end in order to hang on even as the polymer lattice

disintegrates from within its grasp. Furthermore, avidity promotes load sharing between individual microtubule-binding components. When acting in a parallel loading configuration, the force experienced by each individual component is inversely proportional to the total number of independent linkages. The lifetime of most protein-protein interactions decreases exponentially against increasing force (BELL 1978). Therefore, load sharing could dramatically increase the stability of kinetochore-microtubule attachments.

Kinetochore organization additionally promotes optimal microtubule attachment geometry. One way in which this occurs is through oligomerization of kinetochore components at the microtubule-binding interface. Components in the structural core of the kinetochore might contribute in similar ways. These components could enhance microtubule coupling indirectly by positioning the microtubule-binding complexes in an orientation more favorable for their interaction with the microtubule end, and/or more conducive to their cooperation as a unit.

The hierarchical assembly of kinetochores has important implications for the propagation of mechanical load from the microtubule end to the DNA. As force generated at the microtubule interface is transmitted through the kinetochore towards the DNA, the load will be divided among progressively fewer copies of components. As a result, the dynamic force range experienced by any single component is expected to be highest near the DNA-binding site. Intuitively, this would be an optimal location for any molecule that senses kinetochore tension and signals to mitotic error correction pathways. *In vitro* kinetochore reconstitution and biophysical interrogation will enable identification of which kinetochore components have evolved to withstand force. This will be a key step toward understanding how kinetochores sense and transmit mechanical forces in order to accurately segregate chromosomes during mitosis.

Mitotic regulation targets both sides of the kinetochore-microtubule interface

Tension likely serves as an indicator of chromosome alignment for mitotic error correction pathways. Incorrect attachment geometries, such as when both sister kinetochores attach to microtubules emanating from one spindle pole, typically generate low levels of tension relative to correct (bipolar) attachments. These aberrant kinetochore-microtubule attachments must be selectively destabilized for chromosome re-alignment. Corrective detachment is driven by the Aurora B kinase, which phosphorylates kinetochore substrates (including the Ndc80 and Dam1 complexes) and promotes their unbinding from microtubules. This destabilizing effect can be observed directly, even at the single-molecule level *in vitro*. One interesting possibility that has not yet been explored is whether Aurora B phosphorylation additionally alters the force sensitivity of kinetochore-microtubule attachments. Native kinetochore particles exhibit "catch bond-like" properties, as their attachments to microtubules are relatively weak under low forces and are actually stabilized by applying higher forces (AKIYOSHI *et al.* 2010). By modifying the force-dependence of attachment lifetime, Aurora B might further destabilize attachments that generate low tension. This would be a robust error correction mechanism as it can account for the high specificity with which aberrant kinetochore-microtubule attachments are targeted for turnover.

The microtubule tip is also a key point of regulation during error correction. Kinetochore-microtubule attachments are exquisitely sensitive to microtubule dynamics, as disassembly dramatically promotes detachment *in vitro*. This is likely due in large part to the dissociation of lattice segments to which the kinetochore is bound. Another key distinction between assembling and disassembling tips *in vitro* is their structure. Protofilaments at growing microtubule ends are typically straight or gently tapered, while those at shortening tips are tightly

curled (MANDELKOW *et al.* 1991; MULLER-REICHERT *et al.* 1998). Therefore, the shape of the microtubule end itself might influence kinetochore-microtubule coupling. *In vivo*, all kinetochore-microtubule ends appear gently tapered, consistent with the possibility that gently tapered ends are more suitable substrates for kinetochores (MCINTOSH *et al.* 2008). This observation further suggests that microtubule tip structure is regulated in cells. Kinetochores could influence microtubule tip shape directly, perhaps through the action of components that regulate microtubule dynamics. Other microtubule regulators are present on the mitotic spindle; the localization of many such proteins to kinetochore-microtubule tips is antagonized by Aurora B activity (KNOWLTON *et al.* 2006; ZIMNIAK *et al.* 2009). Thus, the mitotic error correction machinery employs a two-pronged approach, targeting both sides of the kinetochore-microtubule interface to drive corrective detachment. Understanding how these pathways are integrated throughout mitosis and in response to different types of erroneous attachments will be the subject of future work.

Bibliography

AKIYOSHI, B., C. R. NELSON, J. A. RANISH and S. BIGGINS, 2009 Analysis of Ipl1-mediated phosphorylation of the Ndc80 kinetochore protein in Saccharomyces cerevisiae. Genetics **183:** 1591-1595.

AKIYOSHI, B., K. K. SARANGAPANI, A. F. POWERS, C. R. NELSON, S. L. REICHOW *et al.*, 2010 Tension directly stabilizes reconstituted kinetochore-microtubule attachments. Nature **468:** 576-579.

ALUSHIN, G. M., V. H. RAMEY, S. PASQUALATO, D. A. BALL, N. GRIGORIEFF *et al.*, 2010 The Ndc80 kinetochore complex forms oligomeric arrays along microtubules. Nature **467:** 805-810.

ANDERSON, M., J. HAASE, E. YEH and K. BLOOM, 2009 Function and assembly of DNA looping, clustering, and microtubule attachment complexes within a eukaryotic kinetochore. Mol Biol Cell **20:** 4131-4139.

ASBURY, C. L., D. R. GESTAUT, A. F. POWERS, A. D. FRANCK and T. N. DAVIS, 2006 The Dam1 kinetochore complex harnesses microtubule dynamics to produce force and movement. Proc Natl Acad Sci U S A **103:** 9873-9878.

ASBURY, C. L., J. F. TIEN and T. N. DAVIS, 2011 Kinetochores' gripping feat: conformational wave or biased diffusion? Trends Cell Biol **21:** 38-46.

BELL, G. I., 1978 Models for the specific adhesion of cells to cells. Science **200:** 618-627.

BIGGINS, S., 2013 The composition, functions, and regulation of the budding yeast kinetochore. Genetics **194:** 817-846.

BIGGINS, S., and A. W. MURRAY, 2001 The budding yeast protein kinase Ipl1/Aurora allows the absence of tension to activate the spindle checkpoint. Genes Dev **15:** 3118-3129.

BIGGINS, S., F. F. SEVERIN, N. BHALLA, I. SASSOON, A. A. HYMAN *et al.*, 1999 The conserved protein kinase Ipl1 regulates microtubule binding to kinetochores in budding yeast. Genes Dev **13:** 532-544.

BURKE, D., D. DAWSON and T. STEARNS, 2000 *Methods in Yeast Genetics*. Cold Spring Harbor Laboratory Press, New York.

CHEESEMAN, I. M., S. ANDERSON, M. JWA, E. M. GREEN, J. KANG *et al.*, 2002 Phospho-regulation of kinetochore-microtubule attachments by the Aurora kinase Ipl1p. Cell **111:** 163-172.

CHEESEMAN, I. M., J. S. CHAPPIE, E. M. WILSON-KUBALEK and A. DESAI, 2006 The conserved KMN network constitutes the core microtubule-binding site of the kinetochore. Cell **127:** 983-997.

CIFERRI, C., S. PASQUALATO, E. SCREPANTI, G. VARETTI, S. SANTAGUIDA *et al.*, 2008 Implications for kinetochore-microtubule attachment from the structure of an engineered Ndc80 complex. Cell **133:** 427-439.

CIMINI, D., B. MOREE, J. C. CANMAN and E. D. SALMON, 2003 Merotelic kinetochore orientation occurs frequently during early mitosis in mammalian tissue cells and error correction is achieved by two different mechanisms. J Cell Sci **116:** 4213-4225.

CIMINI, D., X. WAN, C. B. HIREL and E. D. SALMON, 2006 Aurora kinase promotes turnover of kinetochore microtubules to reduce chromosome segregation errors. Curr Biol **16:** 1711-1718.

DE WULF, P., A. D. MCAINSH and P. K. SORGER, 2003 Hierarchical assembly of the budding yeast kinetochore from multiple subcomplexes. Genes Dev **17:** 2902-2921.
DELUCA, J. G., W. E. GALL, C. CIFERRI, D. CIMINI, A. MUSACCHIO *et al.*, 2006 Kinetochore microtubule dynamics and attachment stability are regulated by Hec1. Cell **127:** 969-982.
DELUCA, K. F., S. M. LENS and J. G. DELUCA, 2011 Temporal changes in Hec1 phosphorylation control kinetochore-microtubule attachment stability during mitosis. J Cell Sci **124:** 622-634.
EFREMOV, A., E. L. GRISHCHUK, J. R. MCINTOSH and F. I. ATAULLAKHANOV, 2007 In search of an optimal ring to couple microtubule depolymerization to processive chromosome motions. Proc Natl Acad Sci U S A **104:** 19017-19022.
EVANS, L., T. MITCHISON and M. KIRSCHNER, 1985 Influence of the centrosome on the structure of nucleated microtubules. J Cell Biol **100:** 1185-1191.
FOLEY, E. A., and T. M. KAPOOR, 2013 Microtubule attachment and spindle assembly checkpoint signalling at the kinetochore. Nat Rev Mol Cell Biol **14:** 25-37.
FRANCK, A. D., A. F. POWERS, D. R. GESTAUT, T. N. DAVIS and C. L. ASBURY, 2010 Direct physical study of kinetochore-microtubule interactions by reconstitution and interrogation with an optical force clamp. Methods **51:** 242-250.
FRANCK, A. D., A. F. POWERS, D. R. GESTAUT, T. GONEN, T. N. DAVIS *et al.*, 2007 Tension applied through the Dam1 complex promotes microtubule elongation providing a direct mechanism for length control in mitosis. Nat Cell Biol **9:** 832-837.
GAITANOS, T. N., A. SANTAMARIA, A. A. JEYAPRAKASH, B. WANG, E. CONTI *et al.*, 2009 Stable kinetochore-microtubule interactions depend on the Ska complex and its new component Ska3/C13Orf3. EMBO J **28:** 1442-1452.
GESTAUT, D. R., J. COOPER, C. L. ASBURY, T. N. DAVIS and L. WORDEMAN, 2010 Reconstitution and functional analysis of kinetochore subcomplexes. Methods Cell Biol **95:** 641-656.
GESTAUT, D. R., B. GRACZYK, J. COOPER, P. O. WIDLUND, A. ZELTER *et al.*, 2008 Phosphoregulation and depolymerization-driven movement of the Dam1 complex do not require ring formation. Nat Cell Biol **10:** 407-414.
GOTTESFELD, J. M., and D. J. FORBES, 1997 Mitotic repression of the transcriptional machinery. Trends Biochem Sci **22:** 197-202.
GRACZYK, B., and T. N. DAVIS, 2011 An assay to measure the affinity of proteins for microtubules by quantitative fluorescent microscopy. Anal Biochem **410:** 313-315.
GRISHCHUK, E. L., A. K. EFREMOV, V. A. VOLKOV, I. S. SPIRIDONOV, N. GUDIMCHUK *et al.*, 2008a The Dam1 ring binds microtubules strongly enough to be a processive as well as energy-efficient coupler for chromosome motion. Proc Natl Acad Sci U S A **105:** 15423-15428.
GRISHCHUK, E. L., I. S. SPIRIDONOV, V. A. VOLKOV, A. EFREMOV, S. WESTERMANN *et al.*, 2008b Different assemblies of the DAM1 complex follow shortening microtubules by distinct mechanisms. Proc Natl Acad Sci U S A **105:** 6918-6923.
GUIMARAES, G. J., Y. DONG, B. F. MCEWEN and J. G. DELUCA, 2008 Kinetochore-microtubule attachment relies on the disordered N-terminal tail domain of Hec1. Curr Biol **18:** 1778-1784.
HANISCH, A., H. H. SILLJE and E. A. NIGG, 2006 Timely anaphase onset requires a novel spindle and kinetochore complex comprising Ska1 and Ska2. EMBO J **25:** 5504-5515.

HAUF, S., R. W. COLE, S. LATERRA, C. ZIMMER, G. SCHNAPP *et al.*, 2003 The small molecule Hesperadin reveals a role for Aurora B in correcting kinetochore-microtubule attachment and in maintaining the spindle assembly checkpoint. J Cell Biol **161:** 281-294.

HILL, A., 1910 The possible effects of the aggregation of the molecules of haemoglobin on its dissociation curves. J. Physiol. **40:** iv-vii.

HUNTER, A. W., M. CAPLOW, D. L. COY, W. O. HANCOCK, S. DIEZ *et al.*, 2003 The kinesin-related protein MCAK is a microtubule depolymerase that forms an ATP-hydrolyzing complex at microtubule ends. Mol Cell **11:** 445-457.

INOUE, S., and E. D. SALMON, 1995 Force generation by microtubule assembly/disassembly in mitosis and related movements. Mol Biol Cell **6:** 1619-1640.

JANKE, C., J. ORTIZ, J. LECHNER, A. SHEVCHENKO, M. M. MAGIERA *et al.*, 2001 The budding yeast proteins Spc24p and Spc25p interact with Ndc80p and Nuf2p at the kinetochore and are important for kinetochore clustering and checkpoint control. EMBO J **20:** 777-791.

JANKE, C., J. ORTIZ, T. U. TANAKA, J. LECHNER and E. SCHIEBEL, 2002 Four new subunits of the Dam1-Duo1 complex reveal novel functions in sister kinetochore biorientation. EMBO J **21:** 181-193.

JIANG, K., J. WANG, J. LIU, T. WARD, L. WORDEMAN *et al.*, 2009 TIP150 interacts with and targets MCAK at the microtubule plus ends. EMBO Rep **10:** 857-865.

JOGLEKAR, A. P., K. BLOOM and E. D. SALMON, 2009 In vivo protein architecture of the eukaryotic kinetochore with nanometer scale accuracy. Curr Biol **19:** 694-699.

JOHNSON, K. A., and G. G. BORISY, 1977 Kinetic analysis of microtubule self-assembly in vitro. J Mol Biol **117:** 1-31.

KASTENMAYER, J. P., L. NI, A. CHU, L. E. KITCHEN, W. C. AU *et al.*, 2006 Functional genomics of genes with small open reading frames (sORFs) in S. cerevisiae. Genome Res **16:** 365-373.

KEATING, P., N. RACHIDI, T. U. TANAKA and M. J. STARK, 2009 Ipl1-dependent phosphorylation of Dam1 is reduced by tension applied on kinetochores. J Cell Sci **122:** 4375-4382.

KELLY, A. E., and H. FUNABIKI, 2009 Correcting aberrant kinetochore microtubule attachments: an Aurora B-centric view. Curr Opin Cell Biol **21:** 51-58.

KELMAN, Z., 1997 PCNA: structure, functions and interactions. Oncogene **14:** 629-640.

KING, J. M., T. S. HAYS and R. B. NICKLAS, 2000 Dynein is a transient kinetochore component whose binding is regulated by microtubule attachment, not tension. J Cell Biol **151:** 739-748.

KLINE-SMITH, S. L., S. SANDALL and A. DESAI, 2005 Kinetochore-spindle microtubule interactions during mitosis. Curr Opin Cell Biol **17:** 35-46.

KNOWLTON, A. L., W. LAN and P. T. STUKENBERG, 2006 Aurora B is enriched at merotelic attachment sites, where it regulates MCAK. Curr Biol **16:** 1705-1710.

KOSHLAND, D. E., T. J. MITCHISON and M. W. KIRSCHNER, 1988 Polewards chromosome movement driven by microtubule depolymerization in vitro. Nature **331:** 499-504.

LAMPERT, F., P. HORNUNG and S. WESTERMANN, 2010 The Dam1 complex confers microtubule plus end-tracking activity to the Ndc80 kinetochore complex. J Cell Biol **189:** 641-649.

LAMPSON, M. A., and I. M. CHEESEMAN, 2011 Sensing centromere tension: Aurora B and the regulation of kinetochore function. Trends Cell Biol **21:** 133-140.

LAMPSON, M. A., K. RENDUCHITALA, A. KHODJAKOV and T. M. KAPOOR, 2004 Correcting improper chromosome-spindle attachments during cell division. Nat Cell Biol **6:** 232-237.

LANCASTER, O. M., and B. BAUM, 2014 Shaping up to divide: Coordinating actin and microtubule cytoskeletal remodelling during mitosis. Semin Cell Dev Biol.

LAWRIMORE, J., K. S. BLOOM and E. D. SALMON, 2011 Point centromeres contain more than a single centromere-specific Cse4 (CENP-A) nucleosome. J Cell Biol **195:** 573-582.

LEDBETTER, M. C., and K. R. PORTER, 1963 A "Microtubule" in Plant Cell Fine Structure. J Cell Biol **19:** 239-250.

LI, J. M., Y. LI and S. J. ELLEDGE, 2005 Genetic analysis of the kinetochore DASH complex reveals an antagonistic relationship with the ras/protein kinase A pathway and a novel subunit required for Ask1 association. Mol Cell Biol **25:** 767-778.

LIU, D., G. VADER, M. J. VROMANS, M. A. LAMPSON and S. M. LENS, 2009 Sensing chromosome bi-orientation by spatial separation of aurora B kinase from kinetochore substrates. Science **323:** 1350-1353.

LONGTINE, M. S., A. MCKENZIE, 3RD, D. J. DEMARINI, N. G. SHAH, A. WACH *et al.*, 1998 Additional modules for versatile and economical PCR-based gene deletion and modification in Saccharomyces cerevisiae. Yeast **14:** 953-961.

MADDOX, P., A. STRAIGHT, P. COUGHLIN, T. J. MITCHISON and E. D. SALMON, 2003 Direct observation of microtubule dynamics at kinetochores in Xenopus extract spindles: implications for spindle mechanics. J Cell Biol **162:** 377-382.

MAIDA, I., E. BOSI, E. PERRIN, M. C. PAPALEO, V. ORLANDINI *et al.*, 2013 Draft Genome Sequence of the Fast-Growing Bacterium Vibrio natriegens Strain DSMZ 759. Genome Announc **1**.

MANDELKOW, E. M., E. MANDELKOW and R. A. MILLIGAN, 1991 Microtubule dynamics and microtubule caps: a time-resolved cryo-electron microscopy study. J Cell Biol **114:** 977-991.

MANNA, T., S. HONNAPPA, M. O. STEINMETZ and L. WILSON, 2008 Suppression of microtubule dynamic instability by the +TIP protein EB1 and its modulation by the CAP-Gly domain of p150glued. Biochemistry **47:** 779-786.

MCGHEE, J. D., and P. H. VON HIPPEL, 1974 Theoretical aspects of DNA-protein interactions: co-operative and non-co-operative binding of large ligands to a one-dimensional homogeneous lattice. J Mol Biol **86:** 469-489.

MCINTOSH, J. R., E. L. GRISHCHUK, M. K. MORPHEW, A. K. EFREMOV, K. ZHUDENKOV *et al.*, 2008 Fibrils connect microtubule tips with kinetochores: a mechanism to couple tubulin dynamics to chromosome motion. Cell **135:** 322-333.

MILLER, M. P., E. UNAL, G. A. BRAR and A. AMON, 2012 Meiosis I chromosome segregation is established through regulation of microtubule-kinetochore interactions. Elife **1:** e00117.

MILLER, S. A., M. L. JOHNSON and P. T. STUKENBERG, 2008 Kinetochore attachments require an interaction between unstructured tails on microtubules and Ndc80(Hec1). Curr Biol **18:** 1785-1791.

MIRANDA, J. J., P. DE WULF, P. K. SORGER and S. C. HARRISON, 2005 The yeast DASH complex forms closed rings on microtubules. Nat Struct Mol Biol **12:** 138-143.

MIRANDA, J. J., D. S. KING and S. C. HARRISON, 2007 Protein Arms in the Kinetochore-Microtubule Interface of the Yeast DASH Complex. Mol Biol Cell.

MITCHISON, T., and M. KIRSCHNER, 1984 Dynamic instability of microtubule growth. Nature **312:** 237-242.

MOLODTSOV, M. I., E. L. GRISHCHUK, A. K. EFREMOV, J. R. MCINTOSH and F. I. ATAULLAKHANOV, 2005 Force production by depolymerizing microtubules: a theoretical study. Proc Natl Acad Sci U S A **102:** 4353-4358.

MULLER-REICHERT, T., D. CHRETIEN, F. SEVERIN and A. A. HYMAN, 1998 Structural changes at microtubule ends accompanying GTP hydrolysis: information from a slowly hydrolyzable analogue of GTP, guanylyl (alpha,beta)methylenediphosphonate. Proc Natl Acad Sci U S A **95:** 3661-3666.

MULLER, E. G. D., B. E. SNYDSMAN, I. NOVIK, D. W. HAILEY, D. R. GESTAUT *et al.*, 2005 The organization of the core proteins of the yeast spindle pole body. Mol Biol Cell **16:** 3341-3352.

NICKLAS, R. B., 1988 The forces that move chromosomes in mitosis. Annu Rev Biophys Biophys Chem **17:** 431-449.

NISHIMURA, K., T. FUKAGAWA, H. TAKISAWA, T. KAKIMOTO and M. KANEMAKI, 2009 An auxin-based degron system for the rapid depletion of proteins in nonplant cells. Nat Methods **6:** 917-922.

ORGEL, L. E., 1998 The origin of life--a review of facts and speculations. Trends Biochem Sci **23:** 491-495.

PAGLIUCA, C., V. M. DRAVIAM, E. MARCO, P. K. SORGER and P. DE WULF, 2009 Roles for the conserved spc105p/kre28p complex in kinetochore-microtubule binding and the spindle assembly checkpoint. PLoS One **4:** e7640.

PAGLIUCA, F. W., M. O. COLLINS, A. LICHAWSKA, P. ZEGERMAN, J. S. CHOUDHARY *et al.*, 2011 Quantitative proteomics reveals the basis for the biochemical specificity of the cell-cycle machinery. Mol Cell **43:** 406-417.

PEARSON, C. G., P. S. MADDOX, E. D. SALMON and K. BLOOM, 2001 Budding yeast chromosome structure and dynamics during mitosis. J Cell Biol **152:** 1255-1266.

PINSKY, B. A., C. KUNG, K. M. SHOKAT and S. BIGGINS, 2006 The Ipl1-Aurora protein kinase activates the spindle checkpoint by creating unattached kinetochores. Nat Cell Biol **8:** 78-83.

POWERS, A. F., A. D. FRANCK, D. R. GESTAUT, J. COOPER, B. GRACYZK *et al.*, 2009 The Ndc80 kinetochore complex forms load-bearing attachments to dynamic microtubule tips via biased diffusion. Cell **136:** 865-875.

RAAIJMAKERS, J. A., M. E. TANENBAUM, A. F. MAIA and R. H. MEDEMA, 2009 RAMA1 is a novel kinetochore protein involved in kinetochore-microtubule attachment. J Cell Sci **122:** 2436-2445.

RICE, L. M., E. A. MONTABANA and D. A. AGARD, 2008 The lattice as allosteric effector: structural studies of alphabeta- and gamma-tubulin clarify the role of GTP in microtubule assembly. Proc Natl Acad Sci U S A **105:** 5378-5383.

RICE, S., A. W. LIN, D. SAFER, C. L. HART, N. NABER *et al.*, 1999 A structural change in the kinesin motor protein that drives motility. Nature **402:** 778-784.

RIEDER, C. L., 1982 The formation, structure, and composition of the mammalian kinetochore and kinetochore fiber. Int Rev Cytol **79:** 1-58.

SARANGAPANI, K. K., B. AKIYOSHI, N. M. DUGGAN, S. BIGGINS and C. L. ASBURY, 2013 Phosphoregulation promotes release of kinetochores from dynamic microtubules via multiple mechanisms. Proc Natl Acad Sci U S A **110:** 7282-7287.

SHANG, C., T. R. HAZBUN, I. M. CHEESEMAN, J. ARANDA, S. FIELDS *et al.*, 2003 Kinetochore protein interactions and their regulation by the Aurora kinase Ipl1p. Mol Biol Cell **14:** 3342-3355.

SHIMOGAWA, M. M., B. GRACZYK, M. K. GARDNER, S. E. FRANCIS, E. A. WHITE *et al.*, 2006 Mps1 phosphorylation of Dam1 couples kinetochores to microtubule plus ends at metaphase. Curr Biol **16:** 1489-1501.

SHIMOGAWA, M. M., M. M. WARGACKI, E. G. MULLER and T. N. DAVIS, 2010 Laterally attached kinetochores recruit the checkpoint protein Bub1, but satisfy the spindle checkpoint. Cell Cycle **9:** 3619-3628.

SIEGEL, L. M., and K. J. MONTY, 1966 Determination of molecular weights and frictional ratios of proteins in impure systems by use of gel filtration and density gradient centrifugation. Application to crude preparations of sulfite and hydroxylamine reductases. Biochim Biophys Acta **112:** 346-362.

SKIBBENS, R. V., C. L. RIEDER and E. D. SALMON, 1995 Kinetochore motility after severing between sister centromeres using laser microsurgery: evidence that kinetochore directional instability and position is regulated by tension. J Cell Sci **108 (Pt 7):** 2537-2548.

SKIBBENS, R. V., V. P. SKEEN and E. D. SALMON, 1993 Directional instability of kinetochore motility during chromosome congression and segregation in mitotic newt lung cells: a push-pull mechanism. J Cell Biol **122:** 859-875.

SOLTYS, B. J., and G. G. BORISY, 1985 Polymerization of tubulin in vivo: direct evidence for assembly onto microtubule ends and from centrosomes. J Cell Biol **100:** 1682-1689.

STRAIGHT, A. F., W. F. MARSHALL, J. W. SEDAT and A. W. MURRAY, 1997 Mitosis in living budding yeast: anaphase A but no metaphase plate. Science **277:** 574-578.

SUNDIN, L. J., G. J. GUIMARAES and J. G. DELUCA, 2011 The NDC80 complex proteins Nuf2 and Hec1 make distinct contributions to kinetochore-microtubule attachment in mitosis. Molecular Biology of the Cell **22:** 759-768.

TANAKA, K., N. MUKAE, H. DEWAR, M. VAN BREUGEL, E. K. JAMES *et al.*, 2005 Molecular mechanisms of kinetochore capture by spindle microtubules. Nature **434:** 987-994.

TANAKA, T. U., and A. DESAI, 2008 Kinetochore-microtubule interactions: the means to the end. Curr Opin Cell Biol **20:** 53-63.

TANAKA, T. U., N. RACHIDI, C. JANKE, G. PEREIRA, M. GALOVA *et al.*, 2002 Evidence that the Ipl1-Sli15 (Aurora kinase-INCENP) complex promotes chromosome bi-orientation by altering kinetochore-spindle pole connections. Cell **108:** 317-329.

TIEN, J. F., N. T. UMBREIT, D. R. GESTAUT, A. D. FRANCK, J. COOPER *et al.*, 2010 Cooperation of the Dam1 and Ndc80 kinetochore complexes enhances microtubule coupling and is regulated by aurora B. J Cell Biol **189:** 713-723.

TIRNAUER, J. S., J. C. CANMAN, E. D. SALMON and T. J. MITCHISON, 2002 EB1 targets to kinetochores with attached, polymerizing microtubules. Mol Biol Cell **13:** 4308-4316.

TOOLEY, J. G., S. A. MILLER and P. T. STUKENBERG, 2011 The Ndc80 complex uses a tripartite attachment point to couple microtubule depolymerization to chromosome movement. Mol Biol Cell **22:** 1217-1226.

UMBREIT, N. T., D. R. GESTAUT, J. F. TIEN, B. S. VOLLMAR, T. GONEN *et al.*, 2012 The Ndc80 kinetochore complex directly modulates microtubule dynamics. Proc Natl Acad Sci U S A **109:** 16113-16118.

VAGNARELLI, P., 2012 Mitotic chromosome condensation in vertebrates. Exp Cell Res **318:** 1435-1441.

WACH, A., A. BRACHAT, C. ALBERTI-SEGUI, C. REBISCHUNG and P. PHILIPPSEN, 1997 Heterologous HIS3 marker and GFP reporter modules for PCR-targeting in Saccharomyces cerevisiae. Yeast **13:** 1065-1075.

WALKER, R. A., E. T. O'BRIEN, N. K. PRYER, M. F. SOBOEIRO, W. A. VOTER *et al.*, 1988 Dynamic instability of individual microtubules analyzed by video light microscopy: Rate constants and transition frequencies. J Cell Biol **107:** 1437-1448.

WAN, X., R. P. O'QUINN, H. L. PIERCE, A. P. JOGLEKAR, W. E. GALL *et al.*, 2009 Protein architecture of the human kinetochore microtubule attachment site. Cell **137:** 672-684.

WANG, H. W., V. H. RAMEY, S. WESTERMANN, A. E. LESCHZINER, J. P. WELBURN *et al.*, 2007 Architecture of the Dam1 kinetochore ring complex and implications for microtubule-driven assembly and force-coupling mechanisms. Nat Struct Mol Biol.

WARGACKI, M. M., J. C. TAY, E. G. MULLER, C. L. ASBURY and T. N. DAVIS, 2010 Kip3, the yeast kinesin-8, is required for clustering of kinetochores at metaphase. Cell Cycle **9:** 2581-2588.

WEI, R. R., J. AL-BASSAM and S. C. HARRISON, 2007 The Ndc80/HEC1 complex is a contact point for kinetochore-microtubule attachment. Nat Struct Mol Biol **14:** 54-59.

WEI, R. R., J. R. SCHNELL, N. A. LARSEN, P. K. SORGER, J. J. CHOU *et al.*, 2006 Structure of a central component of the yeast kinetochore: the Spc24p/Spc25p globular domain. Structure **14:** 1003-1009.

WEI, R. R., P. K. SORGER and S. C. HARRISON, 2005 Molecular organization of the Ndc80 complex, an essential kinetochore component. Proc Natl Acad Sci U S A **102:** 5363-5367.

WELBURN, J. P., E. L. GRISHCHUK, C. B. BACKER, E. M. WILSON-KUBALEK, J. R. YATES, 3RD *et al.*, 2009 The human kinetochore Ska1 complex facilitates microtubule depolymerization-coupled motility. Dev Cell **16:** 374-385.

WESTERMANN, S., A. AVILA-SAKAR, H. W. WANG, H. NIEDERSTRASSER, J. WONG *et al.*, 2005 Formation of a dynamic kinetochore- microtubule interface through assembly of the Dam1 ring complex. Mol Cell **17:** 277-290.

WESTERMANN, S., D. G. DRUBIN and G. BARNES, 2007 Structures and functions of yeast kinetochore complexes. Annu Rev Biochem **76:** 563-591.

WESTERMANN, S., H. W. WANG, A. AVILA-SAKAR, D. G. DRUBIN, E. NOGALES *et al.*, 2006 The Dam1 kinetochore ring complex moves processively on depolymerizing microtubule ends. Nature **440:** 565-569.

WILSON-KUBALEK, E. M., I. M. CHEESEMAN, C. YOSHIOKA, A. DESAI and R. A. MILLIGAN, 2008 Orientation and structure of the Ndc80 complex on the microtubule lattice. J Cell Biol **182:** 1055-1061.

ZHANG, J., S. AHMAD and Y. MAO, 2007 BubR1 and APC/EB1 cooperate to maintain metaphase chromosome alignment. J Cell Biol **178:** 773-784.

ZIMNIAK, T., K. STENGL, K. MECHTLER and S. WESTERMANN, 2009 Phosphoregulation of the budding yeast EB1 homologue Bim1p by Aurora/Ipl1p. J Cell Biol **186:** 379-391.

Appendix A

Cooperation of the Dam1 and Ndc80 kinetochore complexes enhances microtubule coupling and is regulated by aurora B

Tien, J. F., N. T. Umbreit, D. R. Gestaut, A. D. Franck, J. Cooper, L. Wordeman, T. Gonen, C.L. Asubry, and T.N. Davis.

The Journal of Cell Biology (2010) 189: 713-723.

Published May 17, 2010

Cooperation of the Dam1 and Ndc80 kinetochore complexes enhances microtubule coupling and is regulated by aurora B

Jerry F. Tien,[1] Neil T. Umbreit,[1] Daniel R. Gestaut,[1] Andrew D. Franck,[2] Jeremy Cooper,[2] Linda Wordeman,[2] Tamir Gonen,[1,3] Charles L. Asbury,[2] and Trisha N. Davis[1]

[1]Department of Biochemistry, [2]Department of Physiology and Biophysics, and [3]Howard Hughes Medical Institute, University of Washington, Seattle, WA 98195

The coupling of kinetochores to dynamic spindle microtubules is crucial for chromosome positioning and segregation, error correction, and cell cycle progression. How these fundamental attachments are made and persist under tensile forces from the spindle remain important questions. As microtubule-binding elements, the budding yeast Ndc80 and Dam1 kinetochore complexes are essential and not redundant, but their distinct contributions are unknown. In this study, we show that the Dam1 complex is a processivity factor for the Ndc80 complex, enhancing the ability of the Ndc80 complex to form load-bearing attachments to and track with dynamic microtubule tips in vitro. Moreover, the interaction between the Ndc80 and Dam1 complexes is abolished when the Dam1 complex is phosphorylated by the yeast aurora B kinase Ipl1. This provides evidence for a mechanism by which aurora B resets aberrant kinetochore–microtubule attachments. We propose that the action of the Dam1 complex as a processivity factor in kinetochore–microtubule attachment is regulated by conserved signals for error correction.

Introduction

During mitosis, kinetochores attach to assembling and disassembling microtubule tips while withstanding tensile forces from the mitotic spindle (Skibbens et al., 1993, 1995; Maddox et al., 2003). Kinetochores are able to harness energy from these disassembling microtubule tips to drive movement of chromosomes (for a review see Inoué and Salmon, 1995). Understanding how the kinetochore establishes microtubule attachments under force requires understanding the organization of the kinetochore components and how they bear and transmit load. Recent studies investigated the spatial organization of kinetochore components in vivo and how their arrangement changes throughout mitosis (Joglekar et al., 2009; Wan et al., 2009). Through systematic reconstitution of kinetochore components, we are pursuing a complementary approach with the ultimate goal of mapping the transmission of force across the kinetochore from the dynamic microtubule to the centromere. In this study, we focus on the kinetochore–microtubule interface.

The kinetochores of all eukaryotes contain multiple microtubule-binding elements. The KMN network (KNL-1, Mis12 complex, and Ndc80 complex) and the Ska1 complex both bind microtubules in higher eukaryotic cells (Cheeseman et al., 2006; Gaitanos et al., 2009; Welburn et al., 2009). Yeast also contain the KMN network and the Dam1 complex, possibly the functional homologue of the Ska1 complex (Hanisch et al., 2006; Gaitanos et al., 2009; Raaijmakers et al., 2009; Welburn et al., 2009). Cooperation of the three components of the conserved KMN network was shown by cosedimentation with taxol-stabilized microtubules (Cheeseman et al., 2006), but how or whether any of the microtubule-binding components cooperate to achieve attachment to dynamic microtubules is unknown. We show for the first time that cooperation between two

J.F. Tien, N.T. Umbreit, D.R. Gestaut, and A.D. Franck contributed equally to this paper.

Correspondence to Trisha N. Davis: tdavis@u.washington.edu

Abbreviations used in this paper: GB, growth buffer; TEV, tobacco etch virus; TIRF, total internal reflection fluorescence.

Supplemental Material can be found at:
http://jcb.rupress.org/content/suppl/2010/05/17/jcb.200910142.DC1.html

The Rockefeller University Press $30.00
J. Cell Biol. Vol. 189 No. 4 713–723
www.jcb.org/cgi/doi/10.1083/jcb.200910142

Published May 17, 2010

kinetochore subcomplexes enhances processive, load-bearing coupling to dynamic microtubule tips.

In the budding yeast kinetochore, all four proteins of the Ndc80 complex and all 10 proteins of the Dam1 complex are essential (Tanaka and Desai, 2008). In vitro, both complexes independently form diffusive attachments to the microtubule lattice and track with disassembling microtubule tips, although the Ndc80 complex requires artificial oligomerization to tip track (Westermann et al., 2006; Gestaut et al., 2008; Powers et al., 2009). The Dam1 complex also tracks robustly with polymerizing microtubules in vitro (Asbury et al., 2006; see Lampert et al. in this issue). When attached to beads, each complex forms load-bearing attachments to dynamic microtubule tips (Asbury et al., 2006; Franck et al., 2007; Grishchuk et al., 2008a,b; Powers et al., 2009). Despite these similarities, the Ndc80 and Dam1 complexes are not redundant. The Ndc80 complex is required in vivo for attachment to microtubules (Kline-Smith et al., 2005), and the Dam1 complex is required for attaching to the tips of microtubules and for establishing biorientation (Tanaka et al., 2005; Shimogawa et al., 2006). Moreover, the Ndc80 complex is required for the assembly of Dam1 complex onto the kinetochore (Janke et al., 2002), and an interaction between the two complexes has been suggested by localization and two-hybrid studies (Shang et al., 2003; Joglekar et al., 2009). Studying the combination of Ndc80 and Dam1 complexes in vitro will allow us to dissect their distinct roles in kinetochore–microtubule binding.

Kinetochores not only serve as physical bridges between chromosomes and spindle microtubules but are also regulatory hubs that ensure chromosome segregation fidelity during mitosis. For example, aurora B kinase is responsible for resetting aberrant kinetochore–microtubule attachments to achieve biorientation (Cheeseman et al., 2002; Tanaka et al., 2002; Hauf et al., 2003; Pinsky et al., 2006). Many of the microtubule-binding components of the kinetochore, including the Ndc80 and Dam1 complexes, are targets of aurora B (Cheeseman et al., 2002, 2006; Shang et al., 2003; DeLuca et al., 2006; Pinsky et al., 2006; Gestaut et al., 2008). In mammalian cells, aurora B phosphorylation of the N-terminal tail of the Ndc80 protein (Hec1 in humans) abolishes kinetochore–microtubule attachment (DeLuca et al., 2006; Guimaraes et al., 2008). Although the budding yeast Ndc80 protein also has an N-terminal tail, it is not essential (Akiyoshi et al., 2009; Kemmler et al., 2009). Previously, we demonstrated that phosphorylation by the yeast aurora B homologue Ipl1 at one target site within the Dam1 complex, Ser20 of Dam1, reduces its affinity for the microtubule lattice (Gestaut et al., 2008). Two-hybrid assays and pull-downs with in vitro–translated proteins using phosphomimetic mutations at Ipl1 target sites in Dam1 also suggested that phosphorylation of the Dam1 complex modulates its interaction with the Ndc80 complex (Shang et al., 2003). Moreover, Ipl1 target sites on Dam1 are dephosphorylated as cells enter metaphase in a cohesin-dependent manner, which could prevent kinetochore–microtubule attachment turnover as biorientation is established (Keating et al., 2009).

In this study, we show that the Dam1 complex is a phospho-regulated processivity factor for the Ndc80 complex in kinetochore–microtubule coupling. Using techniques for tracking and manipulating single molecules in vitro, we demonstrate directly an interaction between the Ndc80 and Dam1 complexes on microtubules. Through this interaction, the Dam1 complex enhances the ability of the Ndc80 complex to maintain attachment to dynamic microtubule tips even in the presence of external load. Finally, this interaction is regulated by Ipl1, further defining the mechanism for aurora B–mediated corrective detachment in vivo.

Results

The Dam1 and Ndc80 complexes interact on microtubules

We expressed recombinant Saccharomyces cerevisiae Ndc80 and Dam1 complexes in Escherichia coli and purified each complex by affinity chromatography and gel filtration (Wei et al., 2005; Gestaut et al., 2008; Powers et al., 2009). By velocity sedimentation analysis, we found weak interaction between the Ndc80 and Dam1 complexes free in solution (Fig. S1). Using total internal reflection fluorescence (TIRF) microscopy, we quantified the interaction of GFP-tagged Ndc80 complexes with microtubules in the presence and absence of Dam1 complex (Fig. 1). In the absence of Dam1 complex, individual Ndc80 complexes formed transient and diffusive attachments to microtubules, as reported previously (Powers et al., 2009). We measured a dissociation rate constant (k_{off}) of 0.44 ± 0.03 s^{-1}, an association rate constant (k_{on}) of 0.60 ± 0.02 $\mu M^{-1} \times s^{-1}$, and a diffusion constant of 0.067 ± 0.003 $\mu m^2 \times s^{-1}$ (Fig. 1, C–E), which are values comparable with our previous study (Powers et al., 2009). We also simultaneously visualized GFP-tagged Ndc80 complexes and mCherry-tagged Dam1 complexes on microtubules. At concentrations affording single molecule resolution of each complex, interaction events were rare. When the two complexes did associate with each other, they appeared to diffuse more slowly (Fig. S2). However, interaction events between individual Ndc80 and Dam1 complexes were too infrequent to affect population behavior. To increase the frequency of interactions, we raised the concentration of Dam1 complex while maintaining low concentrations (10 pM) of the Ndc80 complex. Overall, Ndc80 complex transitioned gradually to a more persistent and more slowly diffusing behavior as the concentration of Dam1 complex was increased (Fig. 1, C–E). At 500 pM Dam1 complex, the Ndc80 complex dissociated two-fold more slowly from the microtubule (k_{off} = 0.23 ± 0.02 s^{-1}) and associated 1.6-fold faster onto the microtubule (k_{on} = 0.99 ± 0.02 $\mu M^{-1} \times s^{-1}$) as compared with the Ndc80 complex alone. This corresponds to a threefold decrease in the apparent equilibrium dissociation constant, $K_d = k_{off} \times k_{on}^{-1}$ (0.74 ± 0.06 to 0.23 ± 0.02 µM). At 500 pM Dam1 complex, the Ndc80 complex also diffused fivefold more slowly (0.013 ± 0.0006 $\mu m^2 \times s^{-1}$) as compared with Ndc80 complex alone. The Dam1 complex was unlikely to be acting as a simple barrier to diffusional motility, as the diffusive behavior of the Ndc80 complex was unchanged in the presence of phosphorylated Dam1 complex at the same lattice density (see Ipl1 phosphorylation regulates...). The brightness distribution of the GFP signal remained unchanged

Published May 17, 2010

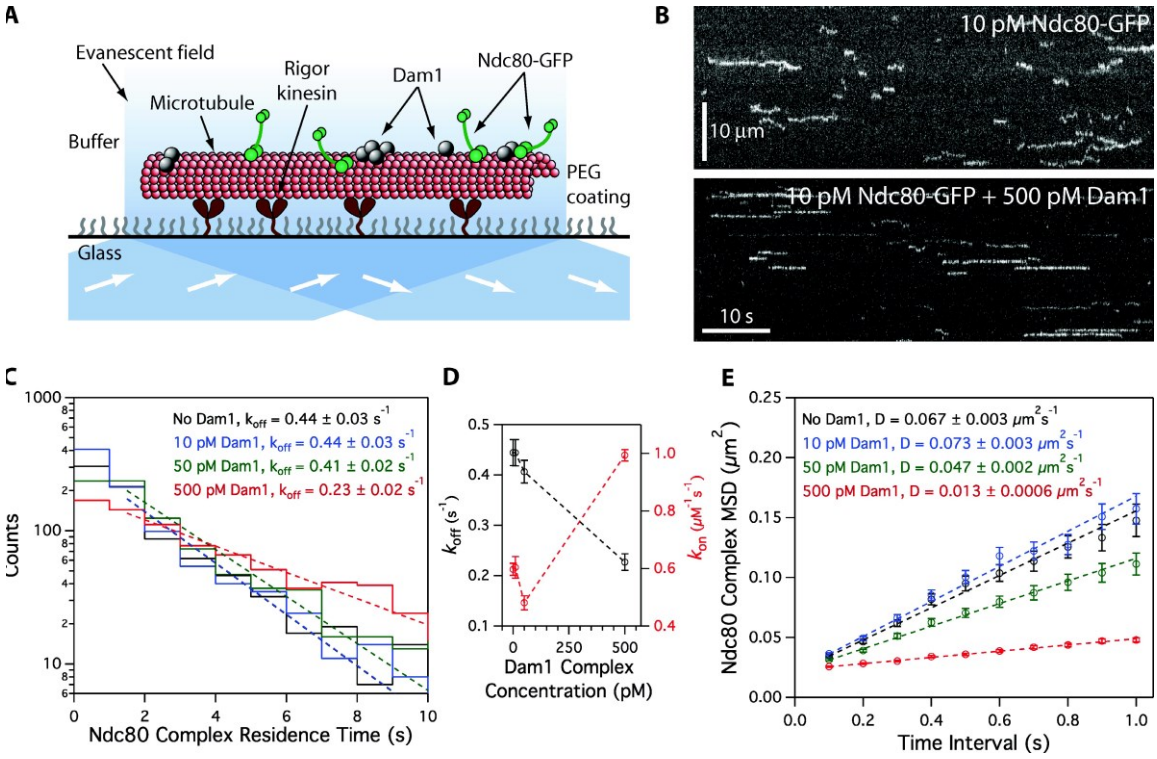

Figure 1. Dam1 complex enhances binding of individual Ndc80 complexes to microtubules. (A) Schematic of the TIRF assay developed to visualize the behavior of GFP-tagged Ndc80 complexes (green rods) in the presence of untagged Dam1 complexes (gray spheres) on microtubules. (B) Representative kymographs showing the binding and one-dimensional diffusion of 10 pM Ndc80 complexes on taxol-stabilized microtubules in the absence or presence of 500 pM Dam1 complex. Positions along the microtubule are shown on the vertical axis, whereas the passage of time is depicted along the horizontal axis. Concentrations are of free complexes in solution. (C) Residence time distributions of 10 pM Ndc80 complex on microtubules without Dam1 complex (black histogram; n = 883 events), with 10 pM Dam1 complex (blue histogram; n = 966), 50 pM Dam1 complex (green histogram; n = 928), and 500 pM Dam1 complex (red histogram; n = 1,003). Dotted lines show the weighted exponential fits used to determine dissociation rate constants, k_{off}. (D) Dissociation rate constants (k_{off}; left axis, black markers) for the Ndc80 complex, calculated from the data in C, are plotted against the concentration of Dam1 complex. Association rate constants (k_{on}; right axis, red markers) of the Ndc80 complex are also plotted (without Dam1 complex, n = 1,103; with 10 pM Dam1 complex, n = 1,426; with 50 pM Dam1 complex, n = 1,179; with 500 pM Dam1 complex, n = 1,412). (E) Mean-squared displacement (MSD) is plotted against time for 10 pM Ndc80 complex on microtubules without Dam1 complex (black markers; n = 803 events), with 10 pM Dam1 complex (blue markers; n = 859), 50 pM Dam1 complex (green markers; n = 883), and 500 pM Dam1 complex (red markers; n = 968). Dotted lines show the weighted linear fits used to determine diffusion constants, D. Markers indicate SEM.

across concentrations of the Dam1 complex, demonstrating that oligomerization of the Ndc80 complex did not contribute to its modified behavior in the presence of the Dam1 complex (Fig. 2). Even at 500 pM Dam1 complex, not all Ndc80 complexes bound persistently and diffused slowly. This indicates that not all Ndc80 complexes were associated with Dam1 complexes, so our calculated values describe a mixed population and likely underestimate Dam1 complex–mediated enhancement of Ndc80 complex–microtubule interactions.

In the presence of the Dam1 complex, diffusion of the Ndc80 complex is slowed far below the reported rate for a single Dam1 complex (Gestaut et al., 2008). Therefore, we hypothesized that at the concentrations required to observe significant changes in the population behavior of the Ndc80 complex, the Dam1 complex forms slowly diffusing oligomers. To test this, we measured the diffusion rate of GFP-tagged Dam1 complex on microtubules (Fig. S3, A and B). At 2 pM, single GFP-tagged Dam1 complexes diffused rapidly, at 0.060 ± 0.003 $\mu m^2 \times s^{-1}$, which is similar to the rates reported previously (Westermann et al., 2006; Gestaut et al., 2008). However, at 20 and 50 pM Dam1 complex, we observed slowly diffusing spots that exhibited fluorescence brighter than individual Dam1 complexes. To maintain single molecule resolution for quantifying the diffusion of Dam1 complex at higher concentrations, we mixed untagged Dam1 complex with a small amount of GFP-tagged Dam1 complex. At 500 pM, Dam1 complex diffused at least 60-fold more slowly than at 2 pM (Fig. S3 B). These observations indicate that oligomerization of the Dam1 complex slows its diffusion rate, as reported previously (Grishchuk et al., 2008a). Moreover, they imply that the enhanced binding of Ndc80 complex to microtubules that we have quantified here (Fig. 1, C–E) occurs via interaction with Dam1 complexes that are primarily in an oligomeric state.

In vitro, the Dam1 complex forms rings of 16–25 complexes that encircle microtubules (Miranda et al., 2007; Wang et al., 2007). To investigate whether rings are important for

Published May 17, 2010

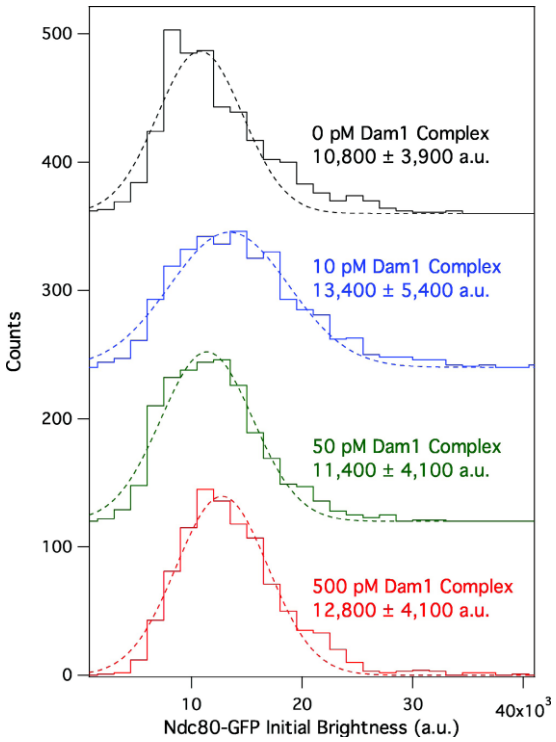

Figure 2. Dam1 complex does not affect the oligomerization state of the Ndc80 complex on microtubules. Mean initial brightness distributions of 10 pM GFP-tagged Ndc80 complex–binding events on microtubules with - out Dam1 complex (black histogram; n = 883 events), with 10 pM Dam1 complex (blue histogram; n = 966), 50 pM Dam1 complex (green histogram; n = 928), and 500 pM Dam1 complex (red histogram; n = 1,003). Dotted lines show Gaussian fits used to determine mean values ± SD. These values are similar to the mean brightness from rare single-bleach steps of GFP-tagged Ndc80 complex (9,300 ± 3,200 au; n = 11). For clarity, green, blue, and black histograms are offset vertically by 120, 240, and 360 counts, respectively.

interaction with the Ndc80 complex, we used negative-stain EM to quantify ring formation on taxol-stabilized microtubules (at 36 nM tubulin) across a range of Dam1 concentrations (Fig. 3). At 500 pM Dam1 complex, the highest concentration used in our TIRF assays, rings were absent. Instead, we observed small particles scattered around or attached to the filaments. The dimensions of these particles were consistent with Dam1 complex dimers (Wang et al., 2007). Rings first appear on microtubules at 1 nM Dam1 complex, substantially increase in density between 5 and 10 nM, and saturate at 100 nM (Table I). These findings are consistent with a strong and cooperative binding of the Dam1 complex to microtubules, as reported previously (Gestaut et al., 2008).

Although 500 pM Dam1 complex did not assemble into rings on microtubules at 36 nM tubulin, reducing the amount of tubulin could promote ring formation by increasing the density of Dam1 complex bound to microtubules. To explore the magnitude of this effect, we imaged 500 pM Dam1 complex on microtubules at fivefold lower tubulin (7 nM). Rings were again absent (n = 8 microtubules; 101 µm total). Further reductions in tubulin concentration were impractical because the microtubules became too sparse on the EM grids. Because the effective concentration of tubulin polymer in our TIRF assays was lower still (~1 nM), it remains possible that Dam1 complex rings contributed to the observed alterations in behavior of the Ndc80 complex. However, we note that two observations suggest that ring formation is not required for the initial interaction between the Ndc80 and Dam1 complexes. First, the Dam1 and Ndc80 complexes interact during velocity sedimentation, where the Dam1 complex is primarily in dimeric form (Fig. S1). Second, interactions between individual Ndc80 and Dam1 complexes can be observed directly in TIRF assays (albeit rarely; Fig. S2).

The Dam1 complex enhances attachment of the Ndc80 complex to dynamic microtubule tips

The Ndc80 complex has been shown to track efficiently with disassembling microtubule tips in vitro, but only when it is bound to beads or to antibodies (Powers et al., 2009). In contrast, the Dam1 complex tracks robustly with disassembling tips without artificial oligomerization (Westermann et al., 2006; Gestaut et al., 2008). Therefore, we tested whether the Dam1 complex enhances tip tracking by the Ndc80 complex. We grew microtubules from nonhydrolyzable GMPCPP seeds in the presence of free fluorescent-labeled tubulin and GTP. We visualized the behavior of GFP-tagged Ndc80 complex as microtubules disassembled after the free tubulin was removed. By itself, the Ndc80 complex localized only briefly to microtubule tips during disassembly (Fig. 4 A). Most binding events were transient and diffusive, which is similar to those seen on taxol-stabilized microtubules (Powers et al., 2009). In contrast, the addition of Dam1 complex, which accumulates at the disassembling microtubule tip (Fig. S3 C), substantially increased the tip tracking behavior of the Ndc80 complex (Fig. 4 A). Ndc80 complexes bound preferentially at the microtubule tip were more persistently attached and moved with the disassembling tip.

For quantification, we defined tip tracking as the colocalization of GFP-tagged Ndc80 complex with disassembling microtubule tips. In the presence of Dam1 complex, Ndc80 complex tracked with 78% (62/80) of disassembling microtubule tips over a mean distance of 1.2 ± 0.2 µm compared with only 27% (19/71) of tips over a mean distance of 0.13 ± 0.09 µm in the absence of Dam1 complex (Fig. 4 B). In the presence of the Dam1 complex, tip tracking events by the Ndc80 complex often continued until the tips reached the microtubule seeds. Therefore, we likely underestimate the effect of the Dam1 complex to enhance the ability of the Ndc80 complex to track disassembling tips.

We then used an optical trapping-based force clamp (Asbury et al., 2006; Franck et al., 2007, 2010; Powers et al., 2009) to test whether the Dam1 complex enhances the tip-tracking ability of Ndc80 complex while underload. We attached beads decorated with Ndc80 complex to the tips of assembling microtubules in the presence and absence of free Dam1 complex. We applied constant tensile force until the attachment broke, the microtubule switched to disassembly or, in a few cases, the

Published May 17, 2010

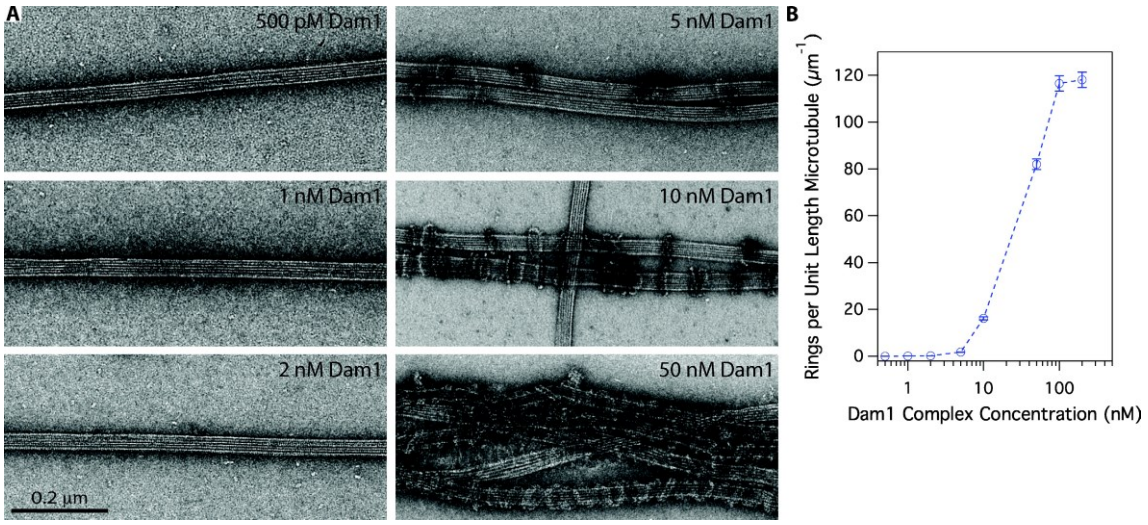

Figure 3. Assembly of oligomeric rings of the Dam1 complex around microtubules. (A) Negative-stain electron micrographs of oligomeric rings formed by the Dam1 complex around taxol-stabilized microtubules. (B) The number of rings observed per unit length (micrometers) of microtubule was quantified (statistics shown in Table I) and plotted against the total concentration of Dam1 complex. Error bars represent counting uncertainties.

event was terminated by other causes (e.g., the bead became stuck to the coverslip). In the absence of Dam1 complex, bead-bound Ndc80 complex formed persistent load-bearing attachments to assembling and disassembling microtubule tips (Fig. 5) as reported previously (Powers et al., 2009). While bearing 1.8 ± 0.4 pN (mean ± SD) of continuous load, travel distances during assembly were broadly distributed with a mean of 350 nm (n = 115). Detachment from assembling tips occurred at a rate of 0.026 ± 0.003 s^{-1} (Fig. 5 B). To mimic the likely arrangement in vivo, we added free Dam1 complex lacking an affinity tag so that it interacted with the beads only via its interaction with Ndc80 complex (i.e., direct Dam1 complex–bead interactions were prevented; see Materials and methods). In the presence of the Dam1 complex, the mean travel distance increased threefold to 1,100 nm (n = 42; $P = 3 \times 10^{-8}$ by Kolmogorov-Smirnov test), and the detachment rate decreased 6-fold to 0.005 ± 0.0008 s^{-1} (Fig. 5 B). Accordingly, plots of survival probability versus distance show that the couplers remained more persistently attached when Dam1 complex was present (Fig. 5 C).

We also developed a force ramp assay to test the coupling performance of bead-bound Ndc80 complex across a broader range of forces on both assembling and disassembling microtubule tips (Franck et al., 2010). After an initial preload period at ~1 pN constant force, we gradually increased the force on a tip-attached bead at a constant rate (0.25 pN s^{-1}) until the bead detached from the microtubule tip, the load limit of the trap (10–12 pN) was reached, or, in the case of disassembling filaments, the microtubule switched from shortening to growth (Fig. 6). The maximum force achieved before any one of these termination points was recorded for each event. Without Dam1 complex present, all events recorded during microtubule assembly ended in detachment. Most events during disassembly also ended in detachment (93/96), but a few ended with a shortening to growth transition (2/96) or when the trap load limit was reached (1/96). The resulting maximum forces were distributed narrowly, with means of 2.7 ± 0.1 pN (n = 101) during assembly and 2.7 ± 0.1 pN (n = 96) during disassembly (Fig. 6, E and F). The addition of Dam1 complex

Table I. EM of ring formation on microtubules at different Dam1 complex concentrations

Dam1 complex concentration	No. of microtubules	Total microtubule length	No. of rings	Ring density
nM		µm		$µm^{-1}$ [a]
0.5	27	259	0	0
1	16	280	20	0.1 ± 0.02
2	26	308	76	0.2 ± 0.03
5	26	256	450	2 ± 0.08
10	18	33	535	17 ± 0.7
50	13	16	1,312 [b]	82 ± 3
100	11	11	1,282 [b]	120 ± 3
200	9	11.5	1,358 [b]	120 ± 3

[a] Errors represent counting uncertainties.

[b] Rings stacked together in pairs to form doublets and/or coils.

Published May 17, 2010

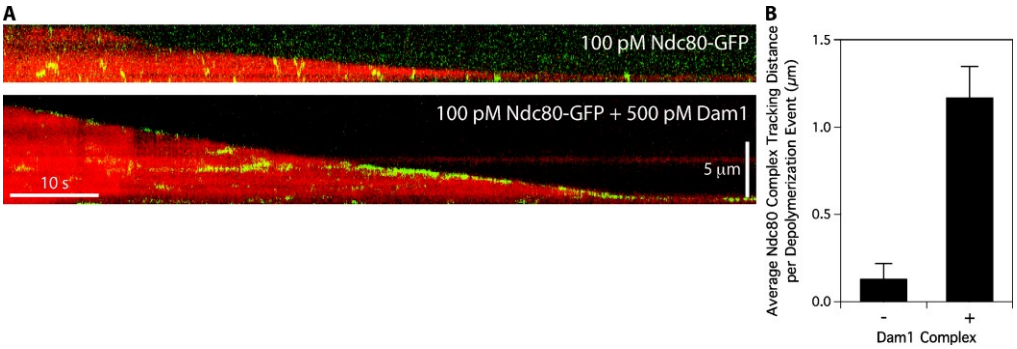

Figure 4. Ndc80 complex tracks with disassembling tips in the presence of Dam1 complex. (A) Representative two-color kymographs showing the tip tracking ability of 100 pM Ndc80 complex in the presence or absence of 500 pM Dam1 complex. Movement of GFP-tagged Ndc80 complex (green) is shown on disassembling microtubules (red). Concentrations are of free complexes in solution. (B) Mean tracking distance of Ndc80 complex per depolymerization event in the absence of Dam1 complex (n = 19) or in the presence of 500 pM Dam1 complex (n = 62). Error bars indicate SEM.

resulted in a clear improvement in the load-bearing capacity of the Ndc80 complex–coated beads. Most events recorded during assembly ended in detachment (112/131), but some persisted until the trap load limit was reached (19/131). Of the events recorded during disassembly, only about half ended in detachment (43/92). The remainder terminated when the microtubule switched to assembly (43/92), or, in a few cases, when the load limit was reached (6/92). The high frequency of shortening to growth transitions indicates that tension applied through linkages composed of both Ndc80 and Dam1 complexes promotes microtubule rescue, a phenomenon we saw previously using bead-bound Dam1 complex alone (Franck et al., 2007). The resulting maximum forces were distributed broadly with means of 5.2 ± 0.2 pN during assembly (n = 131) and 4.4 ± 0.2 pN during disassembly (n = 92), values that are twofold higher than in the absence of Dam1 complex (assembly, $P < 1 \times 10^{-8}$; disassembly, $P = 1 \times 10^{-8}$). These observations, together with the force clamp results, show that interactions between Dam1 and Ndc80 complexes enhance coupling to both assembling and disassembling microtubule tips under load. This enhancement persists across a range of loads (up to 10 pN), and it occurs under conditions in which the entire load is ultimately transmitted to the cargo through the Ndc80 complex.

Ipl1 phosphorylation regulates the interaction between Ndc80 and Dam1 complexes

We asked whether Ipl1 phosphorylation of the Dam1 complex regulates its interaction with the Ndc80 complex on microtubules. Phosphorylation of Ser20 on the Dam1 protein weakens the interaction of the Dam1 complex with microtubules (Gestaut et al., 2008). To determine how phosphorylation at sites other than Ser20 affects the interaction between the Dam1 and Ndc80 complexes, we used a modified Dam1 complex with a Ser20 to Ala mutation (S20A). With the S20A substitution, the Dam1 complex interacts with microtubules in a manner that is indistinguishable from the wild-type complex except that the interaction is insensitive to Ipl1 phosphorylation (Fig. S4, A and B). The phosphorylated S20A Dam1 complex also tracks with disassembling microtubule tips and is less diffusive at high concentrations, as expected for oligomers (Fig. S3). Phosphorylated S20A Dam1 complex also slows the disassembly of microtubules, as reported for wild-type Dam1 complex (Westermann et al., 2006; Franck et al., 2007; Grishchuk et al., 2008a).

In the presence of unphosphorylated S20A Dam1 complex, diffusion of the Ndc80 complex on microtubules is slowed, dissociation rate constant is decreased, and tip tracking is enhanced, as described for the wild-type Dam1 complex (Fig. 7). However, Ipl1 phosphorylation of the S20A Dam1 complex abolished the ability of Dam1 complex to slow the diffusion and decrease the dissociation rate constant of the Ndc80 complex (Fig. 7, B and C). Moreover, phosphorylated S20A Dam1 complex did not enhance the tip-tracking ability of the Ndc80 complex (Fig. 7 D). Control experiments were performed to ensure that after the initial Ipl1 phosphorylation reaction with the S20A Dam1 complex, residual Ipl1 activity was negligible (see Materials and methods; Fig. S5). Furthermore, the 10 proteins of the Dam1 complex do not dissociate from one another when the complex is phosphorylated by Ipl1 (Fig. S4 C). Because phosphorylation of the S20A Dam1 complex does not alter the behavior of the Dam1 complex alone but abolishes its ability to change the behavior of the Ndc80 complex, we conclude that Ipl1 phosphorylation of the Dam1 complex inhibits its interaction with the Ndc80 complex.

Discussion

The Dam1 complex acts as a processivity factor for the Ndc80 complex

Many molecular machines require factors that enhance their processivity. For example, the proliferating cell nuclear antigen sliding clamp is required for efficient DNA replication by DNA polymerase ε (Kelman, 1997). Likewise, dynactin is required for long-distance movement of cytoplasmic dynein along microtubules (King and Schroer, 2000). Kinetochores are processive and form persistent attachments to dynamic microtubule tips over the times and distances required for chromosome biorientation and segregation. However, the contribution of individual

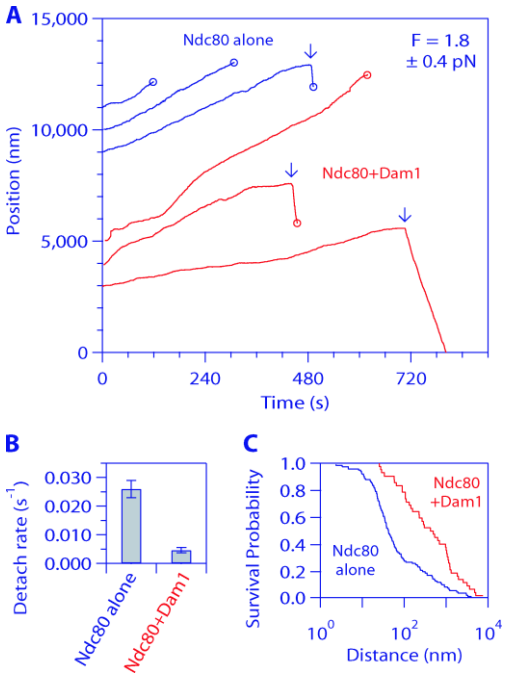

Figure 5. Dam1 complex enhances the coupling of bead-bound Ndc80 complex to assembling microtubule tips under fixed load. (A) Representative records of bead position versus time for microtubule tip attachments by bead-bound Ndc80 complex in the absence (blue traces) or presence (red traces) of free Dam1 complex during continuous application of tensile load. Increasing position represents assembly-coupled movement in the direction of applied force. Arrows mark transitions from assembly to disassembly. Decreasing position represents disassembly-driven movement against the applied force. Circles indicate detachment. For clarity, each record is offset vertically by an arbitrary amount. (B) Rates of bead detachment from assembling microtubule tips are estimated by counting the number of detachment events and dividing by total observation time. Error bars represent uncertainty based on Poisson statistics. (C) Survival probability versus distance for attachments composed of bead-bound Ndc80 complex in the absence (blue) or presence (red) of free Dam1 complex. The survival probability is the number of events that persisted beyond a given distance divided by the total number of events.

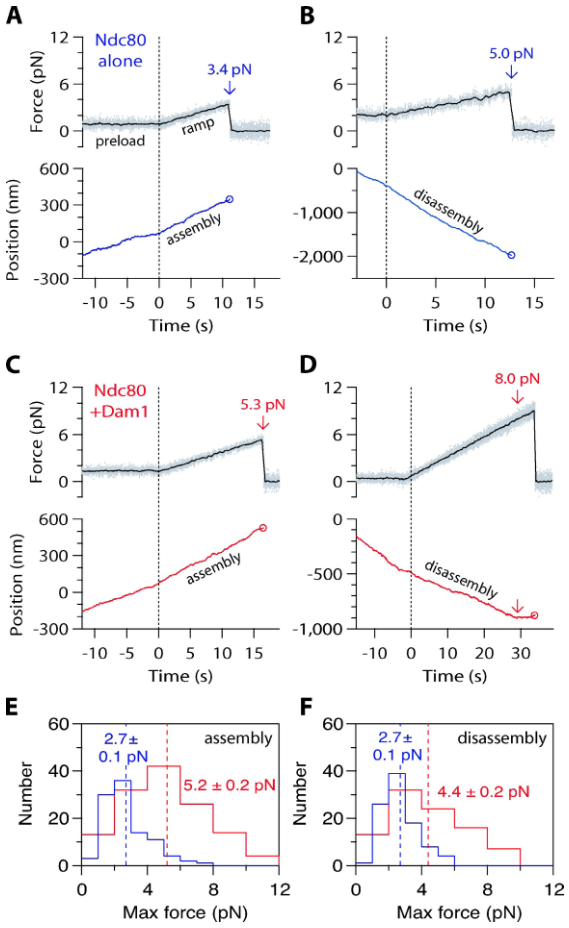

Figure 6. Dam1 complex enhances the coupling of bead-bound Ndc80 complex to assembling and disassembling microtubule tips across a range of loads. (A–D) Representative records showing tensile force (top) and bead position (bottom) versus time for bead-bound Ndc80 complexes attached to assembling and disassembling microtubule tips in the absence (A and B) or presence (C and D) of free Dam1 complex. The instrument was programmed to automatically increase the force at a constant rate (0.25 pN × s^{-1}) after ~500 nm of movement occurred. Arrows mark maximum forces, recorded either at rupture or when the microtubule switched from disassembly to assembly. Circles mark ruptures. (E) Distributions of maximum force for bead-bound Ndc80 complexes attached to assembling tips in the absence (blue histogram; n = 101) or presence (red histogram; n = 131) of free Dam1 complex. (F) Distributions of maximum force for bead-bound Ndc80 complexes attached to disassembling tips in the absence (blue histogram; n = 96), or presence (red histogram; n = 92) of free Dam1 complex. Dotted vertical lines indicate the mean for each distribution. Uncertainties represent standard errors.

components to the processivity of kinetochore–microtubule attachments is poorly understood. In this study, we show that the Dam1 complex enables the Ndc80 complex to track with disassembling microtubule tips over distances in excess of the length of the entire yeast spindle. We also show that the Dam1 complex strengthens the attachment of the Ndc80 complex to dynamic microtubule tips. In vivo, assembly of the Dam1 complex onto the kinetochore requires the Ndc80 complex (Janke et al., 2002). In our optical trap experiments, bead-bound Ndc80 complex was assayed with the Dam1 complex free in solution to mimic this arrangement in vitro. The increased ability of bead-bound Ndc80 complexes to bear load in the presence of free Dam1 complex indicates that tensile force can be transmitted through an Ndc80 complex–based linkage in a physiologically relevant arrangement.

We propose that the Dam1 complex acts as a processivity factor for the Ndc80 complex and that the two complexes cooperate to form load-bearing kinetochore–microtubule attachments. In vivo, the Ndc80 complex forms lateral attachments to spindle microtubules before kinetochore association of Dam1 complex and biorientation (Tanaka et al., 2005; Shimogawa et al., 2006). Our results are consistent with a model in which the Ndc80 complex initially mediates kinetochore attachment to microtubules. The Dam1 complex is later loaded onto the kinetochore to maintain attachment to dynamic microtubule tips. Association of the Dam1 complex is particularly important for these attachments to withstand the tensile forces required for biorientation.

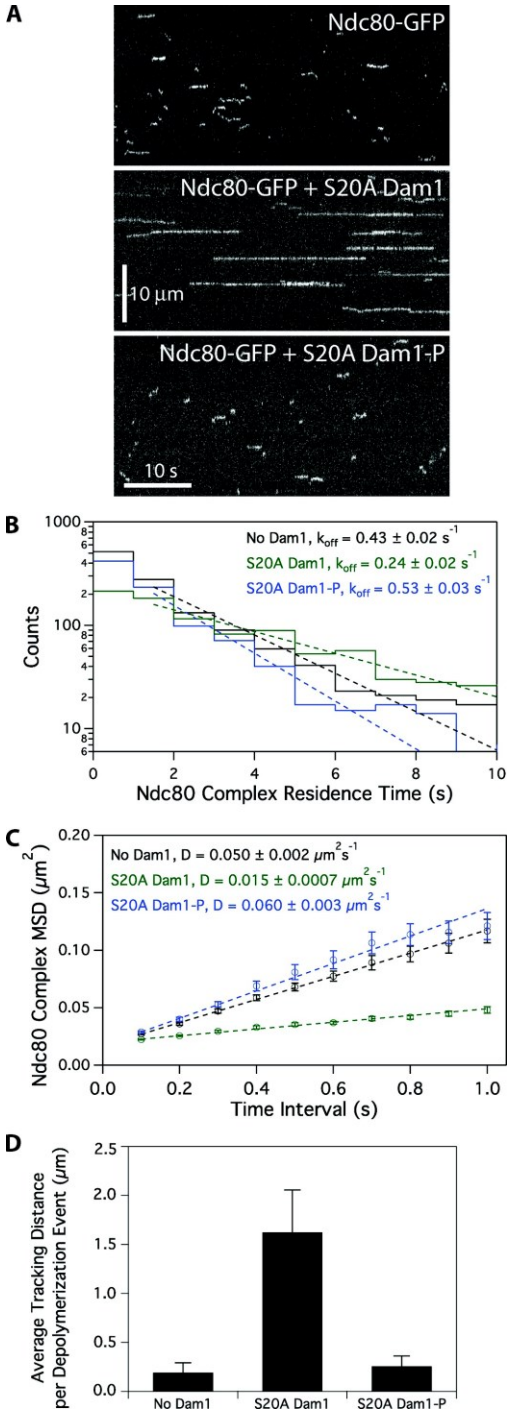

Figure 7. Ipl1 phosphorylation of the Dam1 complex regulates its interaction with the Ndc80 complex. (A) Representative kymographs showing changes in behavior of 10 pM Ndc80 complex with the addition of 500 pM S20A Dam1 complex with or without Ipl1 phosphorylation. Concentrations are of free complexes in solution. (B) Residence time distributions of 10 pM Ndc80 complex on microtubules without Dam1 complex (black histogram, n = 1,266 events), with 500 pM S20A Dam1 complex (green histogram, n = 1,081), and 500 pM Ipl1-phosphorylated S20A Dam1 complex (blue histogram, n = 974). Dotted lines show the weighted exponential fits used to determine dissociation rate constants, k_{off}. (C) Mean-squared displacement (MSD) is plotted against time for 10 pM Ndc80 complex on microtubules without Dam1 complex (black markers, n = 1,102), with 500 pM S20A Dam1 complex (green markers, n = 1,030), and with 500 pM Ipl1-phosphorylated S20A Dam1 complex (blue markers, n = 860). Dotted lines show the weighted linear fits used to determine diffusion constants, D. (D) Mean tracking distance of 100 pM Ndc80 complex per depolymerization event in the absence of Dam1 complex (n = 19), in the presence of 500 pM S20A Dam1 complex (n = 28), or in the presence of 500 pM Ipl1-phosphorylated S20A Dam1 complex (n = 39). Error bars indicate SEM.

The existence of a distinct and separable processivity factor also provides a point of regulation for corrective detachment.

A mechanism for aurora B–mediated corrective detachment

The regulatory mechanism that ensures chromosome biorientation has been proposed to respond to the level of tensile force on the kinetochore (Kelly and Funabiki, 2009). When kinetochores make attachments that generate little tension, such as monotelic or syntelic attachments, progression to anaphase is blocked. Key to this regulation, the conserved aurora B kinase is responsible for the release of aberrant kinetochore–microtubule attachments (Biggins et al., 1999; Tanaka et al., 2002; Hauf et al., 2003; Pinsky et al., 2006). We showed previously that phosphorylation by the yeast aurora B kinase Ipl1 at Ser20 of Dam1 decreases the affinity of the Dam1 complex for the microtubule lattice (Gestaut et al., 2008). We show in this study that Ipl1 phosphorylation of the Dam1 complex at sites other than Ser20 weakens its interaction with the Ndc80 complex. Collectively, these observations suggest that Ipl1 phosphorylation of the Dam1 complex promotes corrective detachment of kinetochores via two distinct mechanisms, decreasing the affinity of the Dam1 complex for both the Ndc80 complex and for microtubules. Regulation by aurora B kinase is a conserved feature of kinetochore function in all eukaryotes. Therefore, we propose that regulation at both the kinetochore–microtubule interface and between components of the kinetochore itself will extend to mechanisms of corrective detachment in higher eukaryotes.

Materials and methods

Protein expression and purification

The S. cerevisiae Ndc80 and Dam1 complexes were expressed from polycistronic vectors in E. coli as described previously (Wei et al., 2005; Gestaut et al., 2008, 2010; Powers et al., 2009). For TIRF microscopy, the Ndc80 complex Nuf2 subunit was tagged with GFP, and the Dam1 complex Dad1 subunit was tagged with GFP or mCherry. Complexes were purified by affinity chromatography and gel filtration as previously described (Asbury et al., 2006; Franck et al., 2007; Gestaut et al., 2008; Powers et al., 2009).

For optical trap bead assays, a tobacco etch virus (TEV) cleavage site was inserted adjacent to the His_6 affinity tag within the GFP-tagged Dam1 complex. The complex was purified by affinity chromatography and gel filtration as previously described (Gestaut et al., 2008). The cleavage reaction was performed in 50 mM phosphate buffer and 350 mM NaCl, pH 6.9, with 1 mM DTT, 0.5 mM EDTA, and recombinant TEV protease for

2 h at 4°C. TEV -cleaved Dam1 complex was isolated by gel filtration, and cleavage was verified by immunoblot analysis.

Phosphorylation of the Dam1 complex

Dam1 complex was phosphorylated with purified GST-Ipl1 and GST-Sli15 as described previously (Gestaut et al., 2008). The 50 µl reaction contained 4 µM GFP- or mCherry-tagged S20A Dam1 complex, 0.5 µM GST-Ipl1, 0.5 µM GST-Sli15 (residues 554–698), 200 mM NaCl, 10 mM ATP, 25 mM $MgCl_2$, and 50 mM Hepes buffer, pH 7.2. Reactions were incubated at 30°C for 90 min. Control reactions lacked GST-Ipl1 and GST-Sli15. Control reactions lacking ATP were also performed and gave similar results as previously reported (Gestaut et al., 2008). Ipl1 activity was not eliminated after the phosphorylation reaction. Therefore, to ensure that residual Ipl1 from the reaction did not affect our assays, we performed mock phosphorylation reactions using BSA in place of the Dam1 complex. The components of this mock reaction had no effect on the diffusion and dissociation rate constants of the Ndc80 complex either in the absence or presence of the Dam1 complex (Fig. S5).

TIRF microscopy

A custom TIRF illumination system was constructed for simultaneous excitation of Alexa Fluor 647 and GFP (Gestaut et al., 2008, 2010; Powers et al., 2009). Total internal reflection of a far-red laser (FTEC-635-0-25-PFQ; Blue Sky Research) and a blue laser (Sapphire 488–75; Coherent) was achieved using a through the objective arrangement with a 100× 1.4 NA Plan Apochromat lens (CFI; Nikon). Images from the far-red and green channels were projected side by side onto a cooled EM charge-coupled device camera (iXon 887-BI; Andor Technology).

A custom flow cell construction method was used (Gestaut et al., 2008, 2010; Powers et al., 2009). Glass slides (Gold Seal) were drilled with two holes along the short axis. Double-sided sticky tape (Scotch) was placed on either side of the holes to produce the walls of the flow channel. Silanized coverslips (Corning) were pressed firmly onto the tape, and the ends of the channel were sealed with vacuum grease. To draw fluid through the channel, a peristaltic pump was used via a custom adaptor attached above one of the holes on the glass slide with adhesive transfer tape (3M).

Flow cells were washed with three 100 µl vol dH_2O. To bind taxol-stabilized microtubules, we flowed in a modified "rigor" kinesin (G234A) lacking motor activity (Rice et al., 1999) diluted in BRB80 containing 8 mg × ml^{-1} BSA (BB80). Flow cells were washed with two 50 µl vol BB80, the second of which contained 10 µM taxol (BB80T). Alexa Fluor 647–labeled microtubules were diluted in BB80T and incubated in flow cells for 5 min. Flow cells were washed with two 50 µl vol BB80T. Proteins were then introduced, diluted in BB80T containing 0.02–0.1 mg × ml^{-1} κ-casein, 200 µg × ml^{-1} glucose oxidase, 35 µg × ml^{-1} catalase, 25 mM glucose, and 5 mM DTT. When assayed in combination, Ndc80 and Dam1 complexes were premixed before their introduction into flow cells. After flowing in the protein mixture, 2,000-frame videos were taken at 10 frames per second with iXon software (Andor Technology). All assays were performed at 26°C.

For disassembling microtubule assays, "rigor" kinesin was bound to flow cells and washed with 50 µl BB80 followed by 50 µl BB80 containing 0.1 mg ml^{-1} κ-casein and 1 mM GTP (growth buffer [GB]). Alexa Fluor 647–labeled GMPCPP microtubule seeds were bound and washed with two 50 µl vol GB. Microtubules were grown by incubating for ∼15 min in GB containing 2 mg × ml^{-1} tubulin (1:100; Alexa Fluor 647 labeled), 200 µg × ml^{-1} glucose oxidase, 35 µg ml^{-1} catalase, 25 mM glucose, and 5 mM DTT. Microtubule depolymerization was induced by buffer exchange removing free tubulin and simultaneously introducing proteins diluted in BB80 containing 0.1 mg × ml^{-1} κ-casein, 200 µg × ml^{-1} glucose oxidase, 35 µg × ml^{-1} catalase, 25 mM glucose, and 5 mM DTT. Videos were started concomitantly with induction of depolymerization and taken at 10 frames per second for 2,000 frames.

TIRF microscopy data analysis

Software analysis of TIRF microscopy data was performed using Labview (National Instruments) as previously described (Gestaut et al., 2008, 2010; Powers et al., 2009). The software generated the position and brightness of individual GFP-tagged complexes on microtubules over time. Custom Igor Pro (WaveMetrics) programs were used to generate histograms of Ndc80 complex residence times on microtubules. A weighted single exponential fit was applied to determine the mean residence time, τ, and to calculate the dissociation rate constant, $k_{off} = \tau^{-1}$. Association rate constants, k_{on}, were estimated as the number of observed Ndc80 complex–binding events per tubulin dimer per second divided by the free concentration of Ndc80 complex. Standard diffusion plots of mean-squared displacement versus time were generated in Igor Pro. A weighted linear fit was used to calculate the one-dimensional diffusion constant, D, of GFP-tagged complexes on microtubules.

To quantify Ndc80 complex tip tracking, brightness profiles along disassembling tips were created in Labview. Fluorescent signals at the tips were averaged across seven frames (0.7 s), and we required a minimum intensity threshold of 20% above background to score a tip-tracking event. For each individual frame, the instantaneous depolymerization rate was calculated as the change in tip position over 50 frames (5 s). A microtubule disassembly event was defined to start at the first appearance of GFP-tagged Ndc80 complex at the tip and to end when the rate of depolymerization dropped <0.03 µm × s^{-1}. Microtubule tips without tracking as defined by this criterion were omitted from further analysis. The total tracking distance for each individual tip was determined, and the mean tracking distance per depolymerization event was calculated.

To quantify binding to microtubules, we created brightness profiles of 500 pM mCherry-tagged Dam1 complex using our TIRF assay. After a 5-min incubation with taxol-stabilized microtubules, an image was recorded (six or seven images per condition). For each microtubule in the image, the integrated intensity of mCherry was measured in ImageJ (National Institutes of Health), and the brightness per unit length was calculated. Brightness per unit length values were averaged across all microtubules within one image and reported as means from multiple images.

EM

Taxol-stabilized microtubules were made by polymerizing cleared tubulin in a total volume of 40 µl BRB80 containing 1.75 mM GTP, 1 mM $MgCl_2$, and 3.5% DMSO at 37°C for 30 min. Various concentrations of Dam1 complex were mixed with taxol-stabilized microtubules to a final concentration of 36 nM tubulin in BRB80 containing 10 µM taxol and incubated for 15 min. Samples were prepared for analysis by EM as follows: carbon-coated copper grids were positively charged in a glow discharge device (Electron Microscopy Sciences) for 2 min. A 2-µl drop of sample was applied onto a freshly discharged grid and incubated for 20 s. Excess solution was blotted off, and the grid was washed twice with water and once with 0.075% uranyl formate before staining with uranyl formate. The stain was blotted off, and the grid was air dried. The preparations were viewed on a transmission electron microscope (Spirit T12; FEI) operating at 120 kV, and images were recorded on a 1,000 × 1,000 bottom-mount low-scan charge-coupled device camera (Gatan) at a nominal magnification of either 15,000 or 52,000× at the specimen level. For each preparation, the total number of Dam1 complex rings on microtubules was counted and divided by the total length of microtubules to generate a mean number of Dam1 complex rings per microtubule micron. In control experiments performed in the presence of blocking proteins (8 mg × ml^{-1} BSA and 0.02 mg × ml^{-1} κ-casein), rings were still absent at 500 pM Dam1 complex.

Optical trap instrumentation and bead preparation

Our optical trap has been described previously (Franck et al., 2007, 2010; Powers et al., 2009). The instrument is built around an inverted microscope (TE2000; Nikon) equipped for video-enhanced differential interference contrast imaging. Custom-mounted optics direct the infrared trapping laser (J20-BL10–106Q; Spectra Physics) through a 100× 1.4 NA oil infrared Plan Apochromat objective lens (CFI; Nikon), through a high NA oil immersion condenser, and onto a position-sensitive detector. During force clamp experiments, a computer feedback–controlled piezo specimen stage (P-517.3CL; Physik Instrumente) was programmed (Labview) to maintain a fixed offset between the tip-attached bead and the trap center by moving to accommodate changes in microtubule length, thereby keeping the tensile force constant. During force ramp experiments, the bead trap separation was increased at a fixed rate, 0.25 pN × s^{-1}, up to a preset maximum of 10–12 pN (just below the escape force of the trap). For both force ramp and force clamp experiments, the stage position was updated and stored to disk at 50 Hz. Bead trap separation was sampled at 40 kHz but decimated to 200 Hz for storage.

Beads were prepared as previously described (Powers et al., 2009). Ndc80 complex was linked to 0.44-µm-diameter streptavidin-coated beads (Spherotech) with biotinylated His_5 antibody (QIAGEN). Ndc80 complex was diluted to 13–15 nM in BB80 with 1 mM DTT and incubated with 6 pM beads at 4°C for ∼90 min. In some experiments, recombinant His_6-tagged GFP was used as a blocking agent. In this case, Ndc80 complex was diluted to 30 nM in BB80 with 1 mM DTT and incubated with 12 pM beads at 4°C for ∼90 min. These beads were mixed 1:1 with 6 µM GFP and incubated for an additional 30 min before use. The amount of complex per bead and the final bead concentration was the same in both protocols. Both protocols yielded a molar ratio of Ndc80 complexes to

beads of 2,200–2,500. Based on simple geometric considerations (Powers et al., 2009), we estimate that <100 Ndc80 complexes could simultaneously interact with the filament. The Ndc80 complex/bead ratio was chosen to create tip attachments of moderate strength, so the full force range of the optical trap could be used to assess the contribution of Dam1 complex to the Ndc80 complex–based attachments. Results obtained with and without the GFP block were statistically indistinguishable (Ndc80 complex during assembly, $P = 0.3010$; Ndc80 complex during disassembly, $P = 0.5518$; Ndc80 complex + Dam1 complex during assembly, $P = 0.1663$; Ndc80 complex + Dam1 complex during disassembly, $P = 0.8597$), so they were pooled and analyzed together.

Optical trap bead assays, data collection, and analysis

Flow chambers were constructed and functionalized as previously described (Powers et al., 2009; Franck et al., 2010). In brief, two lengths of double-sided sticky tape (Scotch) were placed across the width of a microscope slide (Gold Seal) to form an inverted chamber of 2–3-mm width. A cleaned coverslip (Corning) longer than the slide width was pressed firmly onto the tape to form the chamber bottom, the overhanging edges acting as reservoirs for pipetting and aspirating solutions through the chamber. The chamber was functionalized by introducing 1 vol 1 mg × ml^{-1} biotinylated BSA (Vector Laboratories) and incubating for >10 min at room temperature. The chamber was washed with ∼20 vol BRB80 followed by ∼20 vol 0.33 mg × ml^{-1} avidin DN (Vector Laboratories). After a second wash with ∼20 vol BRB80, stable biotinylated microtubule seeds were introduced and washed with a growth and blocking buffer, BRB80 containing 1 mM GTP, 2 mg × ml^{-1} κ-casein, and 2% pluronic F-187. Subsequently, we introduced Ndc80 complex–coated beads that were diluted eightfold into GB, BB80 containing 1 mM GTP, 1.4 mg × ml^{-1} tubulin, 1 mM DTT, 250 µg × ml^{-1} glucose oxidase, 30 µg × ml^{-1} catalase, and 4.5 µg × ml^{-1} glucose. In assays with Dam1 complex, His_6-cleaved GFP-tagged Dam1 complex was used at a final concentration of 9–15 nM and added to the bead mixture just before introduction into the flow chamber. Microtubule disassembly events either occurred by a spontaneous switch from assembly to disassembly or were induced by laser scission (Franck et al., 2010). All trap assays were performed at 26°C.

Records of bead position versus time were analyzed using custom software written in Igor Pro. Periods of microtubule assembly and disassembly were visually identified in the records. Detachments were scored when the force on a bead under load suddenly dropped to zero and the stage exhibited open-loop ("run away") movement. The maximum force was taken as the mean of the final 10 data points before event termination (detachment or microtubule assembly/disassembly state switching). The survival probability was calculated by dividing the number of events that persisted beyond a given distance by the total number of events.

A bead–microtubule-binding assay was used to verify that His_6-cleaved GFP-tagged Dam1 complex did not bind directly to the GFP-blocked beads. Taxol-stabilized microtubules were introduced into a flow chamber and given 1 min to adhere nonspecifically to the coverslip. After a wash and 10-min incubation with surface block (BRB80 with 2 mg × ml^{-1} κ-casein and 10 µM taxol), free beads were introduced. After waiting 10 min to allow beads to bind, the number of microtubule-attached beads was counted across many fields of view (each 822 µm^2). Beads decorated with Ndc80 complex bound microtubules at a density of 7,800 beads × mm^{-2} (1,355 beads in 210 fields of view), whereas beads blocked with GFP in the presence of free Dam1 complex bound at only 24 beads × mm^{-2} (five beads in 250 fields of view) under identical conditions.

Online supplemental material

Fig. S1 shows a weak interaction between the Ndc80 and Dam1 complexes in solution by velocity sedimentation. Fig. S2 shows kymographs of single-molecule Ndc80 and Dam1 complexes interacting on taxol-stabilized microtubules. Fig. S3 shows that the Dam1 complex oligomerizes on microtubules and tracks with disassembling microtubule tips. This behavior is unaffected by the S20A mutation and subsequent phosphorylation by Ipl1. Fig. S4 further shows that phosphorylation of S20A Dam1 complex does not affect its microtubule binding. In addition, phosphorylation does not cause disassembly of the wild-type Dam1 complex. Fig. S5 shows that the behavior of the Ndc80 complex on microtubules is unaffected by residual components of the Dam1 complex phosphorylation reaction. Online supplemental material is available at http://www.jcb.org/cgi/content/full/jcb.200910142/DC1.

We thank V. MacKay and B. Kennedy for help with velocity sedimentation experiments. We also thank A. Powers, M. Shimogawa, B. Graczyk, and M. Wargacki for helpful scientific discussion.

We thank the Murdock Charitable Trust and the Washington Research Foundation for generous support of our electron cryomicroscopy facility. This work was supported by a National Sciences and Engineering Research Council of Canada scholarship (to J.F. Tien), a National Institutes of Health traineeship (grant T32 GM008268 to N.T. Umbreit), a National Science Foundation Integrative Graduate Education and Research traineeship (grant DGE-0504573 to A.D. Franck), a Searle Scholar award (grant 06-L-111 to C.L. Asbury), a Packard Fellowship for Science and Engineering (grant 2006-30521 to C.L. Asbury), and by the National Institute of General Medical Sciences (grants R01GM40506 and R01GM79373 to T.N. Davis and C.L. Asbury, respectively). T. Gonen is a Howard Hughes Medical Institute early career scientist.

Submitted: 26 October 2009
Accepted: 2 April 2010

References

Akiyoshi, B., C.R. Nelson, J.A. Ranish, and S. Biggins. 2009. Analysis of Ipl1-mediated phosphorylation of the Ndc80 kinetochore protein in Saccharomyces cerevisiae. Genetics. 183:1591–1595. doi:10.1534/genetics.109.109041

Asbury, C.L., D.R. Gestaut, A.F. Powers, A.D. Franck, and T.N. Davis. 2006. The Dam1 kinetochore complex harnesses microtubule dynamics to produce force and movement. Proc. Natl. Acad. Sci. USA. 103:9873–9878. doi:10.1073/pnas.0602249103

Biggins, S., F.F. Severin, N. Bhalla, I. Sassoon, A.A. Hyman, and A.W. Murray. 1999. The conserved protein kinase Ipl1 regulates microtubule binding to kinetochores in budding yeast. Genes Dev. 13:532–544. doi:10.1101/gad.13.5.532

Cheeseman, I.M., S. Anderson, M. Jwa, E.M. Green, J. Kang, J.R. Yates III, C.S. Chan, D.G. Drubin, and G. Barnes. 2002. Phospho-regulation of kinetochore-microtubule attachments by the Aurora kinase Ipl1p. Cell. 111:163–172. doi:10.1016/S0092-8674(02)00973-X

Cheeseman, I.M., J.S. Chappie, E.M. Wilson-Kubalek, and A. Desai. 2006. The conserved KMN network constitutes the core microtubule-binding site of the kinetochore. Cell. 127:983–997. doi:10.1016/j.cell.2006.09.039

DeLuca, J.G., W.E. Gall, C. Ciferri, D. Cimini, A. Musacchio, and E.D. Salmon. 2006. Kinetochore microtubule dynamics and attachment stability are regulated by Hec1. Cell. 127:969–982. doi:10.1016/j.cell.2006.09.047

Franck, A.D., A.F. Powers, D.R. Gestaut, T. Gonen, T.N. Davis, and C.L. Asbury. 2007. Tension applied through the Dam1 complex promotes microtubule elongation providing a direct mechanism for length control in mitosis. Nat. Cell Biol. 9:832–837. doi:10.1038/ncb1609

Franck, A.D., A.F. Powers, D.R. Gestaut, T.N. Davis, and C.L. Asbury. 2010. Direct physical study of kinetochore-microtubule interactions by reconstitution and interrogation with an optical force clamp. Methods doi:10.1016/j.ymeth.2010.01.020.

Gaitanos, T.N., A. Santamaria, A.A. Jeyaprakash, B. Wang, E. Conti, and E.A. Nigg. 2009. Stable kinetochore-microtubule interactions dependon the Ska complex and its new component Ska3/C13Orf3. EMBO J. 28:1442–1452. doi:10.1038/emboj.2009.96

Gestaut, D.R., B. Graczyk, J. Cooper, P.O. Widlund, A. Zelter, L. Wordeman, C.L. Asbury, and T.N. Davis. 2008. Phosphoregulation and depolymerization-driven movement of the Dam1 complex do not require ring formation. Nat. Cell Biol. 10:407–414. doi:10.1038/ncb1702

Gestaut, D.R., J. Cooper, C.L. Asbury, T.N. Davis, and L. Wordeman. 2010. Reconstitution and functional analysis of kinetochore subcomplexes. Methods Cell Biol. In press.

Grishchuk, E.L., A.K. Efremov, V.A. Volkov, I.S. Spiridonov, N. Gudimchuk, S. Westermann, D. Drubin, G. Barnes, J.R. McIntosh, and F.I. Ataullakhanov. 2008a. The Dam1 ring binds microtubules strongly enough to be a processive as well as energy-efficient coupler for chromosome motion. Proc. Natl. Acad. Sci. USA. 105:15423–15428. doi:10.1073/pnas.0807859105

Grishchuk, E.L., I.S. Spiridonov, V.A. Volkov, A. Efremov, S. Westermann, D. Drubin, G. Barnes, F.I. Ataullakhanov, and J.R. McIntosh. 2008b. Different assemblies of the DAM1 complex follow shortening microtubules by distinct mechanisms. Proc. Natl. Acad. Sci. USA. 105:6918–6923. doi:10.1073/pnas.0801811105

Guimaraes, G.J., Y. Dong, B.F. McEwen, and J.G. Deluca. 2008. Kinetochore-microtubule attachment relies on the disordered N-terminal tail domain of Hec1. Curr. Biol. 18:1778–1784. doi:10.1016/j.cub.2008.08.012

Hanisch, A., H.H. Silljé, and E.A. Nigg. 2006. Timely anaphase onset requires a novel spindle and kinetochore complex comprising Ska1 and Ska2. EMBO J. 25:5504–5515. doi:10.1038/sj.emboj.7601426

Published May 17, 2010

Hauf, S., R.W. Cole, S. LaTerra, C. Zimmer, G. Schnapp, R. Walter, A. Heckel, J. van Meel, C.L. Rieder, and J.M. Peters. 2003. The small molecule Hesperadin reveals a role for Aurora B in correcting kinetochore–microtubule attachment and in maintaining the spindle assembly checkpoint. J. Cell Biol. 161:281–294. doi:10.1083/jcb.200208092

Inoué, S., and E.D. Salmon. 1995. Force generation by microtubule assembly/disassembly in mitosis and related movements. Mol. Biol. Cell. 6:1619–1640.

Janke, C., J. Ortíz, T.U. Tanaka, J. Lechner, and E. Schiebel. 2002. Four new subunits of the Dam1-Duo1 complex reveal novel functions in sister kinetochore biorientation. EMBO J. 21:181–193. doi:10.1093/emboj/21.1.181

Joglekar, A.P., K. Bloom, and E.D. Salmon. 2009. In vivo protein architecture of the eukaryotic kinetochore with nanometer scale accuracy. Curr. Biol. 19:694–699. doi:10.1016/j.cub.2009.02.056

Keating, P., N. Rachidi, T.U. Tanaka, and M.J. Stark. 2009. Ipl1-dependent phosphorylation of Dam1 is reduced by tension applied on kinetochores. J. Cell Sci. 122:4375–4382. doi:10.1242/jcs.055566

Kelly, A.E., and H. Funabiki. 2009. Correcting aberrant kinetochore microtubule attachments: an Aurora B-centric view. Curr. Opin. Cell Biol. 21:51–58. doi:10.1016/j.ceb.2009.01.004

Kelman, Z. 1997. PCNA: structure, functions and interactions. Oncogene. 14:629–640. doi:10.1038/sj.onc.1200886

Kemmler, S., M. Stach, M. Knapp, J. Ortiz, J. Pfannstiel, T. Ruppert, and J. Lechner. 2009. Mimicking Ndc80 phosphorylation triggers spindle assembly checkpoint signalling. EMBO J. 28:1099–1110. doi:10.1038/emboj.2009.62

King, S.J., and T.A. Schroer. 2000. Dynactin increases the processivity of the cytoplasmic dynein motor. Nat. Cell Biol. 2:20–24. doi:10.1038/71338

Kline-Smith, S.L., S. Sandall, and A. Desai. 2005. Kinetochore-spindle microtubule interactions during mitosis. Curr. Opin. Cell Biol. 17:35–46. doi:10.1016/j.ceb.2004.12.009

Lampert, F., P. Hornung, and S. Westermann. 2010. The Dam1 complex confers microtubule plus end–tracking activity to the Ndc80 kinetochore complex. J. Cell Biol. 189:641–649.

Maddox, P., A. Straight, P. Coughlin, T.J. Mitchison, and E.D. Salmon. 2003. Direct observation of microtubule dynamics at kinetochores in Xenopus extract spindles: implications for spindle mechanics. J. Cell Biol. 162:377–382. doi:10.1083/jcb.200301088

Miranda, J.J., D.S. King, and S.C. Harrison. 2007. Protein arms in the kinetochore-microtubule interface of the yeast DASH complex. Mol. Biol. Cell. 18:2503–2510. doi:10.1091/mbc.E07-02-0135

Pinsky, B.A., C. Kung, K.M. Shokat, and S. Biggins. 2006. The Ipl1-Aurora protein kinase activates the spindle checkpoint by creating unattached kinetochores. Nat. Cell Biol. 8:78–83. doi:10.1038/ncb1341

Powers, A.F., A.D. Franck, D.R. Gestaut, J. Cooper, B. Gracyzk, R.R. Wei, L. Wordeman, T.N. Davis, and C.L. Asbury. 2009. The Ndc80 kinetochore complex forms load-bearing attachments to dynamic microtubule tips via biased diffusion. Cell. 136:865–875. doi:10.1016/j.cell.2008.12.045

Raaijmakers, J.A., M.E. Tanenbaum, A.F. Maia, and R.H. Medema. 2009. RAMA1 is a novel kinetochore protein involved in kinetochore-microtubule attachment. J. Cell Sci. 122:2436–2445. doi:10.1242/jcs.051912

Rice, S., A.W. Lin, D. Safer, C.L. Hart, N. Naber, B.O. Carragher, S.M. Cain, E. Pechatnikova, E.M. Wilson-Kubalek, M. Whittaker, et al. 1999. A structural change in the kinesin motor protein that drives motility. Nature. 402:778–784. doi:10.1038/45483

Shang, C., T.R. Hazbun, I.M. Cheeseman, J. Aranda, S. Fields, D.G. Drubin, and G. Barnes. 2003. Kinetochore protein interactions and their regulation by the Aurora kinase Ipl1p. Mol. Biol. Cell. 14:3342–3355. doi:10.1091/mbc.E02-11-0765

Shimogawa, M.M., B. Graczyk, M.K. Gardner, S.E. Francis, E.A. White, M. Ess, J.N. Molk, C. Ruse, S. Niessen, J.R. Yates III, et al. 2006. Mps1 phosphorylation of Dam1 couples kinetochores to microtubule plus ends at metaphase. Curr. Biol. 16:1489–1501. doi:10.1016/j.cub.2006.06.063

Skibbens, R.V., V.P. Skeen, and E.D. Salmon. 1993. Directional instability of kinetochore motility during chromosome congression and segregation in mitotic newt lung cells: a push-pull mechanism. J. Cell Biol. 122:859–875. doi:10.1083/jcb.122.4.859

Skibbens, R.V., C.L. Rieder, and E.D. Salmon. 1995. Kinetochore motility after severing between sister centromeres using laser microsurgery: evidence that kinetochore directional instability and position is regulated by tension. J. Cell Sci. 108:2537–2548.

Tanaka, T.U., and A. Desai. 2008. Kinetochore-microtubule interactions: the means to the end. Curr. Opin. Cell Biol. 20:53–63.

Tanaka, T.U., N. Rachidi, C. Janke, G. Pereira, M. Galova, E. Schiebel, M.J. Stark, and K. Nasmyth. 2002. Evidence that the Ipl1-Sli15 (Aurora kinase-INCENP) complex promotes chromosome bi-orientation by altering kinetochore-spindle pole connections. Cell. 108:317–329. doi:10.1016/S0092-8674(02)00633-5

Tanaka, K., N. Mukae, H. Dewar, M. van Breugel, E.K. James, A.R. Prescott, C. Antony, and T.U. Tanaka. 2005. Molecular mechanisms of kinetochore capture by spindle microtubules. Nature. 434:987–994. doi:10.1038/nature03483

Wan, X., R.P. O'Quinn, H.L. Pierce, A.P. Joglekar, W.E. Gall, J.G. DeLuca, C.W. Carroll, S.T. Liu, T.J. Yen, B.F. McEwen, et al. 2009. Protein architecture of the human kinetochore microtubule attachment site. Cell. 137:672–684. doi:10.1016/j.cell.2009.03.035

Wang, H.W., V.H. Ramey, S. Westermann, A.E. Leschziner, J.P. Welburn, Y. Nakajima, D.G. Drubin, G. Barnes, and E. Nogales. 2007. Architecture of the Dam1 kinetochore ring complex and implications for microtubule-driven assembly and force-coupling mechanisms. Nat. Struct. Mol. Biol. 14:721–726. doi:10.1038/nsmb1274

Wei, R.R., P.K. Sorger, and S.C. Harrison. 2005. Molecular organization of the Ndc80 complex, an essential kinetochore component. Proc. Natl. Acad. Sci. USA. 102:5363–5367. doi:10.1073/pnas.0501168102

Welburn, J.P., E.L. Grishchuk, C.B. Backer, E.M. Wilson-Kubalek, J.R. Yates III, and I.M. Cheeseman. 2009. The human kinetochore Ska1 complex facilitates microtubule depolymerization-coupled motility. Dev. Cell. 16:374–385. doi:10.1016/j.devcel.2009.01.011

Westermann, S., H.W. Wang, A. Avila-Sakar, D.G. Drubin, E. Nogales, and G. Barnes. 2006. The Dam1 kinetochore ring complex moves processively on depolymerizing microtubule ends. Nature. 440:565–569. doi:10.1038/nature04409

T ien et al., http://www .jcb.org/cgi/content/full/jcb.200910142/DC1

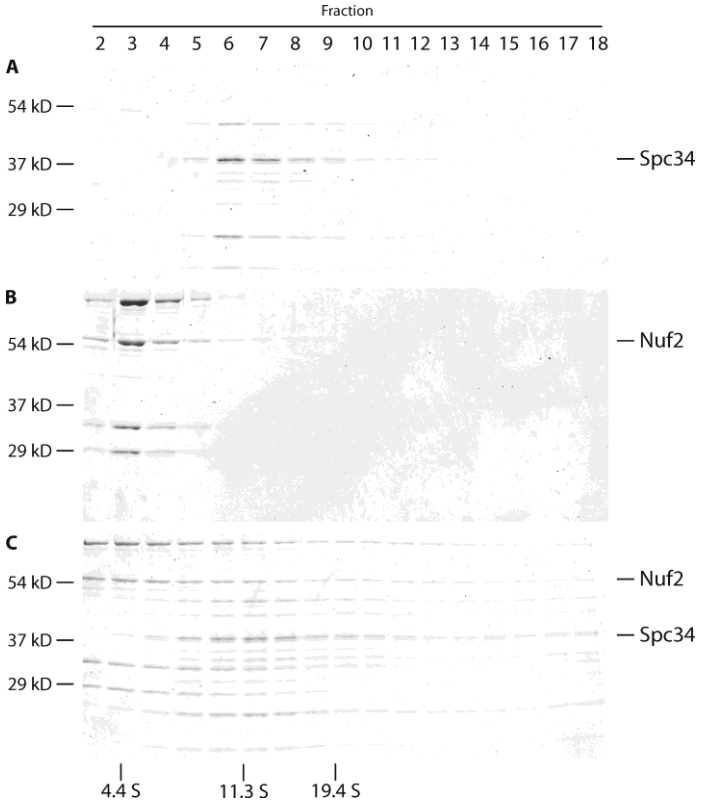

Figure S1. Ndc80 and Dam1 complexes interact weakly free in solution. The interaction between Ndc80 and Dam1 complexes free in solution was assayed by velocity sedimentation. 240 µl samples were layered onto 4.75 ml linear sucrose gradients (8–32%). Gradients were centrifuged at 189,000 g at 4°C for 6 h, and 265 µl fractions were collected. Fraction 1 is the top of the gradient. BSA (4.4S), catalase (11.3S), and thyroglobulin (19.4S) were used as standards. When assayed alone and together, Ndc80 complex and Dam1 complex had a sedimentation coefficient of 4.4S and 11.3S, respectively. Based on a Stokes radius of 9.9 nm, as determined by gel filtration, the molecular mass of the Dam1 complex was calculated to be ~470 kD (Siegel and Monty, 1966). Therefore, at the concentration in this assay, the 204-kD Dam1 complex exists primarily as a dimer free in solution. The positions of the Dam1 complex component Spc34 and the Ndc80 complex component Nuf2 are indicated on the right. (A–C) 2 µM Dam1 complex (A), 1 µM Ndc80 complex (B), and 2 µM Dam1 complex and 1 µM Ndc80 complex in combination (C) are shown.

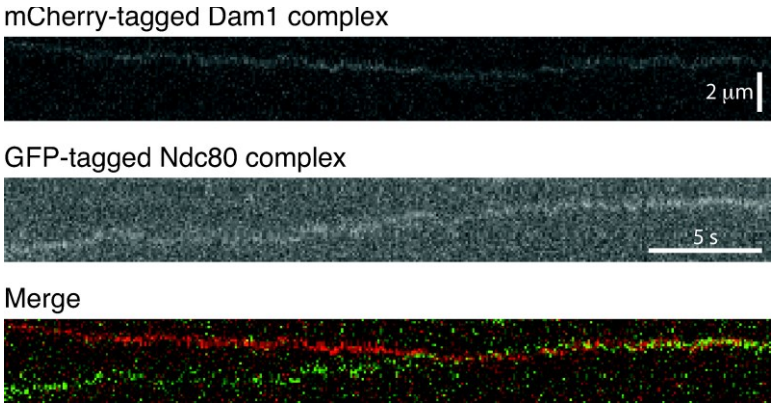

Figure S2. The Ndc80 and Dam1 complexes interact on microtubules. Representative kymograph showing the diffusion of 10 pM GFP-tagged Ndc80 complex and 2 pM mCherry-tagged Dam1 complex on microtubules. Both complexes are diffusive alone but appear to diffuse more slowly when they interact on microtubules.

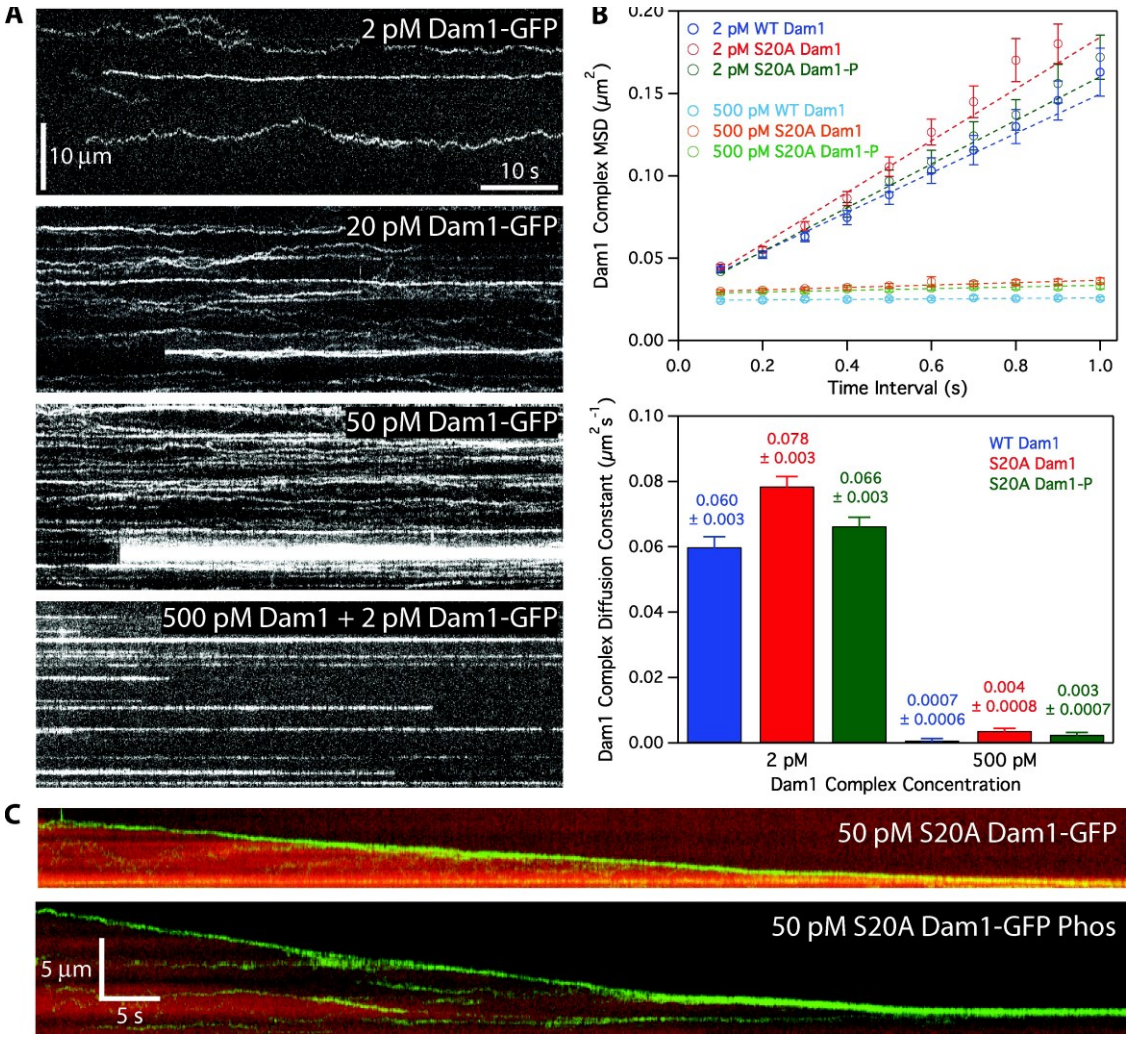

Figure S3. The Dam1 complex oligomerizes on microtubules and tracks with disassembling tips. (A) Representative kymographs showing changes in Dam1 complex behavior as it oligomerizes on microtubules. At 2 pM GFP-tagged Dam1 complex, single monomers were discernable. At 20 and 50 pM, slowly diffusing oligomers were seen as lines. At 500 pM Dam1 complex, the behaviors of individual oligomers were traced by visualizing a small proportion of labeled complex. Concentrations are of free complexes in solution. (B) Oligomerization of Dam1 complex slows its diffusion on taxol-stabilized microtubules, and oligomerization of S20A Dam1 complex is not abolished by Ipl1 phosphorylation. (top) Mean-squared displacement (MSD) is plotted against time for 2 pM wild-type (WT) Dam1 complex (blue markers; n = 188), 2 pM S20A Dam1 complex (red markers; n = 327), 2 pM Ipl1-phosphorylated S20A Dam1 complex (green markers; n = 346), 500 pM wild-type Dam1 complex (light blue markers; n = 129), 500 pM S20A Dam1 complex (orange markers; n = 188), and 500 pM Ipl1-phosphorylated S20A Dam1 complex (light green markers; n = 231). At 500 pM Dam1 complex, the behaviors of individual oligomers were traced by visualizing a small proportion of labeled complex. Markers are mean values ± SEM. Dotted lines show the weighted linear fits used to determine diffusion constants, D. (bottom) Diffusion constants derived from mean-squared displacement versus time plots are summarized as a bar graph. Wild-type Dam1 complex (blue bars), S20A Dam1 complex (red bars), and Ipl1-phosphorylated S20A Dam1 complex (green bars) are shown. Error bars indicate SEM. (C) Representative two-color kymographs demonstrating the tip-tracking ability of Ipl1-phosphorylated S20A Dam1 complex. Movement of 50 pM GFP-tagged unphosphorylated and phosphorylated S20A Dam1 complex (green) is shown on disassembling microtubules (red).

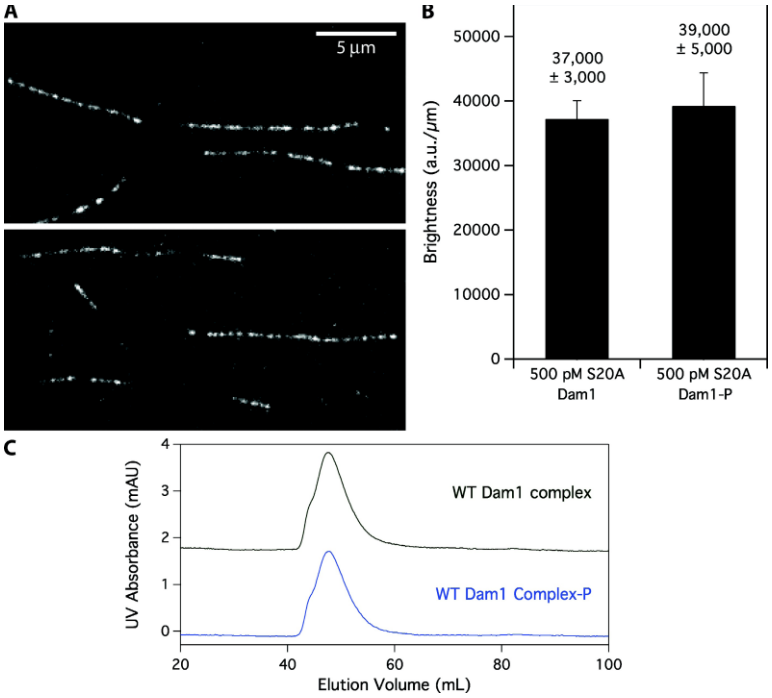

Figure S4. Phosphorylation does not affect microtubule binding of S20A Dam1 complex and does not cause disassembly of wild-type Dam1 complex. (A) Representative images of mCherry-tagged S20A Dam1 complex on microtubules. (top) 500 pM S20A Dam1 complex. (bottom) 500 pM Ipl1-phosphorylated S20A Dam1 complex. (B) Image means of mCherry brightness per unit length microtubules for unphosphorylated (n = 6 images, representing 68 microtubules, totaling 790 µm) and phosphorylated (n = 7 images, representing 51 microtubules, totaling 754 µm) S20A Dam1 complex. Error bars indicate SEM. (C) Unphosphorylated and Ipl1-phosphorylated wild-type (WT) Dam1 complexes each migrate as a single peak during gel filtration and elute at a volume consistent with previously reported values (Gestaut et al., 2008). The elution profile for unphosphorylated Dam1 complex is offset vertically by 2 mAU.

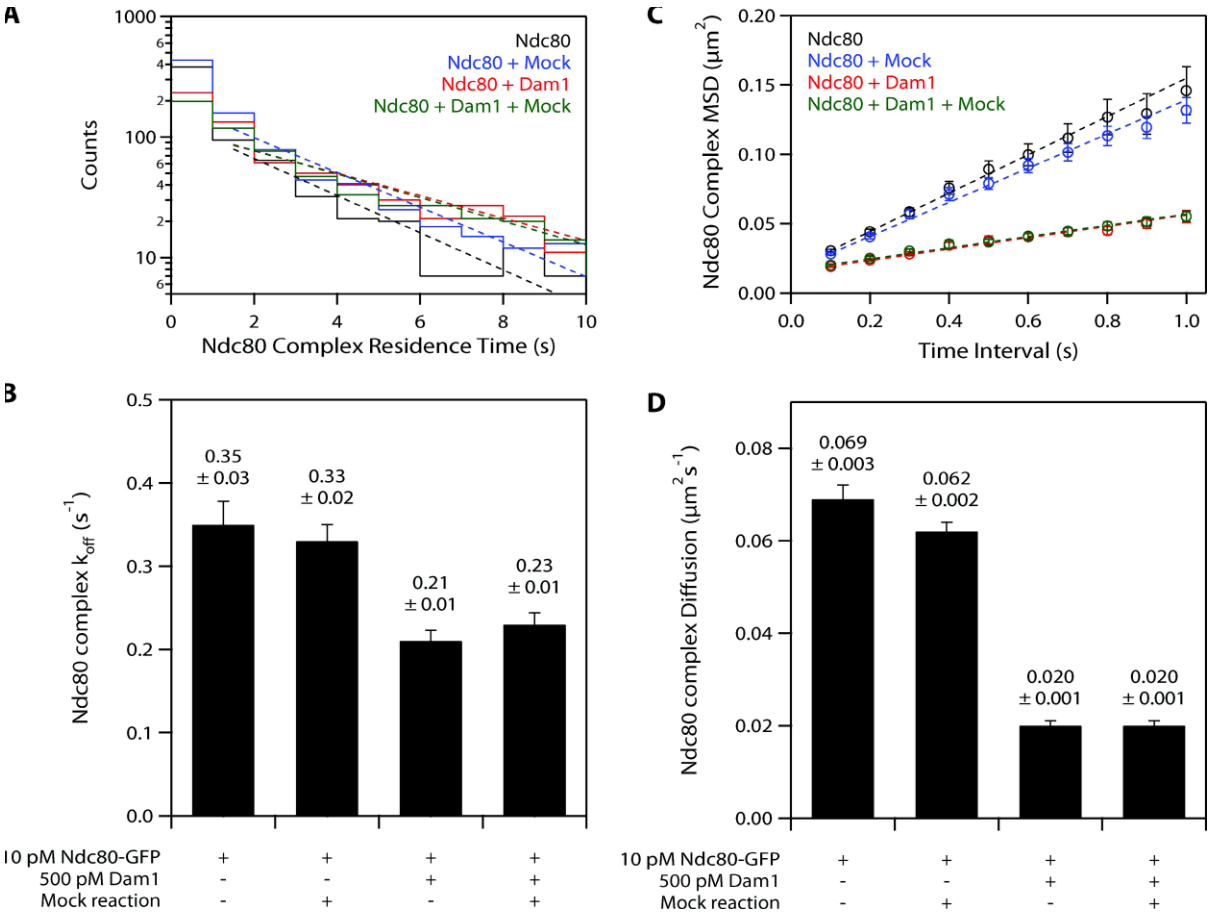

Figure S5. Residual components of Ipl1 phosphorylation reactions have no effect on the behavior of the Ndc80 complex on microtubules. Mock Ipl1 phosphorylation reactions were performed with BSA in place of Dam1 complex and added to TIRF assays at concentrations as in Fig. 6 (63 pM Ipl1, 63 pM Sli15, and 1.3 μM ATP). (A) Residence time distributions of 10 pM GFP-tagged Ndc80 complex on microtubules alone (black histogram; n = 692), with mock reaction (blue histogram; n = 869), 500 pM Dam1 complex (red histogram; n = 752), and 500 pM Dam1 complex and mock reaction (green histogram; n = 699). Dotted lines show the weighted exponential fits used to determine dissociation rate constants, k_{off}. (B) Dissociation rate constants derived from histograms are summarized as a bar graph. (C) Mean-squared displacement (MSD) is plotted against time for 10 pM GFP-tagged Ndc80 complex on microtubules alone (black markers; n = 472), with mock reaction (blue markers; n = 670), 500 pM Dam1 complex (red markers; n = 636), and 500 pM Dam1 complex and mock reaction (green markers; n = 586). Dotted lines show the weighted linear fits used to determine diffusion constants, D. (D) Diffusion rate constants derived from mean-squared displacement versus time plots are summarized as a bar graph. Error bars indicate SEM.

References

Gestaut, D.R., B. Graczyk, J. Cooper, P.O. Widlund, A. Zelter, L. Wordeman, C.L. Asbury, and T.N. Davis. 2008. Phosphoregulation and depolymerization-driven movement of the Dam1 complex do not require ring formation. Nat. Cell Biol. 10:407–414. doi:10.1038/ncb1702

Siegel, L.M., and K.J. Monty. 1966. Determination of molecular weights and frictional ratios of proteins in impure systems by use of gel filtration and density gradient centrifugation. Application to crude preparations of sulfite and hydroxylamine reductases. Biochim. Biophys. Acta. 112:346–362. doi:10.1016/0926-6585(66)90333-5

Appendix B

The Ndc80 kinetochore complex directly modulates microtubule dynamics

Umbreit, N. T., D. R. Gestaut, J. F. Tien, B. S. Vollmar, T. Gonen, C.L. Asbury, and T.N. Davis.

Proceedings of the National Academy of Sciences of the United States of America (2012) 109: 16113-16118.

The Ndc80 kinetochore complex directly modulates microtubule dynamics

Neil T. Umbreit[a,1], Daniel R. Gestaut[a,1,2], Jerry F. Tien[a,1], Breanna S. Vollmar[a,3], Tamir Gonen[a,b,3], Charles L. Asbury[c], and Trisha N. Davis[a,4]

[a]Department of Biochemistry, [c]Department of Physiology and Biophysics, and [b]Howard Hughes Medical Institute, University of Washington, Seattle, WA 98195

Edited by John Carbon, University of California, Santa Barbara, CA, and approved August 2, 2012 (received for review June 5, 2012)

The conserved Ndc80 complex is an essential microtubule-binding component of the kinetochore. Recent findings suggest that the Ndc80 complex influences microtubule dynamics at kinetochores in vivo. However, it was unclear if the Ndc80 complex mediates these effects directly, or by affecting other factors localized at the kinetochore. Using a reconstituted system in vitro, we show that the human Ndc80 complex directly stabilizes the tips of disassembling microtubules and promotes rescue (the transition from microtubule shortening to growth). In vivo, an N-terminal domain in the Ndc80 complex is phosphorylated by the Aurora B kinase. Mutations that mimic phosphorylation of the Ndc80 complex prevent stable kinetochore-microtubule attachment, and mutations that block phosphorylation damp kinetochore oscillations. We find that the Ndc80 complex with Aurora B phosphomimetic mutations is defective at promoting microtubule rescue, even when robustly coupled to disassembling microtubule tips. This impaired ability to affect dynamics is not simply because of weakened microtubule binding, as an N-terminally truncated complex with similar binding affinity is able to promote rescue. Taken together, these results suggest that in addition to regulating attachment stability, Aurora B controls microtubule dynamics through phosphorylation of the Ndc80 complex.

mitosis | Hec1 | single molecule | optical trap | total internal reflection fluorescence microscopy

During mitosis, replicated chromosomes are segregated by the mitotic spindle, a bipolar array of dynamic microtubules. Each chromatid is linked to a bundle of microtubules (a "K-fiber") by a kinetochore. To ensure accurate chromosome segregation, regulatory mechanisms detect and correct errors in attachments between kinetochores and spindle microtubules. The conserved Aurora B kinase plays a crucial role in the resolution of aberrant kinetochore-microtubule attachments (1). Aurora B has many identified targets at the kinetochore, and it is generally thought that phosphorylation of these targets triggers the release of incorrect attachments (2–7). However, emerging evidence suggests that Aurora B activity does not always result in kinetochore-microtubule detachment. For example, early in mitosis when merotelic attachments are more prevalent, phosphorylation of the Ndc80 complex (the key microtubule-binding component of the kinetochore) is relatively high, yet kinetochores do not appear to release from their K-fibers (8, 9). Similarly, syntelic attachments formed in the presence of a reversible Aurora B inhibitor are not immediately released when the kinase is reactivated (10). Instead, the K-fiber microtubules disassemble, carrying the kinetochores back to the centrosome, where the attachments are corrected by an unknown mechanism. These results suggest that Aurora B additionally acts to regulate microtubule dynamics as a part of its mechanism of error correction.

Additional findings suggest that Aurora B modulates microtubule dynamics through regulation of the Ndc80 complex. A component of the Ndc80 complex, the Hec1 protein, has a disordered N-terminal tail that is targeted by Aurora B in vivo (11, 12). In PtK cells, preventing phosphorylation of these target sites not only results in hyperstable kinetochore-microtubule attachments, but also damped kinetochore oscillations (8). The abnormal oscillations could be explained by direct or indirect contributions from the Ndc80 complex. The Ndc80 complex could itself directly control microtubule dynamics in response to Aurora B activity. An alternative (but not mutually exclusive) explanation is that phosphorylation of Hec1 alters the localization of other factors that modulate dynamics. These factors may include the microtubule stabilizer EB1 and the microtubule depolymerase MCAK, both of which are also targets of Aurora B (13–19).

Here, we show that the human Ndc80 complex directly stabilizes the tips of disassembling microtubules, slows the rate of disassembly, and promotes microtubule rescue (the transition from microtubule shortening to growth) in vitro. In contrast, the Ndc80 complex with mutations mimicking Aurora B phosphorylation was impaired in its ability to influence microtubule dynamics, even when tracking with the tips of disassembling microtubules. This diminished ability of the phosphomimetic complex to affect dynamics is not solely a result of weakened microtubule binding, as an N-terminally truncated complex with similar affinity was still able to promote rescue. These results suggest that Aurora B modulates microtubule dynamics through regulation of the Ndc80 complex, and this mechanism could be separable from effects on attachment stability.

Results

Characterization of Full-Length Human Ndc80 Complex. The conserved Ndc80 complex is an essential microtubule-binding component of the kinetochore (20). Although the Ndc80 complex from yeast and worms has been extensively studied in vitro (21–26), most work on the human complex has been limited to the use of truncated forms (26–31). We expressed and purified full-length human Ndc80 complex from *Escherichia coli* for in vitro characterization (Fig. S1). As seen by negative-stain EM, this recombinant Ndc80 complex bound to taxol-stabilized microtubules (Fig. 1*A*). Using total internal reflection fluorescence (TIRF) microscopy, we visualized single molecules of GFP-tagged Ndc80 complex on taxol-stabilized microtubules (Fig. 1*B* and Fig. S2) and measured their dissociation and diffusion rate constants ($k_{off} = 0.21 \pm 0.01\ s^{-1}$, $D = 0.018 \pm 0.001\ \mu m^2 \cdot s^{-1}$) (Fig. 1 *C* and *D*). The affinity and cooperativity of microtubule binding were

Author contributions: N.T.U., D.R.G., J.F.T., T.G., C.L.A., and T.N.D. designed research; N.T.U., D.R.G., J.F.T., B.S.V., and T.G. performed research; B.S.V. and T.G. contributed new reagents/analytic tools; N.T.U., D.R.G., J.F.T., C.L.A., and T.N.D. analyzed data; and N.T.U., D.R.G., and J.F.T. wrote the paper.

The authors declare no conflict of interest.

This article is a PNAS Direct Submission.

See Commentary on page 15972.

[1]N.T.U., D.R.G., and J.F.T. contributed equally to this work.

[2]Present address: Department of Biology, Stanford University, Stanford, CA 94305.

[3]Present address: Janelia Farm Research Campus, Howard Hughes Medical Institute, Ashburn, VA 20147.

[4]To whom correspondence should be addressed. E-mail: tdavis@u.washington.edu.

This article contains supporting information online at www.pnas.org/lookup/suppl/doi:10.1073/pnas.1209615109/-/DCSupplemental.

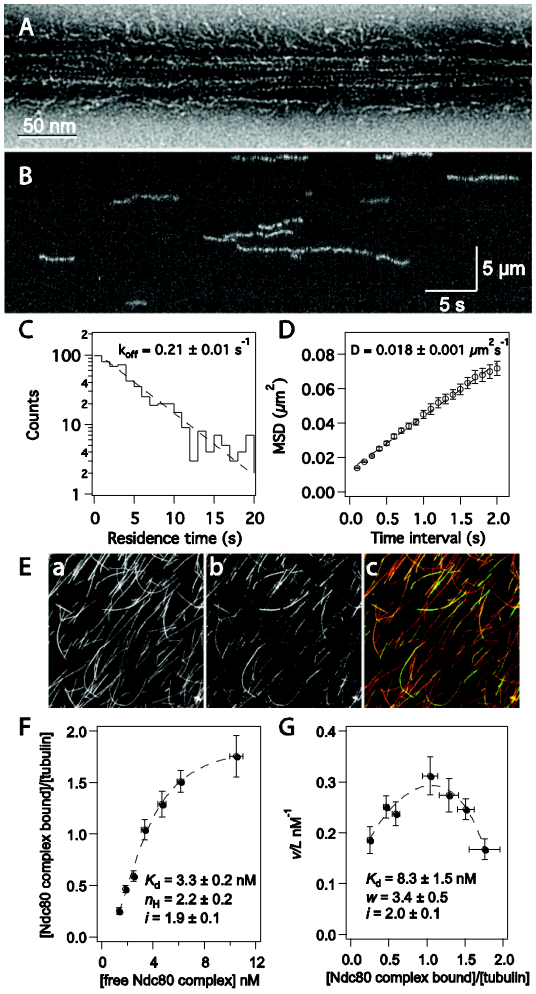

Fig. 1. The human Ndc80 complex binds to and diffuses along the microtubule lattice. (*A*) Negative-stain electron micrograph of the Ndc80 complex on a taxol-stabilized microtubule. (*B*) A representative kymograph showing the binding and diffusion of Ndc80 complex (5 pM complex in solution) on taxol-stabilized microtubules. Position along the microtubule is depicted on the vertical axis over time on the horizontal axis. (*C*) Residence time distributions of GFP-tagged Ndc80 complex on microtubules fit with a single exponential (dashed line) to calculate the off-rate constant, k_{off}. (*D*) Mean-squared displacement (MSD) ± SEM vs. time lag. A linear fit to the data (dashed line) was used to determine the diffusion constant, *D*. (*C* and *D*) n = 584. (*E*) Representative image from the bulk microtubule binding assay with GFP-tagged Ndc80 complex (2 nM) on taxol-stabilized Alexa-568-labeled microtubules (2.5 nM tubulin dimer). Panels show microtubules (a), Ndc80 complex (b), and merge (c). Panel dimensions are 66 by 66 μm. (*F*) Plot of binding density (v) versus free Ndc80 complex concentration (L). A fit to the Hill model (dashed line) was used to determine the apparent affinity (K_d), Hill coefficient (n_H), and lattice occupancy (i, the number of Ndc80 complexes bound per tubulin dimer). (*G*) Scatchard plot of the same data shown in *F*, fit to the McGhee and von Hippel model (dashed line) to calculate the K_d, cooperativity parameter (w), and i. For *F* and *G*, n = 8–10 replicates per data point, markers are mean ± SEM, and errors on model fit parameters (K_d, n_H, w, and i) represent SD.

measured using a bulk microtubule binding assay that measures the amount of GFP-tagged complex bound to microtubules over varying concentrations of complex (Fig. 1*E*) (32, 33). Based on a standard Hill model fit (34), the Ndc80 complex binds microtubules with a strong apparent affinity (K_d = 3.3 ± 0.2 nM) and has a Hill coefficient of 2.2 ± 0.2 (Fig. 1*F*). The Hill model describes cooperativity arising from allosteric changes that enhance ligand binding to a protein. In our binding assay, cooperativity is likely based on interactions between Ndc80 complexes that occur when they are bound to microtubules. Therefore, we used a model previously developed by McGhee and von Hippel that describes cooperativity between ligands binding to a polymer lattice (35). Fitting the binding data with this model (Fig. 1*G*) also showed a strong apparent affinity (K_d = 8.3 ± 1.5 nM) and cooperativity between Ndc80 complexes on the microtubule lattice (w = 3.4 ± 0.5). Compared with the Hill model fit, the McGhee and von Hippel model fit yielded a weaker apparent K_d for a single complex. Thus, interactions between complexes bound to the microtubule contribute to the K_d predicted by the Hill model. This finding is supported by the observation that at high concentrations, truncated Ndc80 complex binds microtubules in clusters (28). Fits to both models revealed a lattice occupancy of approximately two Ndc80 complexes per tubulin dimer, consistent with cryo-EM reconstructions that showed a 4-nm spacing of the truncated complex on microtubules (28).

Ndc80 Complex Directly Stabilizes Disassembling Microtubule Tips and Promotes Microtubule Rescue. In vivo, kinetochores transmit forces generated by the mitotic spindle to drive chromosome movement (36). This process depends on the ability of microtubule-binding components of the kinetochore to form stable attachments to dynamic microtubule tips. Using TIRF microscopy, we visualized the GFP-tagged Ndc80 complex on disassembling microtubules. In these assays, microtubule disassembly was induced by the removal of free tubulin. The human Ndc80 complex can track with disassembling microtubule tips (Fig. 2*A*), unlike the budding yeast Ndc80 complex, which requires the Dam1 complex or oligomerization on the surface of beads (23, 24). The human Ndc80 complex also slowed the rate of microtubule disassembly (Fig. 2*C*). As the concentration of the complex was increased from 0 to 500 pM, microtubule disassembly was slowed from 280 ± 20 nm/s to 100 ± 10 nm/s.

At 500 pM, bright particles of GFP-tagged Ndc80 complex were observed on microtubules (Fig. 2*B*), consistent with its cooperative binding behavior in our bulk assays. In some cases, disassembly appeared to stall as the tip reached these particles, and only continued after the Ndc80 complex appeared to detach. This behavior resulted in a step-like appearance in kymographs (Fig. 2*B*). Furthermore, Alexa-647–labeled tubulin decorated with Ndc80 complex was often seen bending away from the long axis of the microtubule (observed for 66 ± 10% of microtubules) (Fig. 2*D*, Fig. S3 *A* and *B*, and Movie S1). Because these curled extensions can be resolved by light microscopy (116-nm pixels), their curvature is gentler than the tight 20-nm curls seen at bare disassembling tips by cryo-EM in vitro (37). To further investigate tip structure in the presence of Ndc80 complex, we performed a similar disassembly assay and visualized the microtubule tips by negative-stain EM. We observed open protofilament sheets emanating from the tips of microtubules stabilized by Ndc80 complex (Fig. 2*E*). These sheets were not observed at the tips of microtubules stabilized by taxol or by the Dam1 complex (Fig. S3*C*) (38). Microtubules exposed to the same conditions in the absence of any stabilizing factor completely disassembled into free tubulin. Although we were unable to distinguish between microtubule plus- and minus-ends in the electron micrographs, curled extensions were observed in the presence of Ndc80 complex at both microtubule ends in the TIRF assay (Fig. S3*A*). Together, the TIRF and

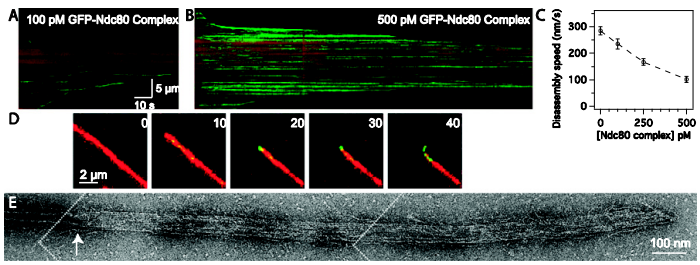

Fig. 2. The Ndc80 complex slows microtubule disassembly and stabilizes protofilament extensions. Kymographs of disassembling microtubules (red) in the presence of (*A*) 100 pM or (*B*) 500 pM GFP-tagged Ndc80 complex (green). Brightness and contrast were adjusted equally in *A* and *B*. (*C*) Mean disassembly speeds ± SEM for microtubules in the presence of increasing concentrations of Ndc80 complex (without Ndc80 complex, $n = 80$; 100 pM Ndc80 complex, $n = 31$; 250 pM, $n = 29$; 500 pM, $n = 34$). (*D*) Time-lapse images of a disassembling microtubule (red) in the presence of 500 pM GFP-tagged Ndc80 complex (green) as a curled extension formed at the tip. *Inset* numbers show elapsed time, in seconds. See Fig. S3*B* for a gallery of images showing curled extensions. (*E*) Negative-stain electron micrograph of a disassembling microtubule tip (see *SI Materials and Methods*) stabilized by the Ndc80 complex. An arrow marks the transition from a closed microtubule to an open sheet. The figure was constructed from three images, the boundaries of which are depicted by dotted white lines.

EM assays suggest that the Ndc80 complex slows disassembly by stabilizing protofilament extensions at microtubule tips.

To test how purified Ndc80 complex couples to dynamic microtubule tips under force, we used an optical trap-based bead motility assay (39). By incubating 11 pM beads with 5 nM Ndc80 complex (~450 complexes per bead), we estimate that up to ~20 complexes can interact with the microtubule tip based on geometric constraints (23). This number closely approximates the number of Ndc80 complexes per kinetochore microtubule in vivo (40). These beads remained coupled to microtubule tips against 2 pN of tension (Fig. 3 *A* and *B*), similar to the forces sustained by kinetochore-microtubule attachments in vivo, which are estimated to be 0.4–8 pN (23, 41, 42). Against the applied force, beads tracked robustly with the tips of disassembling microtubules over an average distance of 970 ± 190 nm ($n = 44$). Consistent with results from our TIRF-based assays, microtubule disassembly was slowed from 230 ± 14 nm/s (for microtubule tips not coupled to beads and in the absence of force) to 44 ± 7 nm/s by beads coated with Ndc80 complex under 2 pN of force (Fig. 3*C*). For episodes of disassembly-driven movement against the applied force, about half (53 ± 8%) ended in bead detachment, but a large proportion (40 ± 7%) underwent a microtubule rescue (the remaining events, 7 ± 3%, terminated for other reasons, such as the bead reaching the microtubule seed or nonspecifically adhering to the cover-slip). Strikingly, disassembling microtubule tips coupled to beads coated with the Ndc80 complex rescued ~70-fold more frequently than bare microtubules (Fig. 3*D*) (135 ± 24 h^{-1} compared with 2 ± 1 h^{-1}). Therefore, the Ndc80 complex is an effective tip-coupler that can directly slow microtubule disassembly and promote rescue.

In contrast, in our previous work with the budding yeast Ndc80 complex, we observed little effect on the rate of microtubule rescue (23). Here we analyzed the dataset reported in Powers et al. (23), specifically looking for rescue events. Microtubules rescued at a frequency of 9 ± 5 h^{-1} while coupled to beads coated with budding yeast Ndc80 complex ($n = 4$ rescues, ~100–2,700 complexes per bead, against ~1 pN of force). This number is close to the rate of rescue for microtubules not coupled to beads (reported above). Therefore, the budding yeast Ndc80 complex, unlike the human complex, appears to have little ability to promote microtubule rescue.

Phosphomimetic Mutations in the Ndc80 Complex Inhibit Its Ability to Influence Microtubule Dynamics. The Hec1 protein of the Ndc80 complex contains a calponin homology domain that is important for its microtubule binding activity (29, 30). In addition, Hec1 has a disordered N-terminal tail that contributes to the affinity of the complex for microtubules (11, 12, 30). In vivo, the tail is a target for the Aurora B kinase, and mutations that mimic phosphorylation at these sites result in unattached kinetochores (11, 43). Consistent with this observation, Aurora B phosphorylation of a truncated Ndc80 complex reduces its binding to microtubules in vitro (29). On the other hand, mutations that block phosphorylation severely damp kinetochore oscillations in vivo (8). These findings suggest that phosphorylation in the Hec1 tail is required not only for regulation of kinetochore-microtubule attachments, but also for normal kinetochore-microtubule dynamics. Using the optical trap assay, we tested the direct contribution of the tail to microtubule dynamics in vitro. In addition to the wild-type complex, we purified Ndc80 complex with the nine putative Aurora B target sites in the Hec1 tail mutated to aspartic acid to mimic phosphorylation (9D), and Ndc80 complex with the Hec1 tail deleted (ΔN). As a control, we also purified Ndc80 complex with alanine mutations at the Aurora B target sites (9A). Because this construct behaved like the wild-type complex in our TIRF assays (Figs. S3*B* and S4), it was not further characterized in the optical trap assay.

Beads coated with wild-type, 9D, and ΔN complexes were all able to slow the rate of microtubule disassembly in a concentration-dependent manner when tracking with disassembling tips against ~2 pN of applied force (Fig. 3 *B* and *C*). However, the 9D and ΔN complexes were impaired relative to the wild-type complex; when incubated with 5 nM of Ndc80 complex, 82 ± 11% of wild-type beads tracked with disassembling microtubule tips, but only 21 ± 5% of the 9D beads and 20 ± 4% of the ΔN beads tracked with disassembly (Fig. 3*B*). Furthermore, 5 nM wild-type beads slowed disassembly to 44 ± 7 nm/s, but 5 nM 9D and 5 nM ΔN beads slowed disassembly to 110 ± 20 and 96 ± 27 nm/s, respectively (Fig. 3*C*). The ability of the mutant complexes to track with and slow disassembly was recovered to wild-type levels by increasing the density of decoration on beads ~20-fold (Fig. 3 *B* and *C*: compare 0.5 and 1 nM wild-type to 10 and 20 nM mutant complexes, respectively). For example, beads coated with 20 nM 9D or 20 nM ΔN complex tracked with microtubules similarly to 1 nM wild-type beads (9D: 76 ± 11%; ΔN: 70 ± 10%; wild-type: 74 ± 9%). Therefore, increasing the number of mutant complexes on beads compensates for their decreased coupling performance.

When assayed at comparable coupling performance, the wild-type and ΔN complexes promoted microtubule rescue, but the 9D complex did not (Fig. 3 *D* and *E*). Deletion of the Hec1 tail reduced the ability of the complex to promote rescue only modestly (~twofold). In contrast, phosphomimetic mutations in the tail nearly abolished this activity. Using beads coated with 20 nM 9D complex, we observed only three rescue events in 29 min

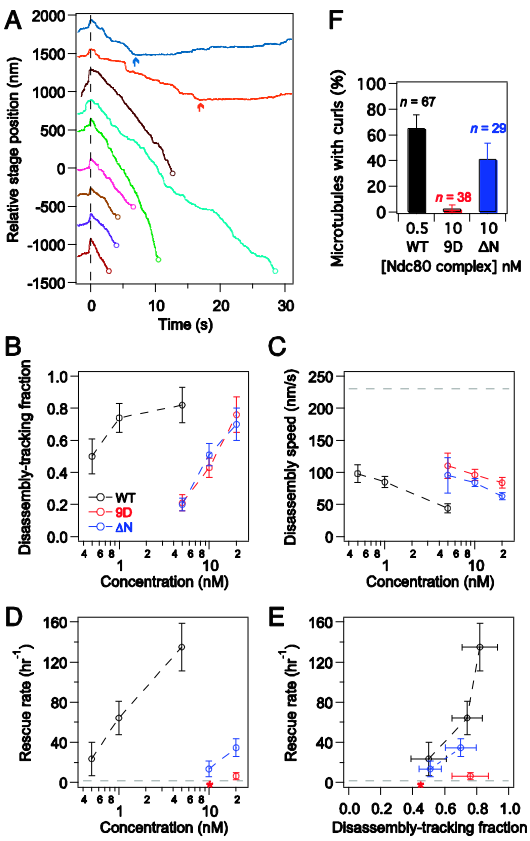

Fig. 3. Phosphomimetic mutations in the Ndc80 complex inhibit its ability to promote microtubule rescue. (*A*) Example traces of position vs. time for beads decorated with Ndc80 complex as they tracked microtubule disassembly against ~2 pN of applied force. Time t = 0 s (dashed vertical line) marks the onset of tracking, when the disassembling microtubule tip began to drive movement of the bead against the force of the trap. Disassembly-driven movement ended when the bead detached (open circles) or when the microtubule rescued (arrows). Traces are offset vertically for visual clarity. (*B*) The fraction of beads coated with wild-type or mutant Ndc80 complex capable of tracking against ~2 pN. From the disassembly-tracking events in *B*, (*C*) mean microtubule disassembly speeds ± SEM and (*D*) rescue rates were measured. Without load and in the absence of bead-bound Ndc80 complex, the disassembly rate was 230 ± 14 nm/s (dashed line in *C*, n = 26) and the rescue rate was 2 ± 1 h^{-1} (dashed line in *D*, n = 3 events in 104 min of disassembly). (*E*) Rescue rate is plotted against the fraction of beads that tracked disassembly against force. (*F*) Percentage of microtubules for which a curl (Fig. 2*D* and Fig. S3*B*) was observed at either tip during disassembly in the TIRF microscopy assay. The n for each data point in *B*–*D* is listed in Table S1. Asterisks indicate that no rescues were observed. Unless otherwise noted, all error bars represent uncertainties from counting statistics.

of microtubule disassembly, which is an average rescue frequency similar to that for bare microtubules (6 ± 4 vs. 2 ± 1 h^{-1}). In addition, the ΔN complex but not the 9D complex stabilized curled extensions at disassembling microtubule tips in the TIRF assay (Fig. 3*F*). Thus, phosphomimetic mutations do not simply negate the activity of the tail, but actively interfere with the ability to modify microtubule tip structure and promote rescue.

The ΔN and 9D complexes performed similarly in tracking with and slowing microtubule disassembly, suggesting that their disparate effects on microtubule rescue and tip structure are not simply the result of a difference in their microtubule-binding affinities. We quantified binding of GFP-tagged 9D and ΔN complexes directly by single-molecule TIRF microscopy and bulk microtubule binding assays. Unlike the wild-type complex, binding of the mutant complexes was undetectable in standard BRB80 (120 mM K^+) buffer conditions, so the assays were performed in BRB40 (60 mM K^+) buffer. Single molecules of 9D and ΔN complex exhibited similar dissociation and diffusion rate constants (Fig. 4 *A* and *B*) (k_{off} = 0.85 ± 0.07 and 0.90 ± 0.05 s^{-1}, and D = 0.060 ± 0.003 and 0.050 ± 0.002 $\mu m^2 \cdot s^{-1}$, respectively). In contrast, wild-type Ndc80 complexes dissociated from microtubules ~15-times more slowly (k_{off} = 0.062 ± 0.005 s^{-1}) and diffused on the lattice ~four-times more slowly (D = 0.015 ± 0.001 $\mu m^2 \cdot s^{-1}$). It has been previously suggested that the Hec1 tail contributes to microtubule binding by the Ndc80 complex or mediates cooperativity between complexes on microtubules (11, 12, 28). Our results establish that the tail contributes directly to microtubule binding, because deletion of the tail causes individual Ndc80 complexes (in the absence of cooperative binding) to dissociate more quickly from microtubules.

In the bulk binding assay, fits to both the Hill and the McGhee and von Hippel models (Fig. 4 *C* and *D*) show that the 9D and ΔN complexes are indistinguishable from one another in their apparent affinities, cooperativity constants, and lattice occupancies (McGhee and von Hippel fit for 9D and ΔN: K_d = 78 ± 20 and 73 ± 20 nM, w = 7 ± 2 and 7 ± 1, i = 2.4 ± 0.1 and 2.4 ± 0.1 per tubulin dimer, respectively). Therefore, phosphomimetic mutations reduce the affinity of the Ndc80 complex for microtubules and impair its ability to promote microtubule rescue. However, these two effects are not strictly coupled; deletion of the Hec1 tail equally reduces the affinity of the complex for microtubules, but is not as detrimental to its ability to modify microtubule tip structure and dynamics. These findings suggest that Aurora B phosphorylation has separable effects on attachment stability and microtubule dynamics at the kinetochore.

Discussion

Ndc80 Complex Directly Modulates Microtubule Dynamics. The Ndc80 complex is a conserved and essential microtubule-binding component of the kinetochore. Here, we characterized the binding of full-length human Ndc80 complex to microtubules in vitro. The Ndc80 complex bound cooperatively to microtubules with a strong affinity, and directly promoted microtubule rescue. Our in vitro results using unphosphorylated wild-type Ndc80 complex explain observations made in cells. In the absence of Hec1 phosphorylation, we found that the Ndc80 complex antagonizes microtubule disassembly. This effect explains why blocking Hec1 phosphorylation in vivo causes hyper-stabilized K-fibers, and leads to damped sister kinetochore oscillations and severe defects in cell division (8). We believe our findings are unique in representing a demonstration that a core component of the human kinetochore directly modifies microtubule rescue rate in vitro. This ability has been shown previously for a core kinetochore component only once, with the budding yeast Dam1 complex (44), which has no known homolog in higher eukaryotes. Notably, the budding yeast Ndc80 complex does not effectively promote microtubule rescue (23), even though the composition and domain structure of the complex are highly conserved.

Our results also indicate a possible mechanism by which the Ndc80 complex promotes microtubule rescue. In the absence of stabilizing factors, protofilaments at disassembling microtubule tips form tight ~20-nm curls (37). When microtubules are stabilized by a nonhydrolyzable GTP analog, protofilaments are straighter at disassembling tips (45). We found that the tips of disassembling microtubules in the presence of Ndc80 complex were gently

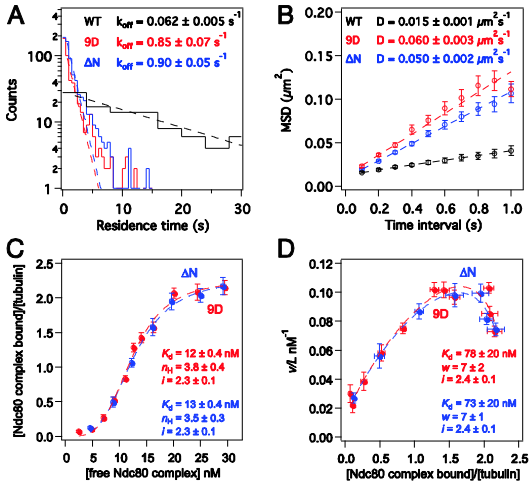

Fig. 4. The 9D and ΔN Ndc80 complexes exhibit similar binding behavior on microtubules. (*A*) Histograms of the residence time for single molecules (5 pM complex in solution) of wild-type (black trace, n = 131), 9D (red trace, n = 497), and ΔN (blue trace, n = 705) Ndc80 complex on taxol-stabilized microtubules. Each histogram was fit by a single exponential (dashed lines) to determine the off-rate constant, k_{off}. (*B*) Plots of MSD vs. time lag for binding events in *A*. The diffusion constant, D, was measured from linear fits to the data (dashed lines). (*C* and *D*) Bulk binding assays of 9D (red traces, n = 4–7 replicates per data point) and ΔN (blue traces, n = 6–7 replicates per data point) Ndc80 complex on taxol-stabilized microtubules. Dashed lines show fits of binding data to (*C*) Hill and (*D*) McGhee and von Hippel models. Errors on model fit parameters (K_d, n_H, w, and l) represent SD. All markers represent mean ± SEM and all assays were performed in BRB40 buffer (see *SI Materials and Methods*).

curved (as seen by TIRF microscopy) and formed large protofilament sheets (as seen by EM). These observations suggest that the Ndc80 complex promotes microtubule rescue by stabilizing tip structures with straighter protofilaments. Alushin et al. proposed that the Hec1 calponin homology domain recognizes the interface between tubulin monomers (28) at a putative hinge region (46). Our findings are consistent with this model. Ndc80 complex lacking the Hec1 tail was able to modify microtubule tip structure and promote rescue, indicating that other parts of the complex (outside of the tail) are primarily responsible for this activity. We propose that binding of the Hec1 calponin homology domain at the hinge region between tubulin subunits induces a straighter protofilament conformation that facilitates microtubule rescue.

Aurora B Regulates Microtubule Dynamics Through the Ndc80 Complex. The Aurora B kinase has an established role in releasing aberrant kinetochore-microtubule attachments (1). Consistent with this model, PtK cells carrying a phosphomimetic mutant Ndc80 (9D) complex have unattached kinetochores (11, 43). We found that the human 9D complex bound to microtubules more weakly relative to the wild-type complex, as determined by three independent in vitro assays. (*i*) Single molecules of the 9D complex dissociated more quickly (>10-fold) from the microtubule lattice. (*ii*) In our bulk assays, binding of the 9D complex was undetectable under conditions in which the wild-type complex bound strongly to microtubules. (*iii*) At equal surface density on beads, the 9D complex was impaired in its ability to track with microtubule disassembly against force. In all three of these assays, the 9D complex behaved similarly to and not worse than Ndc80 complex that lacks the tail domain (ΔN). Therefore, mutations that mimic complete phosphorylation of the Hec1 tail prevent the tail from contributing to microtubule binding.

In vivo observations suggest that in higher eukaryotes, Aurora B does not simply trigger kinetochore-microtubule detachment but additionally regulates microtubule dynamics (8, 10, 47). In PtK cells, syntelic kinetochore-microtubule attachments are not lost immediately following Aurora B activation (10). Instead, reactivation of Aurora B appears to induce disassembly of the kinetochore microtubules, and the kinetochores track with disassembly back to the centrosome, where the attachments are corrected. Our results offer insight into these observations. At higher surface densities on beads (20 nM), the 9D complex tracked robustly with disassembling microtubule tips against force. Based on geometric constraints (23), we estimate ~80 complexes can interact with the microtubule tip at this surface density. This number is more than the number of Ndc80 complexes per microtubule in vivo (~20 per microtubule), but fewer than the number of complexes at a single mammalian kinetochore, which binds 20–25 microtubules through more than 400 attachments (40, 48). Relative to the wild-type complex, the 9D and ΔN complexes are similarly impaired in their binding affinity and tracking performance. However, the ΔN complex promotes microtubule rescue, but the 9D complex does not. Thus, a phosphomimetic Hec1 tail interferes with the ability of the Ndc80 complex to modulate microtubule dynamics, possibly by blocking the ability of the calponin homology domain to stabilize a straighter protofilament conformation. Taken together, these in vitro observations explain how phosphorylation relieves microtubule stabilization at syntelic kinetochores to promote K-fiber disassembly, allowing the attached kinetochores to track back to the centrosome.

Here, we show that a conserved core microtubule-binding component of the human kinetochore directly influences microtubule dynamics. In addition, we find that phosphomimetic mutations of essential Aurora B phosphorylation sites in Hec1 not only weaken attachment, but also nearly abolish the ability of the Ndc80 complex to influence dynamics. These effects are separable, and might be independently tunable through phosphorylation of different subsets of target sites in the Hec1 tail. Taken together, our results indicate that microtubule dynamics can be regulated through Aurora B phosphorylation of the Ndc80 complex.

Materials and Methods

Protein Expression and Purification. The Ndc80 complex was coexpressed from two di-cistronic plasmids encoding Spc25/Spc24-His_6 and Hec1/Nuf2 (see *SI Materials and Methods*) in *E. coli* BL21 cells (Rosetta; Novagen). Protein expression and purification were carried out as previously described (23).

TIRF Microscopy. TIRF microscopy was performed on a custom illumination system (49) (see *SI Materials and Methods*). Taxol-stabilized Alexa-647-labeled microtubules were bound to the cover-slip with "rigor" kinesin (50). GFP-tagged Ndc80 complex was assayed in BRB80 (80 mM Pipes, 120 mM K^+, 1 mM $MgCl_2$, and 1 mM EGTA, pH 6.9) or BRB40 (40 mM Pipes, 60 mM K^+, 1 mM $MgCl_2$, and 1 mM EGTA, pH 6.9) with 8 mg·mL^{-1} BSA, 10 μM taxol, and an oxygen scavenger system. For dynamic microtubule assays, GMPCPP-stabilized microtubule seeds were bound to the cover-slip using "rigor" kinesin, and Alexa-647-labeled extensions were grown in BRB80 containing 8 mg·mL^{-1} BSA and 1 mM GTP. Microtubule disassembly was triggered by buffer exchange to remove free tubulin and simultaneously introduce GFP-tagged Ndc80 complex in BRB80 with 8 mg·mL^{-1} BSA, 1 mM GTP, and an oxygen scavenger system. See *SI Materials and Methods* for additional details.

Microtubule Binding Assays. Microtubule binding assays were performed as previously described (32), with the following modifications: GFP-tagged Ndc80 complex was incubated with taxol-stabilized microtubules in BRB80 with 10 μM taxol and 8% (vol/vol) gel filtration buffer (50 mM Hepes, 200 mM NaCl, pH 7.6), and pelleted through a glycerol cushion onto a cover-slip. The amount of microtubule-bound Ndc80 complex was quantified by fluorescence microscopy. Increasing concentrations of the complex (0–15 nM) were assayed with microtubules (2.5 nM tubulin dimers) to generate a binding curve. Microtubule binding for the 9D and ΔN Ndc80 complexes was undetectable in

BRB80, so binding assays were performed with 0–35 nM complex in BRB40. Binding curves were fitted to the Hill (34) and McGhee and von Hippel (35) models in Igor Pro (Wavemetrics) using iterative least-squares fitting. Errors on curve fit parameters (K_d, n_H, w, and i) represent the SD estimated by Igor Pro. See *SI Materials and Methods* for details of the assay.

Electron Microscopy. Ndc80 complex (50 nM) was incubated with taxol-stabilized microtubules (37 nM tubulin dimers) in BRB80 with 10 μM taxol. For disassembly assays, microtubules were assembled in the absence of taxol and disassembly was induced by dilution into BRB80 containing 25 nM Ndc80 complex. Samples were applied onto carbon-coated copper grids and stained with uranyl formate. Grids were viewed on a transmission electron microscope (Spirit T12; FEI). Additional details are provided in *SI Materials and Methods*.

Optical Trap Bead Motility Assays. Anti-His_5 antibody-coated polystyrene beads (11 pM) were functionalized by incubation with His_6-tagged wild-type (0.5–5 nM) or mutant (5–20 nM) Ndc80 complex. Beads were attached to the tips of disassembling microtubule extensions, which were grown from GMPCPP-stabilized microtubule seeds bound to the cover-slip. An optical trap was used to apply a constant force of ~2 pN opposite the direction of microtubule disassembly. Assays were performed in BRB80 containing 1.4 $mg{\cdot}mL^{-1}$ tubulin, 8 $mg{\cdot}mL^{-1}$ BSA, 1 mM DTT, 250 $\mu g{\cdot}mL^{-1}$ glucose oxidase, 30 $\mu g{\cdot}mL^{-1}$ catalase, and 4.5 $\mu g{\cdot}mL^{-1}$ glucose. Records of bead position over time were generated and analyzed using custom software (Labview and Igor Pro, respectively). These data were used to determine the fraction of beads that tracked with disassembly, and the rates of microtubule disassembly and rescue. Additional details are included in *SI Materials and Methods*.

ACKNOWLEDGMENTS. We thank A. Franck, A. Powers, B. Graczyk, and E. Mazanka for helpful discussions. We also thank the Murdock Charitable Trust and the Washington Research Foundation for support of our electron cryomicroscopy facility. This work was supported by National Institutes of Health Grant T32 GM008268 (to N.T.U.); a Natural Sciences and Engineering Research Council of Canada scholarship (to J.F.T.); Searle Scholar Award Grant 06-L-111 (to C.L.A.); Packard Fellowship for Science and Engineering Grant 2006-30521 (to C.L.A.); National Institute of General Medical Sciences Grants R01 GM40506 (to T.N.D.) and R01 GM079373 (to C.L.A.); Public Health Service National Research Science Award 2T32 GM007270 from the National Institute of General Medical Sciences (to B.S.V.); and the Howard Hughes Medical Institute (T.G.).

1. Liu D, Lampson MA (2009) Regulation of kinetochore-microtubule attachments by Aurora B kinase. *Biochem Soc Trans* 37:976–980.
2. Biggins S, Murray AW (2001) The budding yeast protein kinase Ipl1/Aurora allows the absence of tension to activate the spindle checkpoint. *Genes Dev* 15:3118–3129.
3. Cheeseman IM, et al. (2002) Phospho-regulation of kinetochore-microtubule attachments by the Aurora kinase Ipl1p. *Cell* 111:163–172.
4. Hauf S, et al. (2003) The small molecule Hesperadin reveals a role for Aurora B in correcting kinetochore-microtubule attachment and in maintaining the spindle assembly checkpoint. *J Cell Biol* 161:281–294.
5. Pinsky BA, Kung C, Shokat KM, Biggins S (2006) The Ipl1-Aurora protein kinase activates the spindle checkpoint by creating unattached kinetochores. *Nat Cell Biol* 8:78–83.
6. Tanaka TU, et al. (2002) Evidence that the Ipl1-Sli15 (Aurora kinase-INCENP) complex promotes chromosome bi-orientation by altering kinetochore-spindle pole connections. *Cell* 108:317–329.
7. Cimini D, Wan X, Hirel CB, Salmon ED (2006) Aurora kinase promotes turnover of kinetochore microtubules to reduce chromosome segregation errors. *Curr Biol* 16: 1711–1718.
8. DeLuca KF, Lens SM, DeLuca JG (2011) Temporal changes in Hec1 phosphorylation control kinetochore-microtubule attachment stability during mitosis. *J Cell Sci* 124: 622–634.
9. Cimini D, Moree B, Canman JC, Salmon ED (2003) Merotelic kinetochore orientation occurs frequently during early mitosis in mammalian tissue cells and error correction is achieved by two different mechanisms. *J Cell Sci* 116:4213–4225.
10. Lampson MA, Renduchitala K, Khodjakov A, Kapoor TM (2004) Correcting improper chromosome-spindle attachments during cell division. *Nat Cell Biol* 6:232–237.
11. Guimaraes GJ, Dong Y, McEwen BF, Deluca JG (2008) Kinetochore-microtubule attachment relies on the disordered N-terminal tail domain of Hec1. *Curr Biol* 18:1778–1784.
12. Miller SA, Johnson ML, Stukenberg PT (2008) Kinetochore attachments require an interaction between unstructured tails on microtubules and Ndc80(Hec1). *Curr Biol* 18:1785–1791.
13. Hunter AW, et al. (2003) The kinesin-related protein MCAK is a microtubule depolymerase that forms an ATP-hydrolyzing complex at microtubule ends. *Mol Cell* 11: 445–457.
14. Jiang K, et al. (2009) TIP150 interacts with and targets MCAK at the microtubule plus ends. *EMBO Rep* 10:857–865.
15. Knowlton AL, Lan W, Stukenberg PT (2006) Aurora B is enriched at merotelic attachment sites, where it regulates MCAK. *Curr Biol* 16:1705–1710.
16. Manna T, Honnappa S, Steinmetz MO, Wilson L (2008) Suppression of microtubule dynamic instability by the +TIP protein EB1 and its modulation by the CAP-Gly domain of p150glued. *Biochemistry* 47:779–786.
17. Tirnauer JS, Grego S, Salmon ED, Mitchison TJ (2002) EB1-microtubule interactions in *Xenopus* egg extracts: Role of EB1 in microtubule stabilization and mechanisms of targeting to microtubules. *Mol Biol Cell* 13:3614–3626.
18. Zhang X, Lan W, Ems-McClung SC, Stukenberg PT, Walczak CE (2007) Aurora B phosphorylates multiple sites on mitotic centromere-associated kinesin to spatially and temporally regulate its function. *Mol Biol Cell* 18:3264–3276.
19. Zimniak T, Stengl K, Mechtler K, Westermann S (2009) Phosphoregulation of the budding yeast EB1 homologue Bim1p by Aurora/Ipl1p. *J Cell Biol* 186:379–391.
20. Kline-Smith SL, Sandall S, Desai A (2005) Kinetochore-spindle microtubule interactions during mitosis. *Curr Opin Cell Biol* 17:35–46.
21. Wei RR, et al. (2006) Structure of a central component of the yeast kinetochore: The Spc24p/Spc25p globular domain. *Structure* 14:1003–1009.
22. Wei RR, Sorger PK, Harrison SC (2005) Molecular organization of the Ndc80 complex, an essential kinetochore component. *Proc Natl Acad Sci USA* 102:5363–5367.
23. Powers AF, et al. (2009) The Ndc80 kinetochore complex forms load-bearing attachments to dynamic microtubule tips via biased diffusion. *Cell* 136:865–875.
24. Tien JF, et al. (2010) Cooperation of the Dam1 and Ndc80 kinetochore complexes enhances microtubule coupling and is regulated by aurora B. *J Cell Biol* 189:713–723.
25. Lampert F, Hornung P, Westermann S (2010) The Dam1 complex confers microtubule plus end-tracking activity to the Ndc80 kinetochore complex. *J Cell Biol* 189:641–649.
26. Cheeseman IM, Chappie JS, Wilson-Kubalek EM, Desai A (2006) The conserved KMN network constitutes the core microtubule-binding site of the kinetochore. *Cell* 127: 983–997.
27. Tooley JG, Miller SA, Stukenberg PT (2011) The Ndc80 complex uses a tripartite attachment point to couple microtubule depolymerization to chromosome movement. *Mol Biol Cell* 22:1217–1226.
28. Alushin GM, et al. (2010) The Ndc80 kinetochore complex forms oligomeric arrays along microtubules. *Nature* 467:805–810.
29. Ciferri C, et al. (2008) Implications for kinetochore-microtubule attachment from the structure of an engineered Ndc80 complex. *Cell* 133:427–439.
30. Wei RR, Al-Bassam J, Harrison SC (2007) The Ndc80/HEC1 complex is a contact point for kinetochore-microtubule attachment. *Nat Struct Mol Biol* 14:54–59.
31. Wilson-Kubalek EM, Cheeseman IM, Yoshioka C, Desai A, Milligan RA (2008) Orientation and structure of the Ndc80 complex on the microtubule lattice. *J Cell Biol* 182: 1055–1061.
32. Graczyk B, Davis TN (2011) An assay to measure the affinity of proteins for microtubules by quantitative fluorescent microscopy. *Anal Biochem* 410:313–315.
33. Gestaut DR, et al. (2008) Phosphoregulation and depolymerization-driven movement of the Dam1 complex do not require ring formation. *Nat Cell Biol* 10:407–414.
34. Hill AV (1910) The possible effects of the aggregation of molecules of haemoglobin on its dissociation curves. *J Physiol* 40:iv–vii.
35. McGhee JD, von Hippel PH (1974) Theoretical aspects of DNA-protein interactions: Co-operative and non-co-operative binding of large ligands to a one-dimensional homogeneous lattice. *J Mol Biol* 86:469–489.
36. Koshland DE, Mitchison TJ, Kirschner MW (1988) Polewards chromosome movement driven by microtubule depolymerization in vitro. *Nature* 331:499–504.
37. Mandelkow EM, Mandelkow E, Milligan RA (1991) Microtubule dynamics and microtubule caps: A time-resolved cryo-electron microscopy study. *J Cell Biol* 114:977–991.
38. Westermann S, et al. (2005) Formation of a dynamic kinetochore- microtubule interface through assembly of the Dam1 ring complex. *Mol Cell* 17:277–290.
39. Franck AD, Powers AF, Gestaut DR, Davis TN, Asbury CL (2010) Direct physical study of kinetochore-microtubule interactions by reconstitution and interrogation with an optical force clamp. *Methods* 51:242–250.
40. Lawrimore J, Bloom KS, Salmon ED (2011) Point centromeres contain more than a single centromere-specific Cse4 (CENP-A) nucleosome. *J Cell Biol* 195:573–582.
41. Nicklas RB (1988) The forces that move chromosomes in mitosis. *Annu Rev Biophys Biophys Chem* 17:431–449.
42. Pearson CG, Maddox PS, Salmon ED, Bloom K (2001) Budding yeast chromosome structure and dynamics during mitosis. *J Cell Biol* 152:1255–1266.
43. Sundin LJ, Guimaraes GJ, Deluca JG (2011) The NDC80 complex proteins Nuf2 and Hec1 make distinct contributions to kinetochore-microtubule attachment in mitosis. *Mol Biol Cell* 22:759–768.
44. Franck AD, et al. (2007) Tension applied through the Dam1 complex promotes microtubule elongation providing a direct mechanism for length control in mitosis. *Nat Cell Biol* 9:832–837.
45. Müller-Reichert T, Chrétien D, Severin F, Hyman AA (1998) Structural changes at microtubule ends accompanying GTP hydrolysis: Information from a slowly hydrolyzable analogue of GTP, guanylyl (alpha,beta)methylenediphosphonate. *Proc Natl Acad Sci USA* 95:3661–3666.
46. Wang HW, Nogales E (2005) Nucleotide-dependent bending flexibility of tubulin regulates microtubule assembly. *Nature* 435:911–915.
47. DeLuca JG, et al. (2006) Kinetochore microtubule dynamics and attachment stability are regulated by Hec1. *Cell* 127:969–982.
48. Rieder CL (1982) The formation, structure, and composition of the mammalian kinetochore and kinetochore fiber. *Int Rev Cytol* 79:1–58.
49. Gestaut DR, Cooper J, Asbury CL, Davis TN, Wordeman L (2010) Reconstitution and functional analysis of kinetochore subcomplexes. *Methods Cell Biol* 95:641–656.
50. Rice S, et al. (1999) A structural change in the kinesin motor protein that drives motility. *Nature* 402:778–784.

Supporting Information

Umbreit et al. 10.1073/pnas.1209615109

SI Materials and Methods

Cloning. The human Ndc80 complex was coexpressed in *Escherichia coli* from two di-cistronic plasmids: one encoded Spc25 and His_6-tagged Spc24 in the pCDF backbone, and the other encoded Hec1 and Nuf2 in the pST39 backbone. To generate the Spc25/Spc24-His_6 plasmid, cDNA clones of Spc25 and Spc24 were purchased from ATCC and cloned into pST39 (1) using XbaI/ApaI and EcoRI/HindIII, respectively. A C-terminal His_6-tag was added to Spc24 for affinity purification and binding to polystyrene beads. The di-cistron of Spc25/Spc24-His_6 was transferred from the pST39 backbone into the pCDF backbone (Merck KGaA) using AscI (added by PCR amplification). To generate the Hec1/Nuf2 plasmid, cDNA clones of Hec1 (purchased from ATCC) and Nuf2 (kindly provided by Jennifer DeLuca, Colorado State University, Fort Collins, CO) were inserted into pST39 using EcoRV/KpnI and BspEI/MluI, respectively. For GFP-tagged Ndc80 complex expression, three fragments were generated and ligated together to clone GFP onto the C terminus of human Nuf2. First, the C terminus of Nuf2 was removed from the Hec1/Nuf2 pST39 plasmid using SphI and MluI. Second, a Nuf2 fragment was created by PCR to introduce a PacI site in place of the stop codon, and cut with SphI/PacI. Third, a GFP fragment was similarly created by PCR, to introduce sites for and cut with PacI and MluI. Simultaneous ligation of all three fragments generated pST39 containing a di-cistron of Hec1 and Nuf2-GFP. Ndc80 complex mutants were generated by site-directed mutagenesis using QuikChange Lightning kits (Stratagene) according to the manufacturer's protocol.

Total Internal Reflection Fluorescence Microscopy. Total internal reflection fluorescence (TIRF) microscopy was performed as previously described (2–5). A far-red laser (FTEC-635-0-25-PFQ; Blue Sky Research) and blue laser (Sapphire 488-75; Coherent) were used for simultaneous excitation of Alexa-647 and GFP. The illumination light reaching the sample was collimated and collected through the objective lens (CFI Planapochromat, 100×, 1.49 numerical aperture; Nikon). Emission channels from GFP and Alexa-647 were projected side-by-side onto a CCD camera (iXon 887-BI; Andor Technology), and images were collected at 10 frames per second with iXon software (Andor Technology).

Flow cells for TIRF microscopy were constructed and prepared as previously described (3). Flow cells were washed with H_2O and subsequently incubated for 5 min with "rigor" kinesin (6) diluted in BRB80 (80 mM Pipes, 120 mM K^+, 1 mM $MgCl_2$, and 1 mM EGTA, pH 6.9) with 8 mg·mL^{-1} BSA. Taxol-stabilized microtubules (1% Alexa-647–labeled tubulin) were bound for ~1 min and washed with BRB80 containing 8 mg·mL^{-1} BSA and 10 μM taxol. Flow cells were washed again with BRB80 or BRB40 (40 mM Pipes, 60 mM K^+, 1 mM $MgCl_2$, and 1 mM EGTA, pH 6.9) containing 8 mg·mL^{-1} BSA, 10 μM taxol, and an oxygen scavenger system (200 μg·mL^{-1} glucose oxidase, 35 μg·mL^{-1} catalase, 25 mM glucose and 5 mM DTT). GFP-tagged Ndc80 complex was introduced in BRB80 or BRB40 with 8 mg·mL^{-1} BSA, 10 μM taxol and an oxygen scavenger system. Single-molecule conditions were confirmed by measuring photobleach steps (at various excitation laser powers) for wild-type Ndc80 complexes on taxol-stabilized microtubules (Fig. S2). Laser powers were measured before entry into the microscope body.

In the dynamic microtubule TIRF experiments, GMPCPP-stabilized seeds (2% Alexa-647–labeled) were bound to the coverslip with "rigor" kinesin and washed with growth buffer (BRB80 with 8 mg·mL^{-1} BSA and 1 mM GTP). Dynamic extensions were polymerized off the seeds by the addition of growth buffer supplemented with 2 mg·mL^{-1} tubulin (1% Alexa-647–labeled) and an oxygen scavenger system. Disassembly was induced by buffer exchange with BRB80 containing 8 mg·mL^{-1} BSA, an oxygen scavenger system, and the reported concentration of GFP-labeled Ndc80 complex. All dynamic microtubule assays were done at 30 °C.

Software analysis was performed using Labview (National Instruments), as previously described (2–5). Kymographs were generated for both the Alexa-647 and GFP channels. The position and brightness over time was recorded for individual GFP-tagged complexes on microtubules. Custom programs (available upon request) written in Igor Pro (Wavemetrics) were used to generate residence time histograms and standard diffusion rate plots (mean-squared displacement vs. time lag). The dissociation rate constant (k_{off}) was calculated from a single exponential fit to the histogram of residence time. Diffusion rate constants were calculated from linear fits to diffusion plots. For dynamic microtubule assays, disassembly rates were measured as the average distance disassembled over time, as determined from Alexa-647 channel kymographs. Disassembly rates were measured only for the longer extension of each microtubule, and extensions shorter than 4 μm were discarded from analysis because of unreliability in measurements for short events. Microtubule tips were scored visually for the formation of extensions that curled away from the long axis of the microtubule during disassembly (Fig. S3 *A* and *B*). Only microtubules for which the tip was in focus throughout disassembly were scored.

Microtubule Binding Assays. The bulk binding assay was performed as previously described (3, 7). GFP-tagged Ndc80 complex was incubated with Alexa-568-labeled taxol-stabilized microtubules (2.5 nM tubulin dimers) for 10 min at room temperature. The incubation was done in BRB80 or BRB40 with 10 μM taxol and 8% gel filtration buffer (50 mM Hepes, 200 mM NaCl, pH 7.6). The reaction was fixed by addition of three volumes of 2% glutaraldehyde in BRB80 or BRB40 and incubated for 2 min at room temperature. The assay is not sensitive to the amount of glutaraldehyde used or the duration of the fix (7). A 750-μL glycerol cushion (15% wt/vol in PBS) was layered on top of a polylysine-treated glass cover-slip sitting on a custom spacer (Ellard Instrumentation) in a TLS-55 centrifuge tube (Beckman). A 250-μL portion of the fixed reaction mixture was layered onto the glycerol cushion and the microtubules were pelleted onto the cover-slip at 135,000 × *g* for 10 min at 25 °C. The supernatant and glycerol cushion were removed by aspiration and the cover-slip was placed onto a drop of Citifluor (Ted Pella), microtubule-side down, on a glass slide. The slide was sealed with nail polish to prevent evaporation.

Slides were imaged on a DeltaVision microscopy system (Applied Precision) containing an Olympus IX70 microscope, a 100× oil objective (1.35 numerical aperture), and a CoolSnap HQ digital camera (Roper Scientific). For each slide, 10 *z*-sections (0.3 μm) were taken in 10 consecutive panels (512 × 512 pixels, binned 2 × 2) using filter sets to detect GFP and Alexa-568. To determine the amount of GFP-tagged Ndc80 complex for each slide, the average pixel intensity for the second *z*-section image in the GFP channel was averaged for the 10 panels. These values were corrected for background (a slide in which microtubules were incubated in the absence of Ndc80 complex) and lamp intensity (using the photosensor value). Standard curves were made by incubating increasing concentrations (up to ~60 nM) of wild-type or mutant

Ndc80 complex with a saturating amount of microtubules (140 nM) in the appropriate buffers (BRB80 or BRB40), such that all Ndc80 complex added to the reaction was bound to microtubules. Microtubules were pelleted and imaged as described above. Slopes from the standard curves were used to convert fluorescence intensity values to concentrations for microtubule-bound Ndc80 complexes.

Electron Microscopy. Taxol-stabilized microtubules (37 nM tubulin dimers) were incubated with wild-type Ndc80 complex (50 nM) in BRB80 containing 10 μM taxol for ~10 min. Copper grids were carbon-coated and positively charged in a glow discharge device (EMS) at 25 mA for 2 min. A drop of the reaction mix (2 μL) was applied onto a freshly discharged grid and incubated for 20 s. Excess sample was blotted off, the grid was washed twice with BRB80, once with 0.075% uranyl formate, and stained with uranyl formate. Excess stain was blotted off and the grid was air-dried. Grids were viewed on a transmission electron microscope (Spirit T12, FEI) operating at 120 kV and images were recorded on a 1 k × 1 k bottom-mount slow-scan CCD camera (Gatan) at a nominal magnification of 21,000× at the specimen level.

For the disassembly assay, microtubules were assembled by incubating cleared tubulin (~6 μg/μL) in BRB80 containing 2 mM GTP, 5 mM $MgCl_2$, and 4% DMSO at 37 °C for 30 min. After assembly, 1 volume of warm BRB80 (37 °C) was added to make the stock microtubule mix. Disassembly was induced by diluting 1 μL of microtubule mix into 200 μL of a filtered BRB80 solution (0.22-μm filter; Millipore) containing 25 nM human Ndc80 complex, 25 nM budding yeast Dam1 complex (8), or 10 μM taxol, and incubating for 2 min at room temperature. Samples were then prepared for analysis and imaged by electron microscopy, as described above.

Optical Trap Bead Motility Assays. Ndc80 complexes were linked to the surface of polystyrene beads, as previously described (4, 5, 9). Streptavidin-coated beads (Spherotech) were functionalized with biotinylated anti-His_5 antibodies (Qiagen). His_6-tagged wild-type or mutant Ndc80 complex was incubated at the appropriate concentration (0.5, 1, 5, 10, or 20 nM) with 11 pM beads, rotating for 30 min at 4 °C. Beads were spun down at 16,100 × *g* in a desktop centrifuge for 5 min at 4 °C, and resuspended in 200 μL assay buffer (BRB80 containing 8 $mg{\cdot}mL^{-1}$ BSA and 1 mM DTT) to wash away unbound Ndc80 complex. The beads were spun again at 16,100 × *g* for 5 min at 4 °C, and resuspended with assay buffer to the original incubation volume.

Flow chambers were constructed and functionalized as previously described (9). First, one flow chamber volume of 1 $mg{\cdot}mL^{-1}$ biotinylated BSA (Vector Laboratories) was introduced and allowed to bind to the glass surface for ~10 min at room temperature. The chamber was then washed twice with ~20 volumes BRB80. Next, ~10 volumes 0.33 $mg{\cdot}mL^{-1}$ avidin DN (Vector Laboratories) was introduced, incubated for ~2 min, and washed out with ~20 volumes BRB80. GMPCPP-stabilized biotinylated microtubule seeds were introduced in BRB80, and allowed to bind to the functionalized glass surface for ~2 min. The chamber was then washed with ~20 volumes blocking buffer (BRB80 containing 1 mM GTP, 8 $mg{\cdot}mL^{-1}$ BSA, and 1 $mg{\cdot}mL^{-1}$ κ-casein), followed by a second wash with growth buffer (BRB80 containing 1 mM GTP and 8 $mg{\cdot}mL^{-1}$ BSA). Lastly, Ndc80 complex-coated beads were introduced at an eightfold dilution from the incubation mix (see above) in a solution of growth buffer containing 1.4 $mg{\cdot}mL^{-1}$ tubulin, 8 $mg{\cdot}mL^{-1}$ BSA, 1 mM DTT, 250 $\mu g{\cdot}mL^{-1}$ glucose oxidase, 30 $\mu g{\cdot}mL^{-1}$ catalase, and 4.5 $\mu g{\cdot}mL^{-1}$ glucose. The edges of the flow chamber were sealed with nail polish to prevent evaporation. Microtubule disassembly events occurred either by a spontaneous switch from assembly to disassembly or by laser scission, as described previously (9). All optical trap assays were performed at 26 °C.

Records of bead position vs. time were analyzed using custom software written in Igor Pro (available upon request). To be considered in the analysis, beads were required to have undergone tracking in the direction of disassembly against the applied force for at least 25 nm. Detachments were scored during the experiment and verified in analysis when the force on a bead under load suddenly dropped to zero, and the bead position trace exhibited "run-away" movement. Microtubule rescues were scored visually during the experiment and verified in analysis by identifying the time at which microtubule disassembly halted. Beads were observed for an additional ~30 s to verify that the bead subsequently underwent motion in the direction of microtubule growth at an assembly-limited rate (~10 nm/s) (Fig. 3*A*, top two traces). Intrinsic disassembly and rescue rates for bare microtubules in the absence of force were measured from traces of tip position versus time, as determined from differential interference contrast recordings (10). We also determined that microtubule rescue was not a result of the disassembling tip reaching the GMPCPP-stabilized microtubule seed; the microtubule lattice was laser-ablated approximately at the point where rescue occurred, and the microtubule was verified to undergo disassembly back to the stabilized seed. The rescue rate for microtubules was calculated by dividing the number of observed microtubule rescues by the total time of disassembly-driven motility recorded for each assay condition. Disassembly rates were estimated for each event by the slope of a linear fit to the bead position versus time trace, taken over the second half of the entire duration of the disassembly event. Events that lasted less than 2 s were not included in disassembly rate analysis because of unreliability in the linear fits over short time intervals.

1. Tan S (2001) A modular polycistronic expression system for overexpressing protein complexes in *Escherichia coli*. *Protein Expr Purif* 21:224–234.
2. Gestaut DR, Cooper J, Asbury CL, Davis TN, Wordeman L (2010) Reconstitution and functional analysis of kinetochore subcomplexes. *Methods Cell Biol* 95:641–656.
3. Gestaut DR, et al. (2008) Phosphoregulation and depolymerization-driven movement of the Dam1 complex do not require ring formation. *Nat Cell Biol* 10:407–414.
4. Powers AF, et al. (2009) The Ndc80 kinetochore complex forms load-bearing attachments to dynamic microtubule tips via biased diffusion. *Cell* 136:865–875.
5. Tien JF, et al. (2010) Cooperation of the Dam1 and Ndc80 kinetochore complexes enhances microtubule coupling and is regulated by aurora B. *J Cell Biol* 189:713–723.
6. Rice S, et al. (1999) A structural change in the kinesin motor protein that drives motility. *Nature* 402:778–784.
7. Graczyk B, Davis TN (2011) An assay to measure the affinity of proteins for microtubules by quantitative fluorescent microscopy. *Anal Biochem* 410:313–315.
8. Franck AD, et al. (2007) Tension applied through the Dam1 complex promotes microtubule elongation providing a direct mechanism for length control in mitosis. *Nat Cell Biol* 9:832–837.
9. Franck AD, Powers AF, Gestaut DR, Davis TN, Asbury CL (2010) Direct physical study of kinetochore-microtubule interactions by reconstitution and interrogation with an optical force clamp. *Methods* 51:242–250.
10. Walker RA, et al. (1988) Dynamic instability of individual microtubules analyzed by video light microscopy: Rate constants and transition frequencies. *J Cell Biol* 107: 1437–1448.

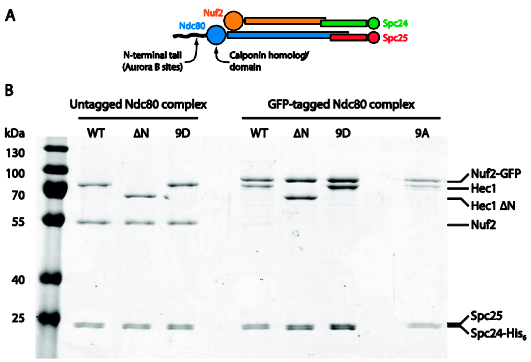

Fig. S1. The human Ndc80 complex was expressed in and purified from *E. coli* using affinity and size-exclusion chromatography. (*A*) Schematic of the heterotetrameric Ndc80 complex. (*B*) A Coomassie-stained gel shows the purified, recombinant wild-type and mutant versions of the Ndc80 complex used in this study. Molecular weight size markers are labeled on the left, and Ndc80 complex proteins, identified by size, are labeled on the right.

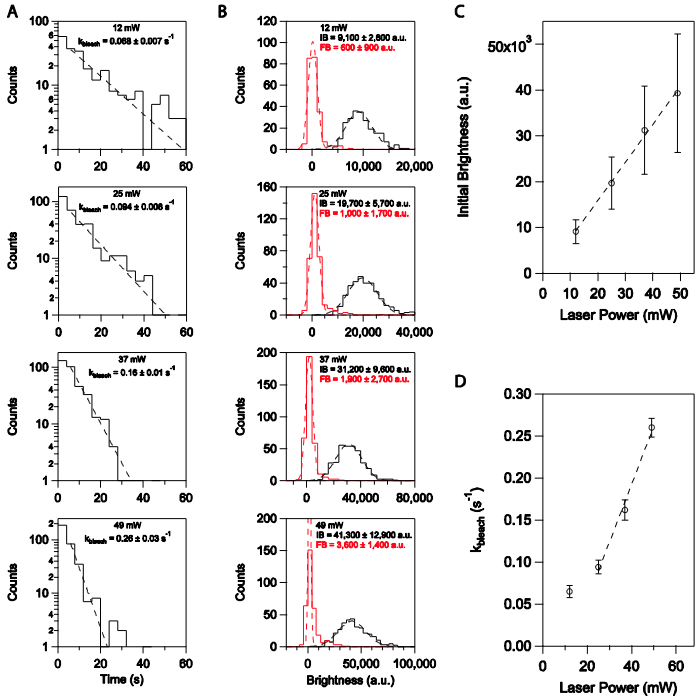

Fig. S2. The Ndc80 complex binds microtubules primarily as a monomer in the single-molecule TIRF assay. To determine if the GFP-tagged Ndc80 complex binds microtubules as a monomer in our single-molecule conditions (5–10 pM complex in solution), we imaged individual particles in BRB40 buffer under conditions that enhanced photobleaching. For example, a monomer would photobleach to near-background levels in a single step, whereas a dimer would photobleach in two steps of half the initial particle brightness. (*A*) Histograms of residence time with exponential fits (dashed lines) used to calculate the apparent bleach rate constant, k_{bleach} (a combination of GFP photobleaching rate and off-rate constants), at various excitation laser intensities. (*B*) Histograms and corresponding Gaussian fits of initial brightness (IB, black traces) and final brightness after photobleaching or detachment (FB, red traces). Note that the single bleach step (~95% of IB) for each condition is consistent with a monomeric species. (*C*) Plot of initial brightness vs. laser power with a linear fit (dashed line). (*D*) Plot of k_{bleach} vs. laser power. Above 12 mW, k_{bleach} increases linearly with laser power (dashed line), indicating that photobleaching (rather than detachment) contributes primarily to k_{bleach} under these conditions. For the datasets in *A–D*: n = 228 at 12 mW, n = 337 at 25 mW, n = 347 at 37 mW, and n = 327 at 49 mW.

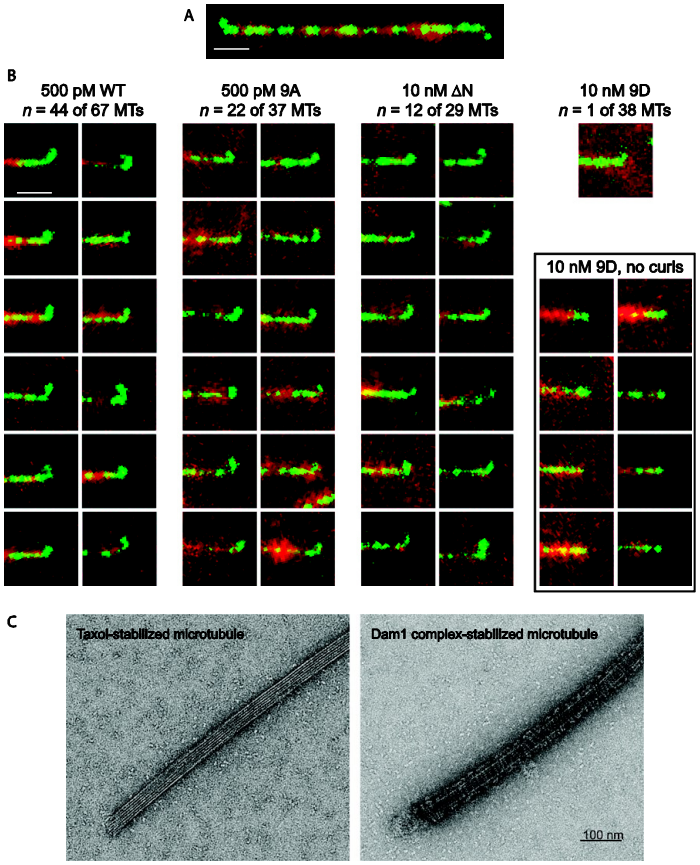

Fig. S3. Curls form at disassembling microtubule tips in the presence of Ndc80 complex. (*A*) In the presence of 500 pM GFP-tagged wild-type Ndc80 complex (green), curled extensions were observed at both ends of disassembling Alexa-647-labeled microtubules (red). (Scale bar, 2 μm.) (*B*) Gallery of curled extensions at the tips of disassembling microtubules in the presence of wild-type, 9A, ΔN, and 9D Ndc80 complex. The number (*n*) of microtubules (MTs) that formed curled extensions during disassembly is noted for each condition. (Scale bar, 2 μm.) (*C*) Negative-stain electron micrographs of disassembling microtubule tips (see *SI Materials and Methods*) stabilized by taxol or budding yeast Dam1 complex.

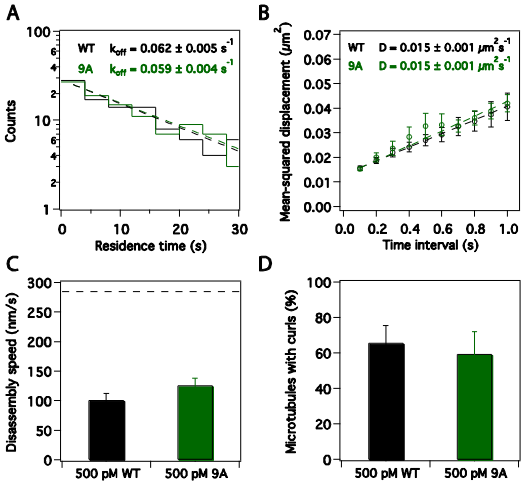

Fig. S4. Wild-type and 9A Ndc80 complexes exhibit similar binding behavior on microtubules. By TIRF microscopy, single molecules (5 pM complex in solution) of GFP-tagged wild-type (black traces, from Fig. 4 *A* and *B*) and 9A (green traces, $n = 124$) Ndc80 complexes have similar (*A*) residence time distributions and (*B*) diffusion rates on taxol-stabilized microtubules. A single exponential fit to the residence time distribution (*A*, dashed line) was used to calculate the off-rate constant, k_{off}. A linear fit to the mean-squared displacement versus time-lag plot (*B*, dashed line) was used to determine the diffusion constant, D. Markers represent the mean ± SEM (*C*) Microtubule disassembly speeds were measured in the presence of 500 pM wild-type (black bar, from Fig. 2*C*) or 500 pM 9A (green bar, $n = 35$) Ndc80 complex. Error bars represent SEM. Dashed horizontal line represents the intrinsic disassembly rate, 284 ± 15 nm/s, value reproduced from Fig. 2*C*. (*D*) Percentage of microtubules for which a curl was observed at the microtubule tip during disassembly in the presence of 500 pM wild-type (black bar, from Fig. 3*F*) or 500 pM 9A (green bar, $n = 37$) Ndc80 complex. Error bars represent counting uncertainties.

Table S1. Number of replicates for optical trap assays

Ndc80 complex	WT			9D			ΔN		
Concentration (nM)	0.5	1	5	5	10	20	5	10	20
n (Disassembly-tracking fraction)	40	84	74	98	134	58	122	111	74
n (Disassembly speed)	21	47	54	8	46	53	11	39	40
n (Number of rescues)	2	15	32	ND	0	3	ND	3	15
Rescue rate observation time (minutes of disassembly)	5	14	14	ND	16	29	ND	13	26

ND, not determined.

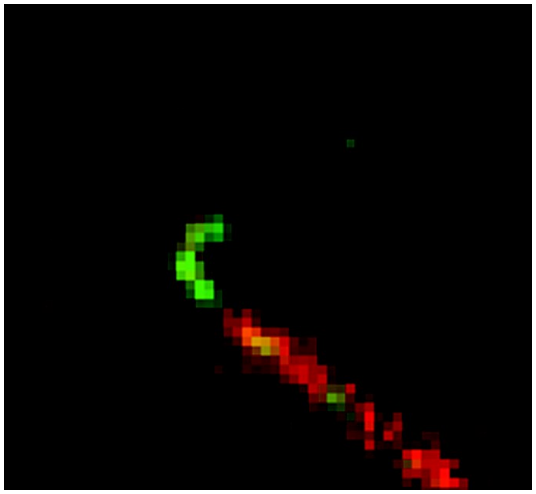

Movie S1. Ndc80 complex stabilizes curled extensions at disassembling microtubule tips. Movie shows 500 pM GFP-tagged Ndc80 complex (green) on a disassembling Alexa-647-labeled microtubule (red). GFP and Alexa-647 channels were visually aligned, and the brightness and contrast were adjusted for clarity using custom Labview software. Movie dimensions are 6.5 by 5.9 μm, and playback is at 9× speed.

Movie S1